

## Scattering-based Light Microscopy: From Metal Nanoparticles to Single Proteins

Lee Priest,<sup>†</sup> Jack S. Peters,<sup>†</sup> and Philipp Kukura\*



Cite This: *Chem. Rev.* 2021, 121, 11937–11970



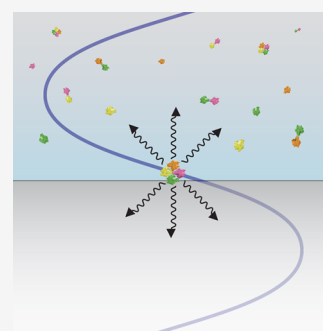
Read Online

ACCESS |

Metrics & More

Article Recommendations

**ABSTRACT:** Our ability to detect, image, and quantify nanoscopic objects and molecules with visible light has undergone dramatic improvements over the past few decades. While fluorescence has historically been the go-to contrast mechanism for ultrasensitive light microscopy due to its superior background suppression and specificity, recent developments based on light scattering have reached single-molecule sensitivity. They also have the advantages of universal applicability and the ability to obtain information about the species of interest beyond its presence and location. Many of the recent advances are driven by novel approaches to illumination, detection, and background suppression, all aimed at isolating and maximizing the signal of interest. Here, we review these developments grouped according to the basic principles used, namely darkfield imaging, interferometric detection, and surface plasmon resonance microscopy.



### CONTENTS

1. Introduction	11937
2. Key Principles	11938
3. Darkfield Imaging	11939
3.1. Introduction	11939
3.2. Total Internal Reflection Scattering	11940
3.3. Rotating Coherent Scattering Microscopy	11942
3.4. Objective Coupling Mirror	11943
3.5. Darkfield Stop	11944
3.6. Darkfield Imaging Using Optical Waveguides	11944
4. Interferometric Imaging	11945
4.1. Introduction	11945
4.2. Interferometric Scattering Microscopy I: Single Particle Tracking	11946
4.3. Interferometric Scattering Microscopy II: Label-free Imaging	11949
4.4. Mass Photometry	11949
4.5. Interferometric Reflectance Imaging Sensor	11951
4.6. Coherent Brightfield Imaging	11953
5. Plasmonic Imaging	11954
5.1. Introduction	11954
5.2. Surface Plasmon Resonance Microscopy	11955
5.3. Biomolecular Imaging and Detection	11956
5.4. Resolution-enhanced Surface Plasmon Resonance Microscopy	11958
6. Summary and Outlook	11959
Author Information	11961
Corresponding Author	11961
Authors	11961
Author Contributions	11961
Notes	11961

Biographies	11961
Acknowledgments	11961
Abbreviations	11961
References	11962

### 1. INTRODUCTION

Structure and dynamics at the nanoscale determine the properties of matter and underpin the mechanisms of life. To understand and ultimately control these properties and functions, we must be able to visualize and thereby study matter on nanoscopic length scales. Much effort has thus been directed at the development and optimization of methods capable of detecting and characterizing nanoscopic objects. Broadly speaking, these can be divided into scanning probe approaches<sup>1–4</sup> and those using the interaction between incident radiation and matter, including both electron microscopy and light microscopy. Light microscopy has been popular due to its noninvasive nature, dynamic operation, potential for high-throughput, and straightforward integration with other technologies. However, these capabilities come at the expense of inferior sensitivity and resolution, as compared to electron microscopy or scanning probe methods.

**Special Issue:** Frontiers of Analytical Science

**Received:** March 31, 2021

**Published:** September 29, 2021



In the context of sensitivity, light microscopy arguably reached its ultimate limit more than 30 years ago with the detection of individual ions and molecules using absorption and fluorescence as contrast mechanisms.<sup>5–7</sup> These single-molecule experiments were performed under cryogenic conditions with specifically selected chromophores to maximize the interaction strength between the incident light and the molecules of interest. Single-molecule experiments in the form of single-emitter fluorescence detection and imaging have since become routine.<sup>8</sup> These experiments benefit from the specific advantage of fluorescence: the spectral separation between illumination and emission profiles, which enables efficient background suppression. This makes it possible to identify specific species in complex mixtures and optically noisy environments, such as living cells, as long as the surrounding objects are non- (or weakly) fluorescent at the combination of illumination and detection wavelengths. The ability to switch fluorophore emission on and off, both temporally and spatially, has also led to the emergence of super-resolution imaging techniques, in which the spatial resolution is now approaching the molecular scale.<sup>9–14</sup>

At the same time, using fluorescence as a contrast mechanism limits applicability of the most sensitive studies to species that are either highly fluorescent themselves or are made fluorescent by the introduction of external tags. Moreover, photochemical and photophysical processes limit both signal intensities and the degree to which signals are quantitative, which is often critical in the analytical context. These limitations, in combination with the prospect of a broader application scope, has driven the development of fluorescence-free methodologies. An alternative approach to separate illumination from detection is to exploit a geometric separation between them, as demonstrated by Siedentopf and Zsigmondy in 1902, who presented the ultramicroscope.<sup>15</sup> The orthogonal illumination and detection pathways enabled the observation of light scattered by nanometer-sized gold colloids. Since this work, many different optical strategies have been developed to image scattered light in the absence of background, and they are grouped together under the term darkfield microscopy. Originating from Zernike's phase contrast microscopy (PCM) in 1935, many technologies have used interference between transmitted (or reflected) incident and scattered light as the primary image contrast mechanism.<sup>16–18</sup> These include differential interference contrast (DIC),<sup>19,20</sup> interference reflection microscopy (IRM),<sup>21,22</sup> and reflection interference contrast microscopy (RICM),<sup>23,24</sup> all of which have predominantly focused on studies of tissues, cells, and supramolecular assemblies due to their lack of sensitivity for nano-objects sub-20 nm in diameter.

In fluorescence-free, extinction-based techniques, the contrast is generated from a combination of the scattering and absorption of incident light. Until recently, scattering-based techniques exhibited inferior sensitivity when compared to their absorption-based counterparts, which reached single-molecule sensitivity at room temperature a decade ago.<sup>25–27</sup> Irrespective, the development of scattering-based techniques has continued toward the robust detection of single biological macromolecules, even in the absence of absorption. The main advantage of these techniques is their universal applicability, as any sample with a different refractive index to its surrounding medium will generate a signal. The key challenge in the context of studying nanoscale phenomena is thus to develop experimental configurations which are capable of detecting and isolating the smallest possible signals. This challenge is being addressed by a variety of efforts

to reduce the imaging background or amplify the signal of interest.

In this review, we provide an overview of recent developments in approaches detecting light scattering with optical microscopes because of the underlying common architecture, although we would like to emphasize the remarkable levels of sensitivity achieved with alternative approaches, such as microcavities.<sup>28–30</sup> After a brief introduction to the key concepts (section 2), we begin by reviewing advances in darkfield microscopy (section 3), focusing on approaches aimed at maximizing detection sensitivity by selecting photons that have interacted with the object of interest. A natural extension involves the use of illumination light to enhance the small signal that results from the weak interaction with the nano-object by interference (section 4). We conclude with an overview of efforts aimed at introducing additional signal amplification with plasmonically active substrates (section 5) before providing a brief summary and outlook (section 6).

## 2. KEY PRINCIPLES

The fundamental challenge in imaging on the nanoscale arises from the drop in interaction strength between the incident electromagnetic radiation and the object as the object becomes much smaller than the illumination wavelength,  $\lambda$ . This challenge can generally be compartmentalized into three key parameters: resolution, specificity, and sensitivity.

Spatial resolution, the minimum distance at which two distinct points in a specimen can be distinguished, can be divided into the lateral (X/Y) and axial (Z) dimensions. Resolution is limited by the diffraction of light as it passes through a circular aperture, such as an objective lens, ultimately restricting the achievable confinement of light and defining the imaged projection of a point-source, the point-spread function (PSF). This diffraction barrier was first introduced by Abbe,<sup>31</sup> with the lateral resolution limited to  $\lambda/2NA$ , where NA is the numerical aperture of the objective lens, defined by the refractive index of the imaging medium multiplied by the sine of the maximum angle over which light can be gathered from the sample. Axial resolution is limited even further ( $2\lambda/NA^2$ ) due to the elliptical geometry of the PSF along this axis, creating an additional challenge for resolving objects in three dimensions.

In the context of microscopy, specificity refers to the ability to distinguish signals from different types of objects of interest within a sample. This can be achieved by a variety of strategies, including: analysis of the magnitude of a detected signal, surface functionalization to promote specific binding and attachment of multiple different fluorescence or scattering labels. For the techniques discussed in this review, specificity relies on these strategies as chemical specificity is not inherently encoded within Rayleigh scattering (in contrast to Raman scattering).<sup>33,34</sup>

Finally, sensitivity refers to the ability of an instrument to not only detect a signal from an object but to differentiate it from any unwanted background signal, or noise. For an ideal experiment, with no external or environmental noise, the noise-floor is limited by the properties of the detector, such as dark noise and read noise, as well as the quantum noise (referred to as shot noise) associated with the counting of discrete particles (photons) arriving at the detector. The width of this Poissonian intensity distribution thus scales with  $\sqrt{N}$ , where  $N$  is the number of photons detected. Because of the well-defined geometry of the PSF described above, it is possible to localize its center of mass with subdiffraction limited precision by fitting the

PSF to a 2D Gaussian function,<sup>35</sup> which enables high-resolution tracking of the motion of an object of interest. Localization precision is limited by the number of photons detected and can be approximated as  $\sigma/\sqrt{N}$  in a shot-noise-limited experiment, where  $\sigma$  is the standard deviation of the PSF fit.<sup>36</sup> This leads to an interplay between the localization precision and temporal resolution of a tracking experiment due to the limited number of photons that can be detected per unit time. In fluorescence-based approaches, the number of photons detected per unit time is limited by optical saturation of the fluorophore. In scattering-based approaches, there is no a priori limited photon budget provided by the scattering object, so the limitation is determined by either sample/optical damage thresholds or saturation of the detector.

Intuitively, the strength of the interaction between light and an object should scale with the polarizability of the object, which is a measure of its ability to respond to and interact with an incident electromagnetic wave. Assuming that the object of interest can be approximated as a sphere, which is often a good approximation for nanoscopic objects much smaller than the diffraction limit, it can be treated as a point dipole with a polarizability given by

$$\alpha = 3\epsilon_m V \left( \frac{\epsilon_p - \epsilon_m}{\epsilon_p + 2\epsilon_m} \right) \quad (1)$$

where  $\epsilon_{m/p}$  is the complex permittivity of the medium and particle respectively, and  $V$  is its volume.<sup>37</sup> The polarizability then yields the scattering and absorption cross sections as

$$\sigma_{\text{scat}} = \frac{8}{3\pi^2} |\alpha|^2 \lambda^{-4} \quad (2)$$

$$\sigma_{\text{abs}} = \frac{2\pi}{\lambda} \text{Im}(\alpha) \quad (3)$$

which sum to yield the extinction cross-section,  $\sigma_{\text{ext}}$ . For nonresonant particles,  $\sigma_{\text{scat}}$  dominates the detected signal. The dependence of  $\sigma_{\text{scat}}$  on the square of the volume of the particle is primarily responsible for the difficulty of detecting very small objects without the use of a label: a reduction in the diameter of a sphere by a factor of 10 reduces the intensity of scattered light by  $10^6$  for a given incident photon flux. While this can be somewhat alleviated by plasmonic scattering enhancement for materials such as silver and gold, the volume of the nanoparticle still dominates the magnitude of its scattering signal.

Generally speaking, when shining light on a sample, the detected signal intensity at a given point in the image ( $I_{\text{det}}$ ) can be written as the sum of the fields associated with the relatively unperturbed incident light ( $E_i$ ) and the light scattered by the presence of an object ( $E_s$ ):

$$I_{\text{det}} = |E_i + E_s|^2 = |E_i|^2 + |E_s|^2 + 2\text{Re}(E_i E_s^*) \quad (4)$$

The scattered light field is proportional to the complex polarizability of the object, implying both linear and quadratic dependencies of the two signal contributions on the volume of the object, a feature that can be taken advantage of. In the context of extinction measurements, the cross-term in eq 4 indicates that spatial mode matching between the wavefronts of the two fields is desirable for efficient extinction to occur. A tightly focused Gaussian beam has a stronger dipolar character compared to plane wave illumination and hence improves the interaction with a dipolar nanoscopic scatterer resulting in increased extinction efficiency.<sup>38</sup> This effect on the extinction

signal is somewhat unsurprising if considered from the perspective of maximizing the ratio of the extinction cross-section to the area of the illumination profile ( $\sigma/A$ ).

It is also important to note that, for a point source located near a refractive index interface, a high proportion of the incident light is scattered into the higher index material, resulting in this light being collected at large angles by the objective lens.<sup>39–41</sup> Consequently, illuminating the sample via the low NA regions of the objective, such as in wide-field illumination, provides an opportunity to spatially discriminate between the scattered and transmitted/reflected illumination light in the back focal plane (BFP) of the objective. This can be advantageous when attempting to manipulate eq 4, and therefore the contrast of the final image, by perturbing one field relative to the other.<sup>42–45</sup>

Thus far, we have only considered the signal arising from the object of interest, but the presence of background light poses the most significant limitation to object sensitivity. Unwanted background light can emanate from multiple sources, such as other scattering objects in the sample, surface inhomogeneity of the sample substrate (typically a glass coverslip), or stray reflections from components in the optical system. For conventional brightfield illumination, the largest background contribution arises from the illumination field, which renders the small signal from a nano-object signal very difficult to detect.

All approaches discussed in this review attempt to manipulate the relative magnitudes of the different contributions in eq 4, with the ultimate goal of detecting and in some cases obtaining additional information about the object through  $E_s$ . Darkfield imaging (section 3) refers to methods that minimize any light that has not interacted with the object of interest,  $E_i$ , in detection. The focus is thus on detecting and quantifying  $|E_s|^2$ , which becomes increasingly challenging the smaller the object becomes due to the  $V^2$  scaling in the presence of competing background signals. Alternatively, one can attempt to reduce the relative magnitude of background signals by focusing on the interference term  $2\text{Re}(E_i E_s^*)$ , which is the target of interferometric microscopy (section 4). As both of these methods will eventually face the limitation of finite illumination powers and polarizabilities, additional steps can be taken to increase  $E_i$  beyond what can be achieved in a straightforward illumination approach, for instance by taking advantage of plasmonic effects (section 5).

### 3. DARKFIELD IMAGING

#### 3.1. Introduction

The most intuitive way to maximize the sensitivity of a microscope is to isolate the photons that interacted with the species of interest from any background signal, a concept optimized in single molecule fluorescence imaging, where this isolation is achieved by filtering for photons of specific wavelengths during both illumination and detection. In the context of scattering detection, analogous efforts to maximize background rejection can be broadly grouped under the term darkfield microscopy.<sup>46–50</sup> The major difference, in this sense, between fluorescence imaging and darkfield microscopy is that the illumination light is of the same wavelength as the scattered light, meaning that background rejection cannot be achieved by orthogonal optical filters. In terms of eq 4, we eliminate  $E_i$ , as far as possible, meaning that in an ideal scenario:

$$I_{\text{det}} \sim |E_s|^2 \quad (5)$$



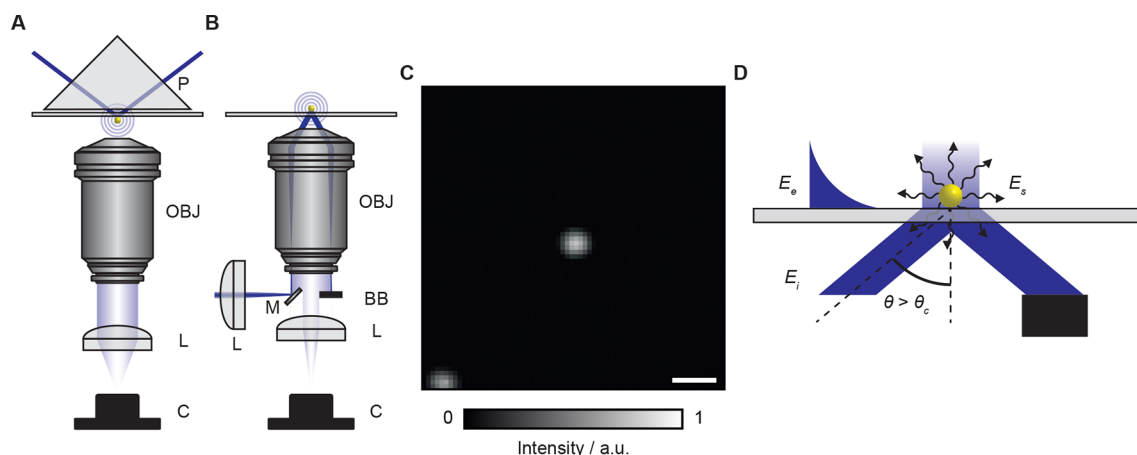


**Figure 1.** Commonly employed approaches to scattering-based total internal reflection microscopy. (A) Prism-type total internal reflection microscopy. (B) Objective-type total internal reflection microscopy. P, prism; OBJ, objective; L, tube lens; M, mirror; BB, beam block; C, camera. (C) Image of a 20 nm GNP on a glass coverslip taken with an optimized objective-type TIRS microscope, scale bar = 0.5 μm. (D) Schematic illustrating the fields involved with TIRS microscopy,  $E_i$  incident field,  $E_s$  scattered field,  $E_e$  evanescent field,  $\theta$  incident angle of illumination, which is greater than the critical angle,  $\theta_c$ . (C) adapted with permission from ref 58. Copyright 2021 Philipp Kukura.

In practice, most approaches are variations on the original theme introduced by Siedentopf and Zsigmondy more than a century ago.<sup>15</sup> While field separation in this case was achieved by detecting scattered light orthogonally to the direction of illumination, this has since been achieved through the use of appropriately placed beam stops, apertures, or reflective optics. In the context of this review, the key limitation and challenge faced by darkfield approaches, in the spirit of detecting ever smaller objects, can be traced to the  $V^2$  scaling of the purely scattered term and the presence of imaging background. As a result, darkfield microscopes perform well when detecting and imaging objects with a diameter on the order of >20 nm but struggle immensely to reach the 5 nm scale required for single macromolecules or small nanoparticles. While light scattered by such small objects could still in principle be detected, this rapid drop in scattered power has in practice been overwhelmed by stray light from the sample or any components in the imaging setup. Even if the background signal intensity were fixed over the course of a measurement, such that it could be isolated from the analyte signal and thus subtracted from the final image, an extremely high dynamic range measurement would be required to detect the signal from a single molecule. Most recent efforts aimed at improving the performance of darkfield microscopes have thus focused on innovative approaches to separate the scattered light from the background light, and in this section we review those approaches.

### 3.2. Total Internal Reflection Scattering

Total internal reflection (TIR) refers to the reflection of incident light at a refractive index boundary and provides a convenient means of containing the illumination light at the glass–water interface. This is usually achieved by directing a laser beam onto the sample substrate at an angle above the critical angle, which generates an evanescent field within a few hundred nanometers of the surface of the substrate. This type of illumination has been heavily utilized in total internal reflection fluorescence (TIRF) microscopy.<sup>51–53</sup> TIR illumination can be advantageous in darkfield microscopy as the signal ideally only contains contributions from scatterers close to the surface of the substrate, thereby minimizing stray light. The first use of TIR illumination in a darkfield microscope was presented by Ambrose in 1956, where cells in water were imaged on the

surface of a glass slide, which was illuminated above the critical angle via a glass prism (Figure 1A).<sup>54,55</sup> In this section, we will focus on objective-type total internal reflection scattering (TIRS) microscopy, which was introduced as an alternative to prism-based illumination by Braslavsky et al.<sup>56</sup> In objective-type TIR illumination, the critical angle is reached by using the outer edges of the entrance pupil of a suitably high-NA oil immersion objective, as previously demonstrated by Stout and Axelrod in TIRF microscopy.<sup>57</sup> In the original objective-type TIRS study,<sup>56</sup> two different optical set-ups were suggested, both based on an inverted microscope and using a beamsplitter to direct the illumination into the objective lens and a field stop to block the back-reflected beam at a position where the BFP of the objective lens is reimaged. The authors demonstrated the sensitivity of the technique by imaging 20 nm gold nanoparticles (GNPs) and 60 nm polystyrene beads.

While we refer throughout this section to reported performance characteristics, such as localization precision and temporal resolution, these parameters are not necessarily comparable across techniques. The reason is that the ultimate performance depends on the details of the experimental arrangement beyond the optical approach: detection efficiency, mechanical stability, illumination power, and alignment details in terms of background suppression. Nevertheless, the reported literature values provide an indication of what is possible and has been demonstrated, which should be considered in combination with the approach as a whole.

For objective-type TIR, the key challenge involves coupling the illumination light in and out of the imaging objective, while minimizing the amount of stray light reaching the detector. Generally, this is best achieved by placing the reflective elements as close as geometrically possible to the entrance pupil of the objective, which minimizes back reflections from the multiple lenses within the objective (Figure 1B). While reimaging is a possibility, as in the original study by Braslavsky et al.,<sup>56</sup> focusing a laser beam into the BFP of a high-NA objective lens produces a number of divergent reflections, which can be difficult to eliminate in a reimaging configuration. In objective-based darkfield techniques, there is an interplay between background suppression and the effective NA of the optical system, as blocking stray light reduces scattered light collection.



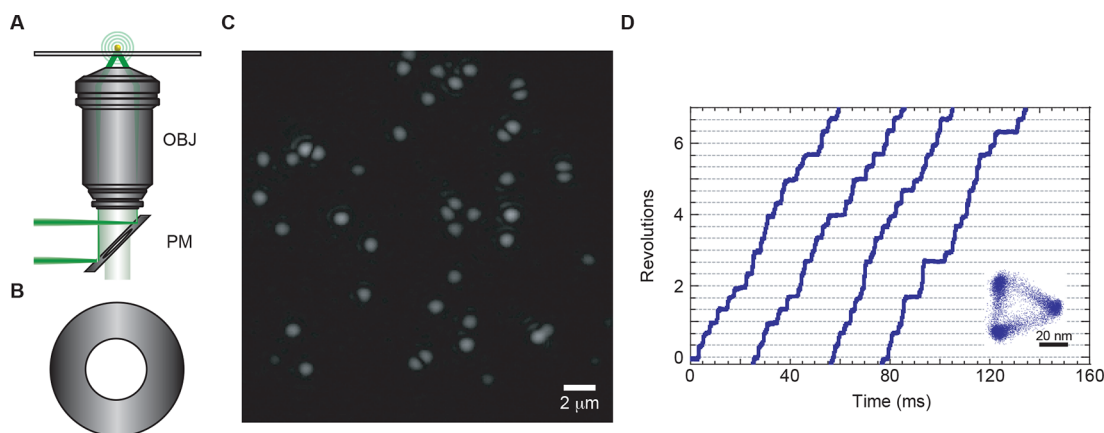


**Figure 2.** Perforated mirror TIR darkfield microscopy. (A) Schematic demonstrating the separation of scattered light from the reflected illumination beam. OBJ, objective lens; PM, perforated mirror. (B) View from the back aperture of the objective looking down the optical axis. (C) Image of 40 nm GNP in water immobilized on a glass slide. (D) Rotational motion of 40 nm gold-nanoparticle-labeled F<sub>1</sub>-ATPase at 2 mM ATP, with the inset displaying an example trace from which the data is obtained. (C,D) Adapted with permission from ref 59. Copyright 2010 Elsevier.

Noji and co-workers approached this problem by introducing a perforated mirror.<sup>59</sup> The concept behind perforated mirror TIR darkfield is to sacrifice spatial resolution and collection efficiency in exchange for background suppression. The optical setup is based on a standard TIRF microscope, with the dichroic mirror exchanged for a perforated mirror, a mirror with an elliptical hole in the center that allows a portion of the scattered light to pass while blocking the reflected illumination beam (Figure 2A). When viewed along the optical axis, the elliptical hole in the perforated mirror acts as a circular aperture, which prevents the introduction of aberrations from asymmetrically cutting the NA (Figure 2B). In proof-of-principle experiments, 40 nm GNPs were imaged with 0.1 ms temporal resolution on a glass surface (Figure 2C). The resulting SNR was 1.5–2.1 times higher for perforated mirror TIR darkfield as compared to an epi-illumination darkfield microscope with a dot mirror. This improvement resulted from the increase in background suppression and occurred despite a considerable drop in the NA of the optical system caused by the interception of scattered light by the perforated mirror.

In fluorescence-free microscopy, GNPs are regularly used as scattering labels due to the relatively large scattering cross-section for the particle size as a result of plasmonic enhancement. This concept was combined with perforated mirror TIR darkfield to study multiple molecular motors with high spatiotemporal resolution. Labeling the  $\gamma$ -subunit of the F<sub>1</sub>-ATPase motor with a 40 nm GNP enabled the rotational motion of the motor to be tracked with 9.1  $\mu$ s time resolution and a localization precision on the order of 1–2 nm (Figure 2D). Building on this work, the rotational dynamics of the F<sub>1</sub>-ATPase,<sup>60–64</sup> V<sub>1</sub>-ATPase,<sup>65,66</sup> and V<sub>0</sub>V<sub>1</sub>-ATPase<sup>67</sup> motors have been studied using this technique. A similar labeling approach was used to study the stepping mechanism of the myosin VI motor, obtaining a spatiotemporal resolution of 2 nm and 37  $\mu$ s.<sup>68</sup> Isojima et al. used the technique to visualize intermediate states between the 8 nm steps of the kinesin-1 motor by probing the motion of a kinesin head with a temporal resolution of 55  $\mu$ s and a spatial precision of 1.3 nm.<sup>69</sup> In addition, Nakamura et al. studied the  $\sim$ 50 nm/s stepping movement of *Settatia marcescens* chitinase A and detected the 1 nm forward and backward steps this motion consists of by tracking the position of the scattering label with 0.3 nm localization precision and 0.5 ms temporal resolution.<sup>70</sup>

In addition to studies using scattering labels like those highlighted above, perforated mirror TIR darkfield microscopy has been used for label-free detection of  $\sim$ 100 nm diameter influenza virus particles, immobilized on glass with a detection limit of  $1.2 \times 10^4$  plaque-forming units (PFU)/mL.<sup>71</sup> The authors used scanning electron microscopy (SEM) and fluorescence microscopy to confirm that the darkfield microscope was capable of imaging single influenza virus particles as opposed to aggregates.

Recently, perforated mirror TIR darkfield microscopy has undergone multiple technological developments. Iino and co-workers introduced an axicon lens into the illumination path to generate an annular illumination profile at the BFP of the objective.<sup>72</sup> This method enabled greater illumination intensities compared to previous implementations, as the illumination intensity was limited by the damage threshold of the objective lens when irradiated with a stationary, focused beam. This illumination scheme improved the localization precision of the technique to 1.3 Å for 40 nm GNPs and 1.9 Å for 30 nm GNPs with 1 ms time resolution. This development was applied to study the stepping motion of processive dynein with 100  $\mu$ s temporal resolution and 0.7 nm localization precision.<sup>73</sup> A further development by the same group introduced a multiple-wavelength illumination scheme, which is capable of tracking different types of metal nanoparticles simultaneously by exploiting their associated plasmon resonances and introducing a spectrometer in the imaging path.<sup>74</sup>

An alternative strategy for separating scattered from background light when using TIR illumination involves introducing a pair of micromirrors close to the back aperture of the microscope objective to couple illumination in and out of the imaging path. This arrangement can yield very high optical efficiency, with 94% of the collected backscattered light passing the micromirrors.<sup>58</sup> In addition, the approach is capable of highly effective background suppression through the interception of back reflections from the objective. The sensitivity of the technique was demonstrated by imaging 20 nm GNPs in water immobilized on a glass coverslip with shot-noise-limited localization precision and a signal-to-background ratio close to 100. As a proof of principle, the authors tracked the position of 20 nm silver and GNPs diffusing at an oil–water interface with  $\sim$ 1 nm spatial precision and 10  $\mu$ s temporal resolution, using stroboscopic illumination.

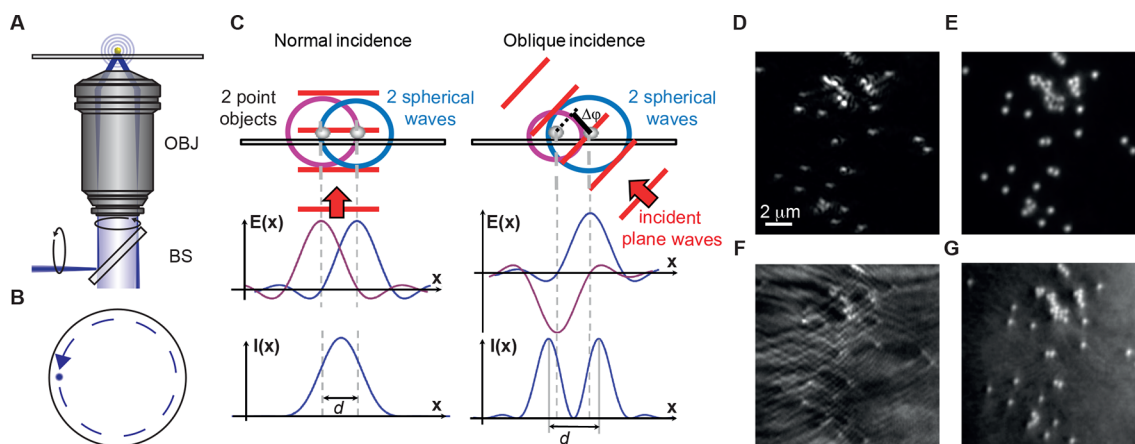


**Figure 3.** ROCS microscopy principle and representative results. (A) Schematic of ROCS microscopy. OBJ, objective; BS, beamsplitter. (B) Translation of the illumination beam in a ring pattern around the back aperture of the objective lens. (C) Schematic of interference between adjacent scatterers  $<math><math><math>E(x)</math></math> and https://creativecommons.org/licenses/by/4.0/. (D–G) adapted with permission from ref 91. Copyright 2018 Optical Society of America.$

In addition to tracking the location of the scattering label, polarization-sensitive darkfield microscopy is capable of simultaneously determining the orientation of gold nanorods (GNRs)<sup>75</sup> due to the strongly polarized scattering response of the nanoparticle.<sup>37,76</sup> In a recent demonstration of this concept, Mazaheri et al. tracked 71 nm  $\times$  25 nm GNRs diffusing on a supported lipid bilayer with a temporal resolution of 2.3  $\mu$ s, lateral localization precision of 3 nm, and rotational precision of 4 $^\circ$ , using a polarization-sensitive objective-type TIRS microscope.<sup>77</sup>

### 3.3. Rotating Coherent Scattering Microscopy

As noted by Abbe in 1873, oblique, coherent illumination of a sample results in a factor of 2 improvement to the achievable spatial resolution when compared to illumination at normal incidence,<sup>31,78</sup> due to higher orders of diffraction being collected by the objective lens. Illuminating two adjacent objects at an oblique angle and in the direction of the alignment of the two objects results in a time-delay between the illumination of each object. For coherent illumination, this induces a phase-offset between the scattered fields emanating from the two objects, which interfere at the detector (Figure 3C). Destructive interference between the scattered waves allows an intensity separation of the two objects at a distance of  $\sim\lambda/4$  apart. Many structured coherent illumination and synthetic aperture imaging techniques have demonstrated improved resolution by leveraging this effect.<sup>79–83</sup>

When illuminating complex samples containing multiple scattering objects in this way, however, the interference of coherent scattering events produces unwanted speckle patterns and interference artifacts. One approach of overcoming these artifacts is to illuminate the sample sequentially from all directions. In this way, for any orientation of adjacent objects, there will be two instances where they are illuminated from opposite directions along their alignment axis. Incoherent addition of the coherent images results in a suppression of the coherence artifacts and a strong separation contrast. This concept is the basis for rotating coherent scattering (ROCS)

microscopy, which was first introduced by Rohrbach and co-workers.<sup>84–88</sup>

In the first iteration of TIR darkfield ROCS microscopy, a spatial light modulator was used to deflect the illumination beam to acquire 72 partial images, each taken with TIR illumination at a different azimuthal angle, which were incoherently averaged to obtain a final image.<sup>84</sup> In this experimental setup, the scattered light was separated from background light by placing a field stop in a plane conjugate to the objective's BFP. In proof-of-principle experiments, 190 nm polystyrene beads were imaged in water to showcase the improved spatial resolution. A potential downside of ROCS microscopy is that minor image distortions are introduced,<sup>78</sup> with scattering objects appearing to be located further apart than their physical distance.

Introducing a two-axis scan mirror, which scanned the beam in a ring pattern across the BFP of the objective within a single exposure of the detector (Figure 3A,B),<sup>85</sup> removed the need for post processing and enabled an acquisition rate up to 100 Hz. The technique was applied to image J774 mouse macrophages and 200 nm thin helical bacteria with a frame rate of 63 and 100 Hz, respectively, achieving spatial resolution of  $\sim$ 150 nm despite the decrease in effective NA of the optical system due to the field stop blocking the reflected illumination beam in the detection path. The authors demonstrated the improvement in spatial resolution, by comparing TIR-ROCS images with TIRF images acquired using the same objective lens and a similar detection wavelength, which yielded a spatial resolution of  $\sim$ 210 nm. Alternatively, darkfield ROCS can be performed without relying on TIR, which can be advantageous when studying species which are located away from the surface of the coverslip.<sup>89</sup> The authors used this approach in conjunction with optical tweezers and interferometric BFP tracking to study the bending of microtubules attached to optically trapped beads.

In addition to operating in darkfield mode, ROCS can be operated in brightfield mode by removing the darkfield stop, enabling interference between the collected scattered light and the back-reflected light. Brightfield ROCS was introduced by Jünger and Rohrbach, who used it in combination with TIR-darkfield ROCS to investigate the activity of the cytoskeleton of

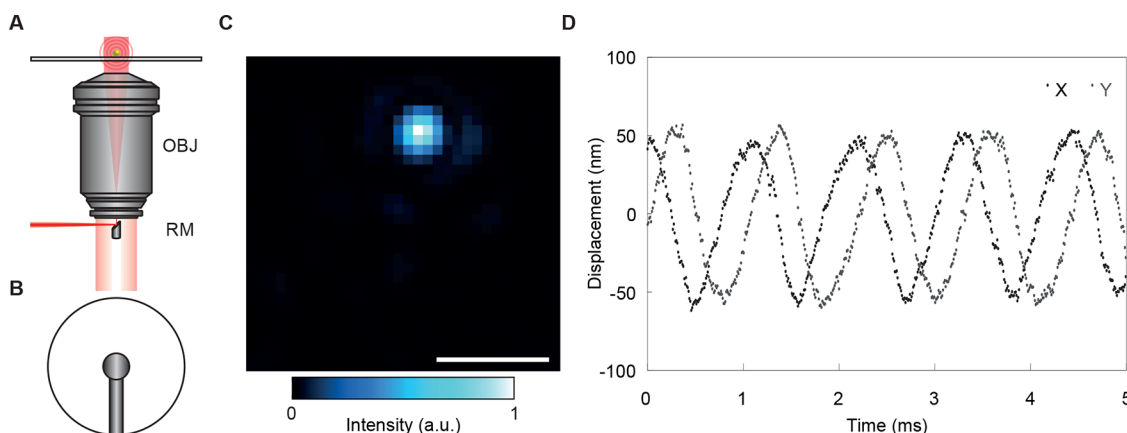


**Figure 4.** Schematic and data from an objective coupling mirror darkfield microscope. (A) Schematic of the experimental setup. OBJ, objective lens; RM, rod mirror. (B) View from the back aperture of the objective looking down the optical axis toward the rod mirror. (C) Image of a 100 nm GNP attached to a flagellar motor on top of an *Escherichia coli* cell, scale bar = 1  $\mu\text{m}$ . (D) Traces of the displacement of a 100 nm GNP attached to a bacterial flagellar motor, the black and gray lines correspond to X and Y displacement, respectively. (C,D) Adapted with permission from ref 95. Copyright 2010 AIP Publishing.

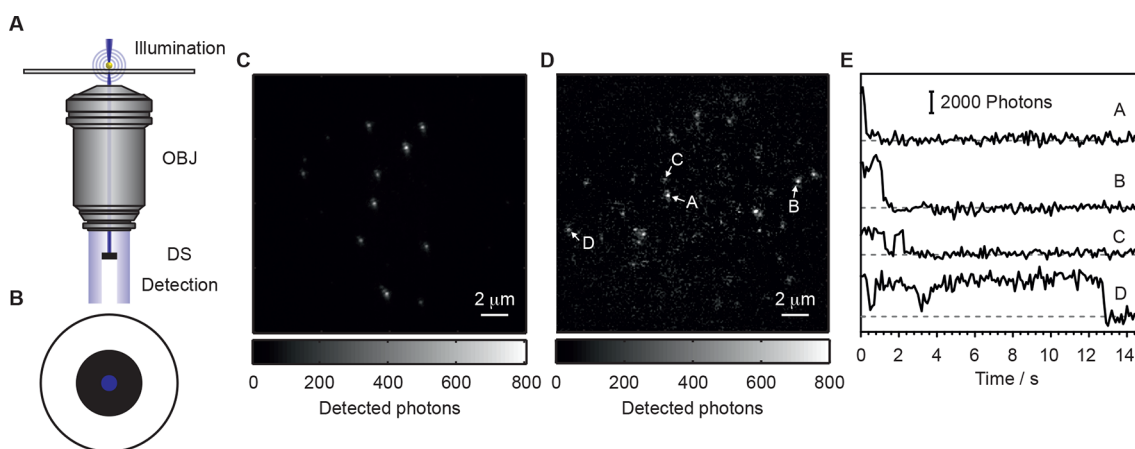


**Figure 5.** Darkfield stop schematics and performance. (A) Schematic illustrating the separation of illumination and scattered light. OBJ, objective; DS, darkfield stop. (B) View from the back aperture of the objective lens looking along the optical axis toward a 4 mm darkfield stop. (C) Image of 20 nm GNPs in water with 1 ms integration time. (D) Fluorescence image of ATTO 610 molecules without the use of an optical filter with 100 ms integration time. (E) Traces of the fluorescence emission of the molecules labeled in (D). (C–E) adapted with permission from ref 42. Copyright 2014 American Chemical Society.

J774 mouse macrophages.<sup>90</sup> This approach was further developed by utilizing the full collection efficiency of a 1.46 NA objective lens, leading to higher detection NA at the expense of lower imaging contrast, relative to an identical setup with a darkfield stop in the detection path.<sup>91</sup> This was demonstrated by imaging 200 nm polystyrene beads with both imaging modalities (Figure 3D–G). In both darkfield and brightfield ROCS, it is clear that the coherence artifacts present in images acquired with illumination from a single oblique angle are not present in images acquired with the illumination averaged over all azimuthal angles. By controlling the spatial coherence of the illumination light with a rotating diffuser, the authors showed that maximizing the spatial coherence of the illumination light leads to optimum image contrast and resolution.

### 3.4. Objective Coupling Mirror

In addition to operating with TIR illumination described above, efficient separation of illumination from detection can be achieved in epi-illumination by a single, small mirror which directs the illumination into the objective lens and allows the returning scattered light to pass. This concept was implemented

by Xie and co-workers, who used a small circular mirror attached to a glass window to couple the illumination beam diagonally into the objective.<sup>92</sup> The small mirror enabled the majority of scattered and reflected light to pass, with separation obtained by inserting a field stop after the first lens in the detection path, due to the offset locations of the scattered and reflected light image planes. The authors used this microscope to track 100–150 nm GNPs endocytosed within lysosomal vesicles inside live cells, moving along microtubules and being transported by molecular motors, with 25  $\mu\text{s}$  temporal resolution and 1–2 nm spatial precision using a quadrant photodiode (QPD) in detection. The diagonal illumination approach used in this microscope was adapted from the scheme developed by Nishiyama et al., who combined transmission darkfield microscopy with an optical trap and demonstrated the presence of  $\sim 4$  nm substeps within the 8 nm step of kinesin.<sup>48</sup> The  $\sim 4$  nm substeps elucidated in this study were recently observed using multiple different techniques.<sup>93,94</sup>

An alternative version of this approach was developed by Berry and co-workers. In their version, a small rod mirror situated close to the back aperture of the objective lens directs



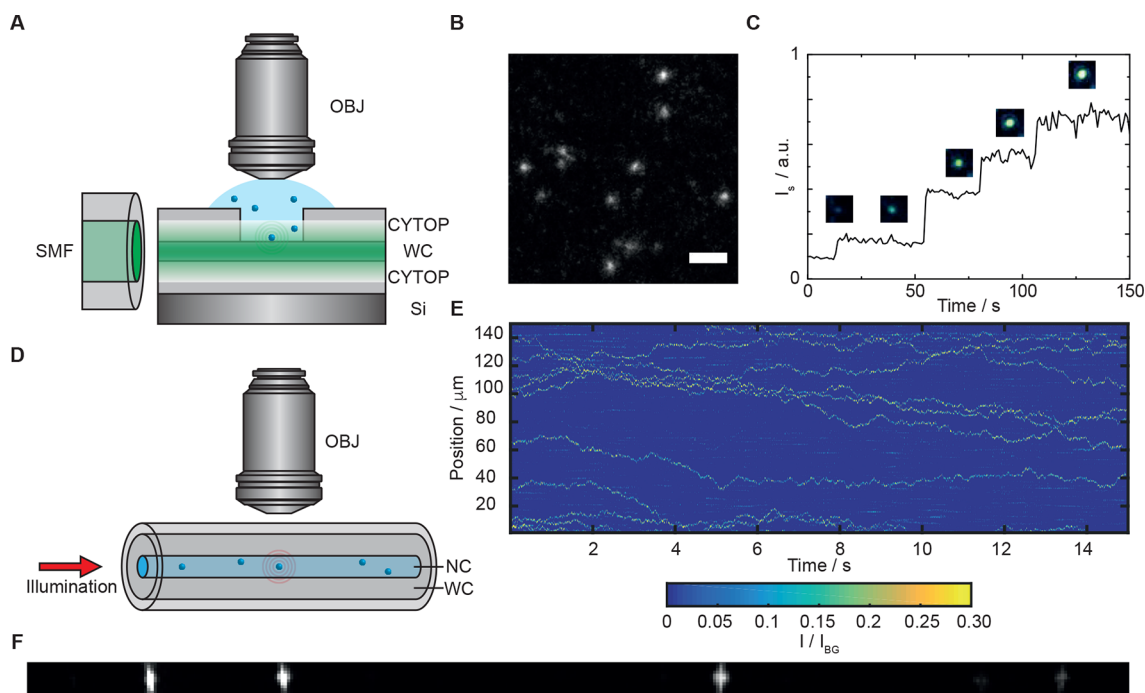


**Figure 6.** Darkfield imaging in optical waveguides. (A–C) Evanescent scattering using waveguide illumination. (A) Schematic of the experimental setup. OBJ, objective; SMF, single mode fiber; WC, waveguide core. (B) Image of 150 nm fluorescently labeled lipid vesicles, scale bar = 2  $\mu\text{m}$ . (C) Scattering intensity trace of 18 nm GNPs binding to a 100 nm lipid vesicle. (D–F) Darkfield imaging in a nanofluidic optical fiber. (D) Schematic of experimental design. OBJ, objective; WC, waveguide core; NC, nanochannel. (E) Example traces of CCMV virions diffusing in the optical fiber. (F) Image of a mixture of 19–51 nm polystyrene beads. (B,C) adapted with permission from ref 106. Copyright 2015 American Chemical Society. (E,F) adapted with permission from ref 112. Copyright 2015 American Chemical Society.

the illumination along the optical axis (Figure 4A).<sup>95</sup> The rod mirror and its mount blocked less than 10% of the area of the back aperture of the objective lens while intercepting back reflections from the objective and interfaces within the sample due to its position (Figure 4B). They tested the microscope performance by imaging a 100 nm GNP bound to a flagellar motor on top of an *Escherichia coli* cell (Figure 4C). The low background signal from the *Escherichia coli* cell, relative to the signal generated by the 100 nm GNP, was attributed to the poor backscattering efficiency of the cell, as the cell is a significantly larger particle which scatters the majority of the light in the forward direction - a potential benefit for further in vivo applications. As a proof-of-principle demonstration, the microscope was also used to track the rotation of the bacterial flagellar motor at a frame rate of 110 kHz by labeling the hook of the motor with a 100 nm GNP (Figure 4D). Further in vivo studies of that motor using the same technique generated torque-speed curves of the motor under various conditions and allowed measurement of stepwise speed changes at low load.<sup>96,97</sup>

As a further demonstration of epi-illumination objective coupling mirror darkfield, Noji and co-workers employed polarization-sensitive detection<sup>75</sup> and defocused image analysis<sup>98</sup> to track both the position and orientation of 80 nm  $\times$  40 nm GNRs, with 10  $\mu\text{s}$  temporal resolution and  $\sim 1^\circ$  azimuthal angle precision.<sup>99</sup> In addition to determining the azimuthal angle, the defocused image analysis method was capable of simultaneously extracting the polar angle of the GNRs with  $\sim 1^\circ$  precision.

### 3.5. Darkfield Stop

Another strategy to obtain efficient separation of background and scattered light combines a field stop with transmission illumination (Figure 5A).<sup>42</sup> This strategy leads to highly efficient

background suppression ( $>10^7$ ) because the illumination beam does not pass through the objective toward the sample, significantly reducing reflections being directed toward the camera. In the setup devised by Weigel et al., the darkfield stop was fabricated from blackened aluminum and was significantly larger than the illumination beam, sacrificing scattered light collection efficiency for superior background suppression (Figure 5B). The sensitivity of the microscope was demonstrated by imaging 20 nm GNPs in water immobilized on a glass coverslip (Figure 5C) and 10 nm GNPs binding to a glass coverslip in water at an acquisition rate of 100 Hz. The high background suppression enabled single molecule fluorescence detection without the use of an optical filter (Figure 5D,E).

### 3.6. Darkfield Imaging Using Optical Waveguides

In addition to objective-based darkfield microscopy, the sample can also be illuminated by an evanescent field generated as the light propagates through a waveguide. In waveguide scattering microscopy (WSM), the scattered light is efficiently separated from the background by aligning the illumination and detection pathways orthogonal to each other (Figure 6A,D). Evanescent illumination using waveguides has also been utilized in fluorescence microscopy.<sup>100–102</sup>

WSM was first introduced by Thoma et al. in 1997, who applied the technique to image thin films using an evanescent field penetrating the surface of an ion-exchanged slab waveguide.<sup>103</sup> One advantage of waveguide-based evanescent illumination over objective-based evanescent illumination is that the depth of the evanescent field can be tailored over a much larger range by adapting the geometry and refractive indices of the materials used to construct the waveguide.<sup>101</sup> In addition, the orthogonal placement of the objective lens relative to the guided wave removes the need for placing reflective optics,

apertures, or beam blocks in the detection path, and a much larger field of view (FOV) can be illuminated. Ni et al. applied the technique to nanoparticles by imaging GNRs as small as  $85 \pm 9 \times 30 \pm 4$  nm, coated on the core surface of an etched multimode optical fiber.<sup>104</sup> Cahoon and co-workers built on this concept by imaging  $\sim 150$  nm  $\times$  50 nm GNRs and silicon nanowires with diameters down to 50 nm, using glass coverslips and microscope slides as waveguides.<sup>105</sup> In this study, the authors presented different experimental configurations capable of detecting the forward and backscattered light from the nanoparticles.

Agnarsson et al. introduced a waveguide chip that was capable of single particle fluorescence and scattering measurements (Figure 6A).<sup>106,107</sup> In this technique, the sample was exposed to the core of the waveguide by etching a sample well into the polymer cladding layer on top of the silica core (Figure 6A). Light was coupled in to the single-mode waveguide via a single-mode fiber, which generated an evanescent field that penetrated the core–water interface. Particles binding to the core–water interface were detected through scattering of the evanescent field, which was collected by a water immersion objective lens oriented perpendicular to the waveguide. To generate a low-intensity background, the waveguide chip was constructed from an extremely smooth silica core sandwiched between two layers of CYTOP, a fluorinated polymer with a refractive index of 1.34, close to that of water. As a proof-of-concept experiment, the chip was used to image fluorescently labeled lipid vesicles with a diameter of 150 nm, demonstrating that the chip was capable of detecting the light scattered by biological nanoparticles (Figure 6B). Furthermore, the technique was used to analyze the kinetics of phospholipase A2 enzymes digesting 100 nm vesicles and to image individual 18 nm GNPs binding to lipid vesicles with a diameter of 100 nm (Figure 6C). Building on this initial work, the technique was applied to analyze the size-dependent binding of ligand-functionalized GNPs to lipid membranes.<sup>108</sup> In other studies, the chip's ability to enable imaging of single vesicles using both scattering and fluorescence has been used to study the formation of lipid membranes,<sup>109</sup> the lipid content of extracellular vesicles,<sup>110</sup> and the effect of the addition of monomeric  $\alpha$ -synuclein on various types of lipid vesicles.<sup>111</sup>

In addition to utilizing the evanescent field that is generated as the light propagates through the waveguide, it is also possible to illuminate with the guided laser mode directly. Manoharan and co-workers designed a single-mode silica fiber containing a subwavelength cylindrical nanofluidic channel to image nanoparticles with high levels of sensitivity (Figure 6D).<sup>112</sup> The nanoparticles were illuminated with a guided optical mode that was coupled into the fiber using a low-magnification objective lens. A portion of the light scattered by the nanoparticles was collected by an oil immersion objective, which was oriented perpendicular to the illumination. The fiber exhibited very low background scattering, leading to a low-intensity, stationary background which was removed computationally. In proof-of-principle experiments, a mixture of polystyrene beads ranging from 19 to 51 nm traveling through the fiber were imaged and tracked with a frame rate of 1 kHz (Figure 6F). The localization error of the technique ranges from  $<50$  to 300 nm depending on the size of the nanoparticle, with the error largely induced by motion blur at the limited frame rate of the detector. In addition, the technique was used successfully to image and track wild-type cowpea chlorotic mottle virus (CCMV) virions with a diameter of 26 nm (Figure 6E), and was capable of operating with frame rates of up to 3.5 kHz. Building on this work, Faez et al.

developed a technique termed nanocapillary electrophoretic tracking (nanoCET), which combined the technique described above with two microelectrodes, both oriented perpendicular to the fiber and situated along its plane.<sup>113</sup> An alternating voltage was applied between the two electrodes to drive a 60 nm GNP back and forth along the channel at a frequency of up to 200 Hz, leading to measurements of the electrophoretic mobility of the particle at a frame rate of 2 kHz.

Jiang et al. advanced fiber-based scattering microscopy by introducing an optical fiber capable of tracking nanoparticles in three dimensions.<sup>114</sup> The microfluidic channel was displaced from the core of the fiber in one dimension so that a homogenized evanescent field was generated in this dimension of the channel. This enabled the 3D position of the particle to be extracted by analyzing the location and intensity of the PSF. Proof-of-principle experiments tracked 50 nm GNPs in three dimensions at a frame rate of 2 kHz, with  $<3$  nm and  $\sim 21$  nm localization accuracy in the lateral and axial dimensions, respectively. In this initial study, to obtain the evanescent illumination conditions described above, the refractive index of the liquid in the microchannel was set to 1.44. Improvement of the data analysis procedure extended this method to more complex illumination profiles, enabling the channel to be filled with water and paving the way to biological studies.<sup>115</sup> Another technological development was introduced by Förster et al., who incorporated a hollow-core fiber with a channel diameter over an order of magnitude larger than that used by Manoharan and co-workers.<sup>112,116,117</sup> This fiber enabled more particles to be studied simultaneously. In initial experiments, 40 nm GNPs and *Escherichia coli* virus  $\lambda$  phages were imaged and tracked. In those experiments, the sensitivity was lower than in aforementioned experiments conducted by Manoharan and co-workers due to the incorporation of a low-magnification, low-NA oil immersion objective, as resolution and the collection efficiency were sacrificed in exchange for a large depth of field.

## 4. INTERFEROMETRIC IMAGING

### 4.1. Introduction

Since the introduction of PCM in 1935,<sup>16</sup> many optical microscopy technologies have employed interference as the contrast mechanism. Despite the developments introduced by DIC microscopy,<sup>19,20</sup> IRM,<sup>21</sup> and RICM,<sup>23</sup> ultrasensitive optical detection of nonfluorescent nano-objects remained largely limited to darkfield microscopy. As discussed in the previous section, however, the square-dependence of the optical signal intensity on object volume in darkfield microscopy has resulted in real-world limitations to the achievable detection sensitivity. These limitations can be circumvented to some degree by the introduction of a reference light field to the optical signal. The resulting intensity at the detector,  $I_d$ , then becomes a superposition of the reference field,  $E_r = E_r e^{i\phi_r}$ , and the field scattered from the probed nano-object,  $E_s = E_s e^{i\phi_s}$ , such that eq 4 now reads:

$$I_d = |E_r + E_s|^2 = I_r + I_s + 2E_r E_s \cos \phi \quad (6)$$

where  $I_r$  and  $I_s$  represent the intensity of the reference and scattered light respectively, and  $\phi = \phi_r - \phi_s$ , represents the phase offset between the reference and scattered fields. As the particle size decreases, the pure scattering term decreases rapidly in magnitude such that, for subwavelength nano-objects, the detected irradiance can be approximated as

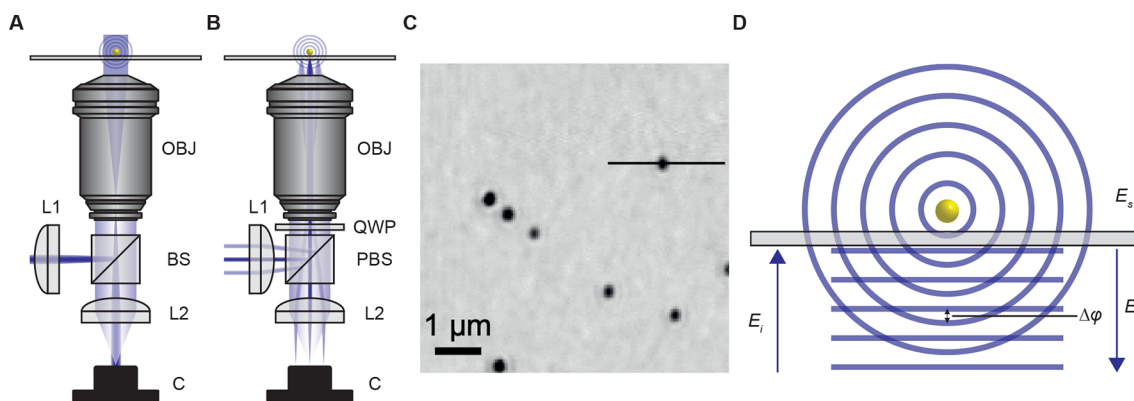


**Figure 7.** Interferometric scattering microscopy principles and example experimental arrangements. (A) Schematic of widefield illumination iSCAT. (B) Schematic of rapid beam scanning illumination iSCAT. OBJ, objective; BS, beamsplitter (nonpolarizing); QWP, quarter-waveplate; PBS, polarizing beamsplitter; L1, illumination lens; L2, imaging lens; C, camera. (C) Confocal detection iSCAT image of 20 nm GNPs on a glass coverslip in water. (D) Principle of interferometric scattering microscopy,  $E_i$  incident field,  $E_s$  scattered field,  $E_r$  reflected reference field,  $\Delta\phi$  phase difference between the scattered and reflected fields. (C) Adapted with permission from ref 121. Copyright 2006 Optical Society of America.

$$I_d \approx I_r + 2E_r E_s \cos \phi \quad (7)$$

Unlike darkfield microscopy, the presence of reference light dominates the detected intensity, and any analyte signal appears as a small perturbation in the final image with contrast,  $c$ , given by

$$c = \frac{I_d - I_r}{I_r} = \frac{2E_r E_s \cos \phi}{I_r} = \frac{2E_s}{E_r} \cos \phi \quad (8)$$

The potential for ultrasensitive optical detection with interferometric scattering as the contrast mechanism stems from the linear proportionality of the signal to the nano-object volume, as opposed to the square dependence in darkfield imaging. Detection based on interferometric scattering differs from darkfield imaging in two further significant ways. First, the magnitude of the interferometric term is not only determined by the electric field amplitude but also by the phase difference between the interfering fields. Second, the challenge involves the detection of the interferometric term, which is not only much smaller than the reference field but can be lost among unwanted interferometric signals. It is these two parameters that current methods thus focus on: optimizing the phase difference between incident and scattered light and the relative magnitudes of  $E_r$  and  $E_s$ , which does not affect the nominal measurement sensitivity but is important for matching the detected light intensity to the capabilities of the detector and the ability to fine-tune the focus of the microscope.

Similar to darkfield imaging and the precursors to modern interferometric detection technologies, the ultimate challenge for ultrasensitive optical detection with interferometric scattering remains the same: eliminating background signatures that overwhelm the signal, in this case the interferometric term. These can be largely attributed to two sources: (1) Additional background light, often due to spurious back-reflections from optics and backscattering from rough detection surfaces. (2) Shot-noise-induced fluctuations in the detected reference light,  $|E_r|^2$ , which can mask a small interferometric signal.

In terms of background scattering, the advantage of interferometric approaches is the weaker, linear, scaling with object volume, meaning that the detected signal drops more slowly for smaller objects. It is important, however, to recognize that this difference in scaling does not make interferometric detection significantly more sensitive than darkfield imaging

(within a factor of  $\sqrt{2}$ ). The main reason why interferometric methods have been more successful than darkfield methods at detecting the smallest objects in recent years comes down to limitations of dynamic range in detection coupled with the unavoidability of a certain level of background scattering as a result of imperfect surfaces. As an example, while it may be feasible to detect a signal that is 1/100 of the background in interferometric imaging, the same challenge in darkfield imaging would amount to detecting a signal that is 1/10000 of the background.

In terms of the signal-to-noise ratio of the measurement, the initial challenge is to ensure that the measurement is mainly limited by shot noise, rather than by other noise sources, such as mechanical vibrations, laser intensity noise, or background fluctuations. Suppressing these additional noise sources becomes a more significant challenge as the shot-noise-induced fluctuations are reduced to the levels required for single-molecule detection. In addition to this, detecting a sufficient number of photons to reach such noise-floor levels might require the signal from detector pixels or recorded frames to be averaged together, thus sacrificing localization precision and temporal resolution, respectively. The temporal averaging of consecutive frames increases the effective full well capacity of the detector, however, as the averaging window is increased, nonshot-noise contributions, such as sample drift, become increasingly prominent. This results in the breakdown of the  $\text{SNR} \propto \sqrt{N}$  relationship for larger averaging windows (>50 ms). In this section, we discuss a variety of recent methods that attempt to optimize the phase and amplitude of  $E_r$  to varying degrees, depending on the specific application and the magnitudes of the noise.

#### 4.2. Interferometric Scattering Microscopy I: Single Particle Tracking

Interferometric scattering microscopy (iSCAT) can, in its simplest form, be thought of as the laser-illumination equivalent of IRM,<sup>21,22</sup> in which the stability of a common-path geometry (whereby the interfering light fields share a near-identical optical path to the detector) is coupled with the reference field attenuation and axial sensitivity of a reflection-based configuration. In reflection-based microscopes, the majority of the incident light is transmitted such that the reference field intensity is essentially a measure of the reflectivity at the substrate–sample interface. While this does improve the image



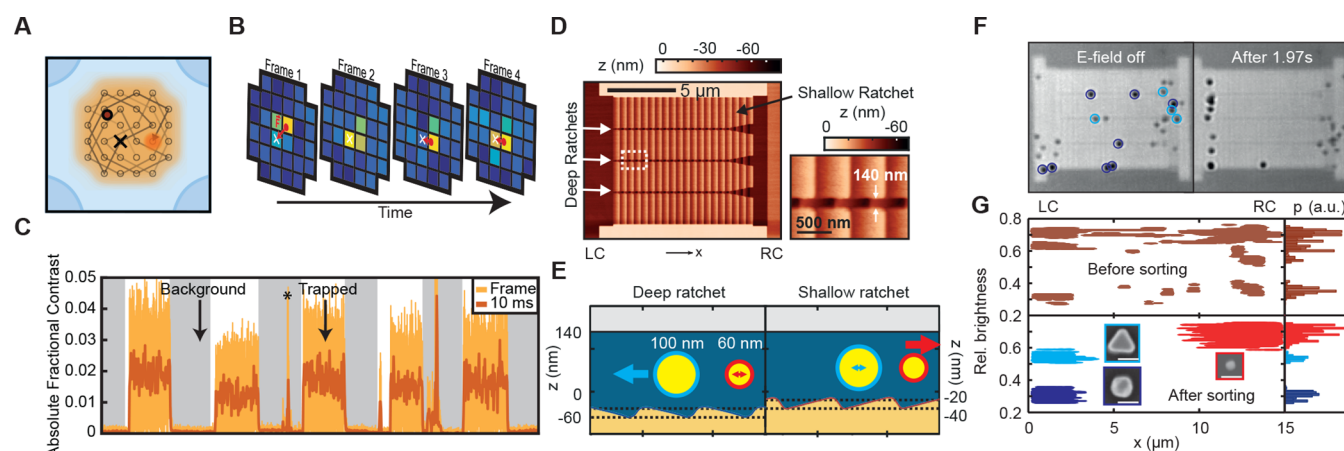


**Figure 8.** Combination of interferometric scattering detection and single particle traps. (A–C) Anti-Brownian electrokinetic trap (ISABEL). (A) Illustration of the scanning pattern of the illumination beam. (B) Schematic of the trapping algorithm. (C) Trace of iSCAT contrast with time of a trapped 40 nm GNP. (D–G) Nanofluidic rocking Brownian motor capable of sorting GNPs based on their size. (D) Topography of the sorting device. (E) Schematic of the method of separation of 60 and 100 nm GNPs. (F) iSCAT images displaying the separation of 60 and 100 nm GNPs. (G) Plot of position vs median relative brightness of the particles in the device before and after sorting. (A–C) Adapted with permission from ref 144. Copyright 2019 American Chemical Society. (D–G) Adapted with permission from ref 149. Copyright 2018 The American Association for the Advancement of Science.

contrast compared to that of an analogous transmission-based microscope, it is important to note that it does not improve the overall shot-noise-limited SNR of the experiment, due to the overall photon deficit and the resulting effect on the shot noise. Though the term iSCAT was first coined by the Sandoghdar group,<sup>118</sup> its earliest practical implementation was reported using a laser-scanning confocal microscope equipped with a 50:50 beamsplitter imaging microtubules at a glass–water interface.<sup>119</sup> The resulting images exhibited a remarkable signal-to-background ratio of  $\sim 10$ , implying a detection limit on the order of  $\sim 300$  tubulin monomers and making this early reflective laser microscope one of the most powerful label-free biosensors of the time. Lindfors et al. then used a reflective laser microscope with sample scanning to demonstrate record detection sensitivity and spectroscopic characterization of GNPs down to 5 nm in oil,<sup>120</sup> a concept that quickly expanded to biological environments<sup>121</sup> and virus detection and tracking.<sup>122</sup> Static detection sensitivity has reached as far as cadmium selenide quantum dots<sup>123</sup> and 2 nm gold particles on suitable substrates.<sup>124</sup>

Two illumination schemes are widely used in iSCAT microscopy: widefield and rapid beam scanning. Widefield illumination uses a lens to focus the illumination into the BFP of the objective, yielding effectively plane-wave illumination of the sample (Figure 7A). This illumination scheme is the method of choice for obtaining the highest possible temporal resolution, as the acquisition rate is not limited by the rate of beam scanning. The second illumination scheme, rapid beam scanning illumination, uses a pair of acousto-optic deflectors (AODs), which scan a focused beam across the sample, generating an even illumination profile while removing ring artifacts and reducing speckle patterns observed in widefield iSCAT (Figure 7B). This illumination approach has often been implemented in combination with a polarization-dependent method to separate the signal from the illumination path using a quarter-wave plate (QWP) and polarizing beamsplitter (PBS), to maximize collection efficiency. The progress of iSCAT over the past decade, as well as the historical context of its development from technological precursors, have been covered in detail in recent

reviews.<sup>125–128</sup> Here, we will focus on recent technological developments in the context of single-particle tracking (SPT).

For SPT, localization precision and imaging speed are ultimately limited by the number of photons that can be detected from the scatterer in a finite time window. Nanoparticles, specifically (GNPs), are commonly used as labels as they are inert, provide a strong extinction signal due to their polarizability, and do not suffer the drawbacks of fluorescent alternatives. Laser-based illumination provides access to incident photon intensities only limited by sample damage and detector full-well depth. As a result, high spatiotemporal resolution can be obtained through a variety of combinations of lateral localization precision and temporal resolution depending on the experimental requirements due to the trade-off between these two parameters. For example, in a recent study, the tracking of 20 nm GNPs was performed with a 2 nm precision, on the  $\mu\text{s}$  time scale.<sup>129</sup> More recently, this has been pushed toward an acquisition rate of 913 kHz and sub-10 nm localization precision for 20 nm GNPs diffusing on a supported lipid bilayer.<sup>130</sup> The sensitivity and measurement precision achievable with iSCAT has enabled optimization of nanoparticle binding<sup>131</sup> and the study of mobility differences between supported and suspended bilayer membranes.<sup>132</sup>

In addition to studying membrane mobilities, iSCAT has recently found applications in elucidating the mechanisms of molecular motor processivity.<sup>94,133,134</sup> For example, iSCAT was used to track the position of 30 nm GNP scattering labels attached to the motor domains of kinesin-1 motor proteins, with a localization precision of  $\sim 2$  nm at an acquisition rate of 1 kHz.<sup>94</sup> More recently, studies have emerged that take advantage of the high spatiotemporal resolution of iSCAT to visualize and characterize the dynamics of cytoskeletal filaments, specifically microtubules.<sup>135</sup> Maintaining the imaging capabilities of iSCAT requires highly efficient suppression of background signals, which is relatively straightforward in the aforementioned scenarios but much more challenging in the presence of large objects, such as cell bodies. While in principle, background subtraction approaches can be employed, they are limited to any changes that occur in the background during the desired

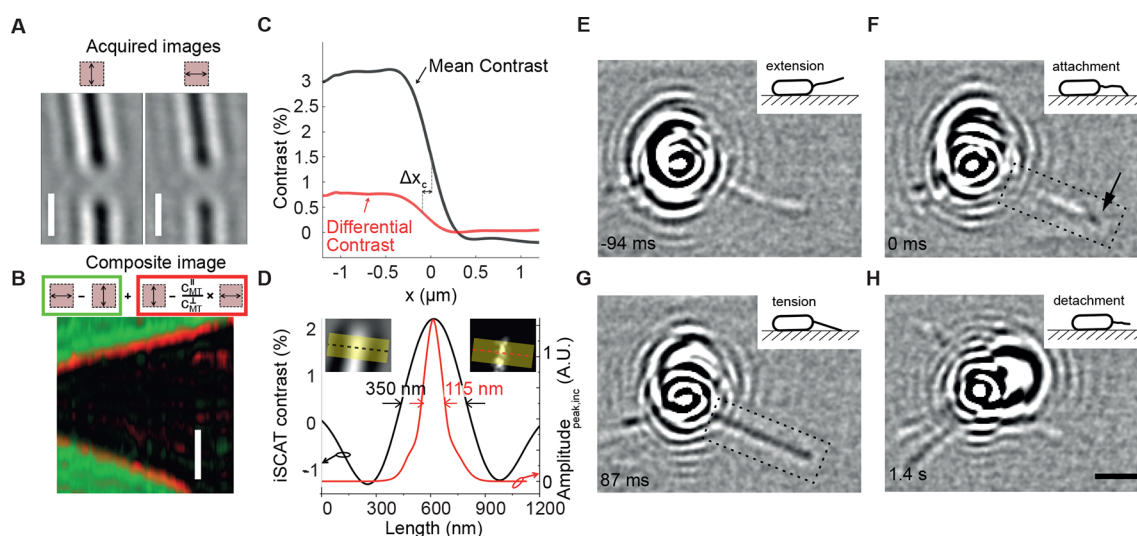


**Figure 9.** Interferometric scattering microscopy of microtubules and type IV pili. (A) Images of a microtubule acquired with light polarized parallel (left) and perpendicular (right) to the microtubule. Scale bar:  $1\ \mu\text{m}$ . (B) Composite kymograph of isotropic (red) and anisotropic (green) scattering combined. Scale bars:  $1\ \mu\text{m}$  (vertical) and  $1\ \text{s}$  (horizontal). (C) The profile of the mean contrast (black) and anisotropic contrast (red) averaged from disassembling microtubules. (D) Cross sections of the iSCAT (top left) and super-resolved (top right) microtubule images inset. (E–H) iSCAT images of different steps in the type IV pili cycle of a *Pseudomonas aeruginosa* cell, scale bar =  $2\ \mu\text{m}$ . (E), (F), (G), and (H) correspond to extension, attachment, tension, and detachment, respectively. (A–D) Adapted with permission from ref 154. Copyright 2021 John Wiley and Sons. (E–H) Adapted with permission from ref 155. Copyright 2019 Springer Nature.

exposure time, resulting in studies so far being limited to labels of  $30\ \text{nm}$  diameter or larger.<sup>136–138</sup>

An additional challenge, and opportunity, of performing iSCAT on cells is the fact that the labels no longer diffuse only in 2D, where the phase relationship between scattered and reflected light is constant, but also in 3D, where it varies rapidly with the distance of the label from the reflective cover glass surface. Early studies used a simple interpretation of eq 6 to extract three-dimensional information both in solution<sup>139</sup> and on cells;<sup>137</sup> this was recently replaced by a more sophisticated PSF analysis, which makes it possible to achieve sub- $10\ \text{nm}$  localization precision in both the lateral and axial directions at microsecond acquisition speeds.<sup>136</sup> In this way, the authors could study subdiffusion and nanoscale confinement of GNP-labeled epidermal growth factors in live HeLa cells. Additionally, the trajectory of a GNP-labeled protein was used to reconstruct a map of the nanoscopic topology of cellular structures, such as the surface of a filopodium. Subsequent development of interferometric PSF analysis has built upon this work to further demonstrate the applicability of iSCAT to 3D SPT in live, complex environments.<sup>138,140</sup> The long observation times of these tracking measurements, up to tens of minutes in length, highlights a key advantage of scattering labels compared to fluorescent alternatives.

Alternative approaches to extend iSCAT detection beyond two-dimensional imaging have been explored by Hong, Cho, and co-workers.<sup>141</sup> Remote focusing iSCAT (RF-SCAT), in which imaging depth, and thus the vertical tracking range, is increased by vibration-free vertical image scanning. By implementing an additional  $4f$  telecentric system, the wavefront from the BFP of a high-NA, oil immersion objective, coupled to the sample, can be reimaged into the BFP of a lower-NA, air objective, before being focused onto a reference mirror. The vertical image sections can be selected without movement of the sample stage or imaging objective by translating the axial position of the reference mirror. This optical configuration enabled a trackable depth for nanoparticles of  $10\ \mu\text{m}$ .

The ability to use iSCAT in three dimensions with high levels of sensitivity is important because it removes the need for immobilization on a surface, which can be as perturbative, if not more perturbative, than the incorporation of fluorescent labels. In this regard, the combination of the anti-Brownian electrokinetic (ABEL)<sup>142,143</sup> trap with iSCAT, termed ISABEL, enabling trapping and closed-loop feedback tracking of nanoscale particles in solution is particularly attractive (Figure 8).<sup>144</sup> A challenge compared to other nanoparticle applications arises from the fact that the trapped object is not bound to the glass surface and can move along the optical axis, which causes changes in optical contrast (Figure 7D). The ABEL trap then ensures that the particle is constrained to the trapping region (Figure 8A), through tracking its position with detection rates up to  $10\ \text{kHz}$ , calculating the particle displacement vector from the center and applying an electric field to move the particle back to the center of the trap (Figure 8B,C). In addition to the ISABEL trap, various other single-particle traps have utilized iSCAT detection as an alternative to fluorescence.<sup>139,145–149</sup> The combination of iSCAT detection and single particle traps represents an important advance, especially in the context of the potential future expansion toward single proteins<sup>32,33</sup> and combination with motion control and sorting.<sup>148,149</sup> The incorporation of iSCAT detection in a nanofluidic rocking Brownian motor capable of sorting GNPs into populations based on their diameters was presented by Knoll and co-workers.<sup>149</sup> The device used a combination of deep and narrow ratchets angled to the left, embedded within wide and shallow ratchets angled to the right (Figure 8D). This enabled the separation of  $60$  and  $100\ \text{nm}$  GNPs upon application of an external oscillating electric field, with the  $60\ \text{nm}$  GNPs traveling along the shallow channel to the right and the  $100\ \text{nm}$  particles traveling along the deep channel to the left (Figure 8E–G). The position of the nanoparticles in the device was imaged using iSCAT at an acquisition rate of  $1\ \text{kHz}$ .

### 4.3. Interferometric Scattering Microscopy II: Label-free Imaging

The enhanced interferometric signal generated by the plasmon resonance of GNPs is roughly equivalent to that of a dielectric particle with about twice the diameter of a GNP. Given the size range of many biomolecules, for example, virus particles (20–200 nm), iSCAT is well-suited for imaging such objects without the need for labels. Initial studies reported the label-free optical detection of single virus particles bound to supported membrane bilayer receptors.<sup>118,122</sup> Manoharan and co-workers also tracked the position and orientation of unlabeled bacteriophages to nanometer precision and monitored the changes in iSCAT contrast as a function of virion DNA content.<sup>150</sup> This allowed the DNA ejection dynamics of individual bacteriophages, upon the addition of LambB receptor, to be investigated. Subsequently, the same group quantified the assembly kinetics of individual MS2 bacteriophage capsids around MS2 RNA, identifying features of capsid growth that would otherwise be unresolved in bulk measurements.<sup>151</sup> The iSCAT signal intensities of the RNA genome of MS2 bacteriophages, tethered to a functionalized glass surface, were monitored upon the introduction of MS2 coat-protein dimers. The ratio of the iSCAT signal to the number of coat proteins bound to the RNA strand was sufficient to infer potential assembly pathways.

Another target for label-free iSCAT have been microtubules, as in the original study by Amos and Amos.<sup>119</sup> In that study, the authors imaged microtubules bound to standard microscope cover glass. This was later extended to gliding assays employed by Andrecka et al.<sup>152</sup> As microtubules exhibit anisotropic scattering profiles, their iSCAT contrast is polarization-dependent relative to their orientations, a property previously explored for GNRs in both iSCAT and darkfield modalities.<sup>75,77,99,153</sup> Parallelized polarization-sensitive iSCAT detection recently enabled studies of not only microtubule motion but also disassembly.<sup>154</sup> Differential image contrasts from the two orthogonal polarization projections (Figure 9A) were presented in the form of a composite kymograph (Figure 9B) to show the change in relative isotropic and anisotropic scattering contributions, indicating a mass change at the microtubule tip (Figure 9C). Incremental images, temporally separated by 19 ms, provided quantitative information on disassembly rates and were used to reconstruct super-resolution images which enabled detection of tubulin oligomer detachment, with a theoretical detection limit of ~3 tubulin dimers (Figure 9D). Obtaining the differential contrast from the two orthogonal projections (Figure 9A) enabled reconstruction of super-resolved images and nanoscopic structural changes at the tip of a disassembling microtubule from changes to scattering anisotropy on a submillisecond time scale.

Persat and co-workers transitioned iSCAT imaging of biological filaments toward the cellular context.<sup>155</sup> To achieve this, they imaged type IV pili (TFP), filaments assembled at cell surfaces used by bacteria to attach to surfaces, move and resist flow. These filaments have been challenging to image using light microscopes due to the detrimental effects of fluorescent labeling on the cell's ability to (dis)assemble the filaments, which is central to their function. Using iSCAT, the filaments could be imaged in a label-free fashion (Figure 9E–H), despite the strong scattering background from the cell body. In addition, the dependence of the iSCAT signal on the distance from the glass surface made it possible to differentiate between different functional states, such as extension (Figure 9E), attachment

(Figure 9F), development of tension (Figure 9G), and eventually detachment (Figure 9H).

The ability to detect and image biological nanoparticles in aqueous solution naturally extends to lipids and the structures they form such as lipid nanodomains,<sup>156</sup> lipid bilayers,<sup>157</sup> and micelle and vesicle formation during autocatalytic processes.<sup>158–160</sup> iSCAT is particularly well-suited to this application, as it enables label-free visualization of chemical reactions by monitoring the production or destruction of nanoparticles. While nanoparticle formation can be monitored by bulk methods such as dynamic light scattering (DLS)<sup>161,162</sup> or NMR, the ability to detect individual particles provides access to the earliest stages of nanoparticle formation, often part of the “lag phase” caused by the invisibility of particles at very low concentrations for bulk methods. In addition, single particle detection allows much improved characterization of sample hetero/homogeneity compared to methods providing average particle size only.

### 4.4. Mass Photometry

At the very extremes of sensitivity, iSCAT has been used to detect, image, localize, and track individual proteins in a label-free fashion.<sup>32,33,163,164</sup> The interferometric contrast generated by protein molecules, which are weakly scattering objects, is a function of their refractive index and proportional to their volume. Given that proteins consist of amino acids, which exhibit small variations in refractive index<sup>165</sup> and specific volume,<sup>166</sup> the refractive index contribution to the contrast should be effectively constant, and the volume should be proportional to the mass, resulting in a linear relationship between iSCAT contrast and protein mass. The earliest demonstrations of single-protein iSCAT sensitivity used this relationship to provide evidence for single-molecule sensitivity.<sup>32,33</sup>

Given the enormous power of native mass spectrometry (MS) in the context of studying biomolecular structure and dynamics, label-free single molecule detection, and mass quantification have immense potential.<sup>167,168</sup> Early implementations,<sup>32,33</sup> however, failed to provide the resolution, accuracy, or precision exceeding that of well-established ensemble-based scattering approaches such as DLS.<sup>161,162</sup> Solutions of proteins of different mass could be distinguished, but the resolution was insufficient to quantify mixtures of different species, and the accuracy insufficient to confidently identify species directly by mass, which are some of the key advantages of native MS.

The challenge in nonfluorescent single-molecule imaging relates to the capability of the optical system to distinguish the weak analyte signal from the cacophony of background light contributions. Imaging in a reflective configuration and applying a sliding window background subtraction algorithm to subtract static background can go some way toward addressing this issue.<sup>43</sup> However, a typical iSCAT measurement of single proteins in solution yields image contrasts of approximately 0.4%/MDa of molecular mass.<sup>32,33</sup> Thus, a perfectly shot-noise-limited measurement of a 250 kDa protein, with an SNR of 10, would require the collection of  $10^8$  photoelectrons. Consequently, because of the full-well-capacity limitations of commercially available cameras ( $<10^5$ ), this photoelectron requirement must be fulfilled by means of spatiotemporal averaging, limiting resolution and potentially introducing additional background noise.

In the context of biomolecular mass measurements, and the accuracy and mass resolution demanded by applications in



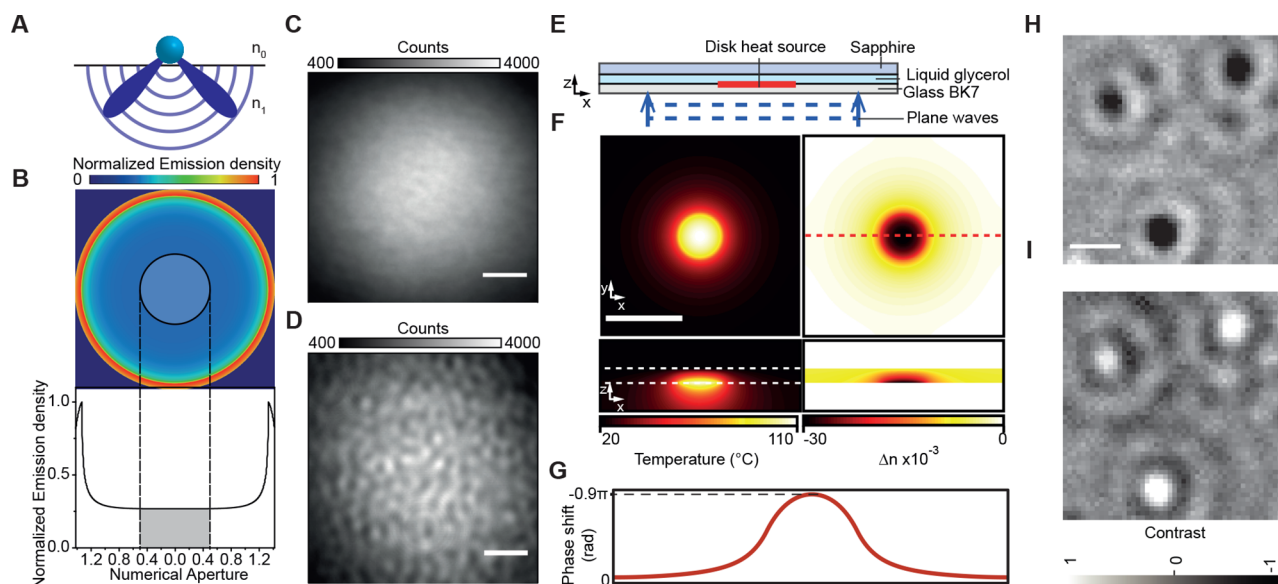


**Figure 10.** Numerical aperture filtered iSCAT. (A) Schematic of the dipole emission pattern for a point scatterer at a refractive index interface;  $n_0$  and  $n_1$  represent the refractive indices of the media ( $n_1 > n_0$ ). (B) Emission pattern at the back aperture of a high-NA (1.42) microscope objective for a nanoscopic scatterer at a glass–water interface illuminated with circularly polarized light. The inner outlined circle indicates the position of the partial reflector (top panel). Normalized emission density as a function of numerical aperture. Gray shaded region corresponds to the position of the partial reflector (bottom panel). (C) Raw iSCAT image of a glass coverslip covered by water. (D) Equivalent image with the addition of a  $T = 1\%$  partial reflector in the optical setup. Scale bar:  $1 \mu\text{m}$ . (E) Illustration of a photothermal spatial light modulator (PT-SLM). (F) XY cross-section of the temperature profile across the PT-SLM (top left panel), equivalent XZ cross-section (top right panel). Scale bar:  $100 \mu\text{m}$ . The two white dashed lines indicate the boundaries of the thermo-optic material. XY cross-section of the resulting refractive index variation (bottom left panel) and equivalent XZ cross-section (bottom right panel). (G) Phase-shift profile of a plane wave propagating through the structure in  $z$  at the position of the red dashed line in (I). (H,I) Normalized iSCAT images of  $30 \text{ nm}$  single gold nanospheres at total heating powers incident on the modulator structure of  $0 \text{ mW}$  (L) and  $110 \text{ mW}$  (M). Scale bar:  $500 \text{ nm}$ . (B–D) Adapted with permission from ref 43. Copyright 2017 American Chemical Society. (E–I) Adapted with permission from ref 169. Copyright 2021 Springer Nature under Creative Commons Attribution 4.0 International License <https://creativecommons.org/licenses/by/4.0/>.

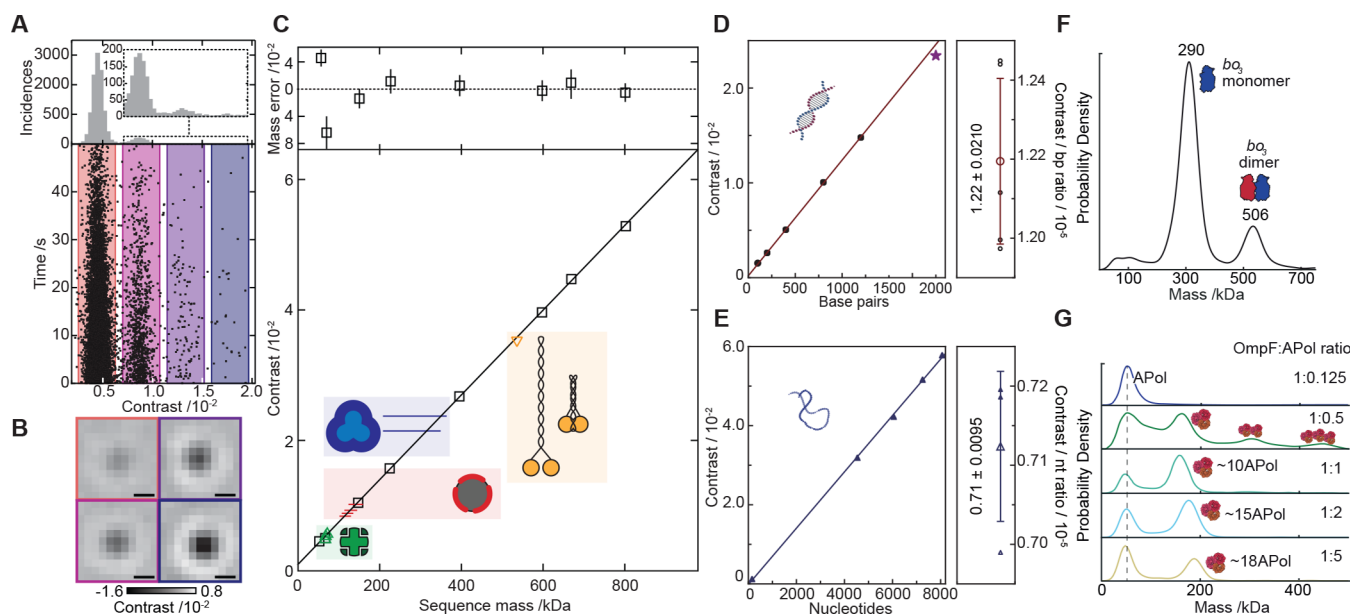


**Figure 11.** Mass photometry principle and applications. (A) Scattering contrast histogram acquired from binding events of  $12 \text{ nM}$  BSA. (B) MP images of a BSA monomer, dimer, trimer, and tetramer, scale bars =  $200 \text{ nm}$ . (C) Contrast to mass relationship for a range of proteins. (D,E) Relationship between contrast and number of base pairs in double-stranded (D) and single-stranded (E) DNA. (F) Mass histogram of *Escherichia coli*  $b_{o3}$  oxidase isolated from lauryl maltose-neo-pentyl glycol detergent micelles. (G) Mass histograms of different ratios of *Escherichia coli* outer membrane protein trimers solubilized in amphipols. (A–C) Adapted with permission from ref 34. Copyright 2018 American Association for the Advancement of Science. (D,E) Adapted with permission from ref 176. Copyright 2020 Oxford University Press under Creative Commons Attribution 4.0 International License <https://creativecommons.org/licenses/by/4.0/>. (F,G) Adapted with permission from ref 185. Copyright 2020 Philipp Kukura.

bioanalytics, at least an order of magnitude improvement in measurement precision at the single molecule level was required. One method to achieve this involves further attenuation of the reference light relative to the scattering signal by exploiting the geometric separation of the two fields, as described in section 2. The placement of a partially reflective metallic film of specified dimensions in the BFP of the microscope objective selectively filters its NA and increases the scattering contrast (Figure 10A–D).<sup>43–45</sup> Again, this does not lead to an improved shot-noise-limited SNR, due to the concomitant reduction in total detected photoelectrons. However, two significant advantages arise from such NA filtering. First, the increased contrast of the substrate surface enables facile and accurate determination of the optimum focus position, which is essential for accurate contrast measurement because of the importance of the phase difference between scattered and reflected light. The second advantage is the ability to use high illumination powers without saturating the imaging detector. However, with the increased contrast provided by the partial reflector, sensitivity to non-Poissonian image perturbations also increases. This is particularly relevant because visualization of single-molecule events require subtraction of the high-contrast, static, speckle-like pattern generated by the surface of a typical glass coverslip (Figure 10D). The increased need for sample stage stability and overall suppression of low-frequency environmental noise resulted in the evolution of a robustly enclosed mass photometer from previous, optical-table-based iSCAT microscopes.<sup>34</sup>

Recent developments in the Piliarik group expanded the general principle of introducing a spatial filter beyond static field attenuation or phase retardation.<sup>169</sup> Replacing the thin metal film disk with a layer of GNRs, the purpose of the spatial filter was not solely to attenuate the reference field but also to change its phase. By sandwiching a layer of thermo-optic material, namely liquid glycerol, between the gold-coated glass substrate and a sapphire heat sink (Figure 10E), the local refractive index of the glycerol can be rapidly altered by microscopic heating (Figure 10F), which in turn results in a phase retardation of the transmitted optical wave (Figure 10G). The refractive index control, spatially confined to the cross-section of the photo-thermal spatial light modulator (PT-SLM), allows the phase offset between the reference and scattered field to be modulated with a switching time of 70  $\mu$ s, a factor of 100 faster than conventional liquid crystal SLM devices. This novel device, incorporated into an iSCAT optical setup, was shown to enable quantitative phase imaging measurements of 3D nanoscopic microtubule displacement.

The application of NA filtering in combination with improvements in the hardware and data analysis led to rapid advancements in the detection sensitivity, precision, and ultimately mass resolution of single-molecule mass measurements.<sup>34</sup> The contrast distributions from a sample of bovine serum albumin (BSA) molecules (66 kDa) now exhibited well-resolved (19 kDa full width at half-maximum (FWHM)), equally spaced peaks as expected for different oligomeric states of the same protein measured using a method sensitive to complex mass (Figure 11A). In addition, mass measurement of a wide range of single protein molecules was possible with up to 2% sequence mass accuracy. This level of accuracy was a desirable aspect of mass photometry (MP) because it dramatically simplifies the identification of unlabeled species by mass, enabling more highly multiplexed detection than is possible with fluorescence labeling. While the lower detection limit of MP ( $\sim$ 40 kDa)<sup>170</sup> is limited by the noise sources

discussed previously, the upper limit is dictated by a number of factors. The linear relationship between iSCAT contrast and mass relies on the assumption that the amplitude of the scattered field is negligible when compared to the reference field, which can be somewhat alleviated by altering the degree of reference field attenuation. In addition to this, as the physical size of the particle exceeds the limits of Rayleigh scattering ( $\sim$ 10% of the illumination wavelength) and beyond, both the emission profile and relative phase of its scattered field will begin to deviate from that of a single molecule. However, in the context of single proteins and other similarly sized biomolecules, given an appropriate mass standard, there is no intrinsic upper limit to MP quantification.

While it is important to note that the current capabilities of MP cannot match those attainable by native MS, the ability to separate different oligomeric states, as well as free and bound complexes as a result of the high single-molecule measurement precision, in combination with label-free detection, single-molecule sensitivity, mass measurement, solution operation, and concentration measurement by molecular counting has resulted in significant adoption of MP since its inception. This includes application to nucleic acids (Figure 11D,E), membrane proteins (Figure 11F,G), and membrane associated proteins.<sup>34,159,171–198</sup> The study of membrane proteins in particular presents an experimental challenge due to the instability of their hydrophobic transmembrane regions in aqueous solution. In the first study applying MP to study membrane proteins, the authors studied both amphipathic vesicles and lipid nanodiscs in order to characterize the particle size, sample purity, and heterogeneity of integral membrane proteins, in addition to identifying their functional states.<sup>185</sup> MP was applied to imaging different oligomeric states of *Escherichia coli* bo<sub>3</sub> oxidase isolated from lauryl maltose-neo-pentyl glycol detergent micelles (Figure 11G). In addition, the authors studied different ratios of *Escherichia coli* outer membrane protein (OmpF) trimers solubilized in amphipols (Apol) (Figure 11F).

The speed, sensitivity, and relative simplicity of a typical experiment mean that MP lends itself naturally to sample characterization for more structure-specific analytical techniques such as cryo-electron microscopy (cryo-EM) and X-ray crystallography.<sup>194</sup> A recent study demonstrated this by using MP to quantify the heterogeneity of macromolecular complexes. The results obtained were comparable to those gathered from corresponding negative stain EM workflows. Similarly, the ability of MP to count individual molecules can be used to accurately determine the relative abundances of different biomolecular complexes in solution, thus yielding information on the associated binding affinities and interaction kinetics.<sup>188,195,196</sup>

#### 4.5. Interferometric Reflectance Imaging Sensor

Interferometric reflectance imaging sensor (IRIS) is an experimental technique combining interferometric imaging principles with a specialized substrate to act as an effective biosensor. In IRIS, the substrate is fabricated from a silicon wafer covered by a thermally grown layer of silicon dioxide, which can be coated with antibodies to facilitate selective binding of a species of interest.<sup>199</sup> Initially, the technique was designed to detect ensemble binding of biomolecules to a surface by measuring the thickness of the accumulated layer of biomass.<sup>200</sup> Subsequently, the technique demonstrated the ability to detect and image single particles, in a modality termed single particle

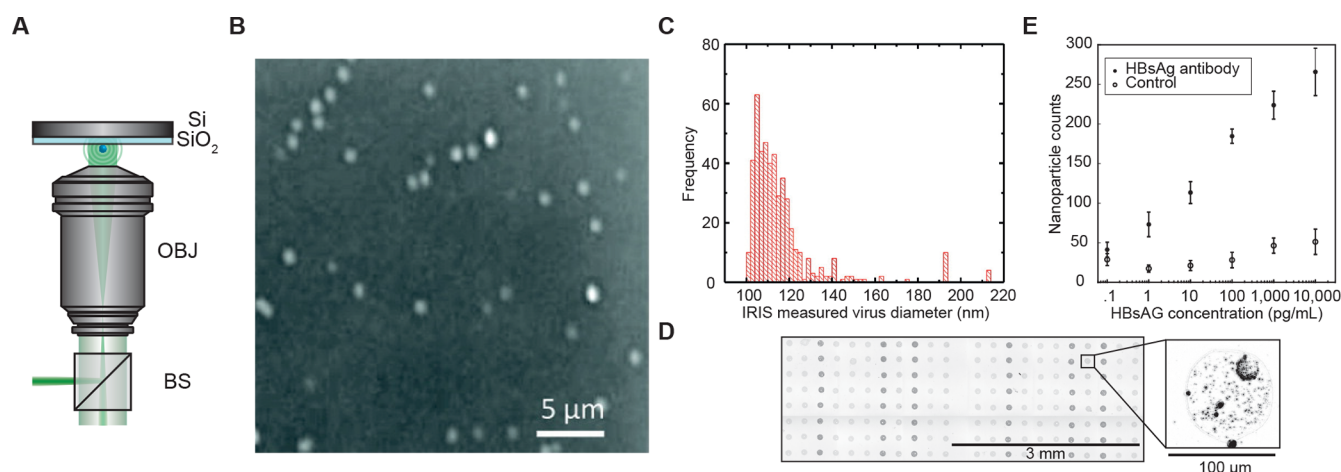


**Figure 12.** Single-particle interferometric reflectance imaging sensor (SP-IRIS). (A) Schematic illustrating the experimental configuration: OBJ, objective; BS, beamsplitter. (B) Image of H1N1 virus particles immobilized on an SP-IRIS chip. (C) Histogram of the measured H1N1 virus diameters. (D) Composite image of an SP-IRIS microarray. Inset: normalized image intensity image of  $25 \text{ nm} \times 71 \text{ nm}$  GNRs bound to the surface of a microarray spot. (E) Plot of GNR counts against the concentration of HBsAg. (B,C) Adapted with permission from ref 201. Copyright 2010 American Chemical Society. (D,E) Adapted with permission from ref 203. Copyright 2018 American Chemical Society.

interferometric reflectance imaging sensor (SP-IRIS),<sup>201</sup> which is the focus of this section.

In SP-IRIS, the  $\text{SiO}_2/\text{Si}$  substrate is imaged using a widefield reflection microscope containing a beamsplitter and a light-emitting diode (LED) illumination source (Figure 12A).<sup>201</sup> LED illumination provides a simple method to suppress coherent image artifacts, such as speckles. The reference field is generated from the light reflected by the IRIS substrate, hence the phase difference between the scattered and reflected field is optimized by tailoring the thickness of the  $\text{SiO}_2$  layer.<sup>202</sup> In addition, the IRIS substrate increases the collection efficiency of the scattered light from a nanoparticle when compared to that of a transparent substrate by reflecting some of the forward scattered light from the particle. In the original working mode of SP-IRIS developed by Ünü and co-workers, nanoparticles were immobilized on the substrate surface before being imaged with a high-NA air objective lens. Proof of principle experiments demonstrated the ability of SP-IRIS to detect and characterize the size of polystyrene beads immobilized on the substrate surface, ranging from 70 to 200 nm in diameter, and H1N1 influenza virus particles ranging from 90 to 160 nm in diameter (Figure 12B,C).

Building on this initial work, the application of SP-IRIS was extended to multiplexed detection of different viruses in complex media.<sup>204</sup> The IRIS chip was coated with a nonfouling copolymer functionalized with an array of multiple different monoclonal antibodies, which selectively bind to different virus surface glycoproteins. In this study, the SP-IRIS chips were incubated in the sample and were washed and dried before being imaged. The authors demonstrated that the technique was capable of detecting virus particles in both blood and fetal bovine serum (FBS). In addition, SP-IRIS was able to differentiate between multiple vesicular stomatitis virus (VSV) based virions in a mixed sample due to the size variations between different species. This capability was developed by Connor and co-workers, who used two LED illumination wavelengths to detect virus particles over a range of 40 to  $\sim 400$  nm in diameter.<sup>205</sup> A similar approach was used to detect exosomes by functionalizing the surface of the IRIS chip with a microarray of antibodies which selectively bind to exosomal biomarkers.<sup>206</sup> The technique was applied to detect exosomes

with diameters  $>50$  nm from purified samples and undiluted human cerebrospinal fluid.

SP-IRIS transitioned from operating in air to operating in buffer, enabling real-time measurements.<sup>207</sup> To overcome the reduced signal when operating in buffer, image processing techniques and a higher-NA air objective lens were introduced, along with optimization of the  $\text{SiO}_2$  thickness for these conditions. In this implementation, SP-IRIS demonstrated real-time detection of an Ebola model virus binding to an antibody-microarray coated IRIS chip in FBS with a detection limit of 100 PFU/mL. In the experiments presented, the temporal resolution of the technique was 30 s, which was adequate due to the low binding frequency of the viruses at the concentrations of interest. For measurement at higher concentrations, the temporal resolution could be improved through the use of a faster camera. This concept was extended by Scherr et al., who developed a disposable cartridge suitable for use with infectious samples, enabling SP-IRIS to act as a potential point-of-need diagnostic technique.<sup>208</sup> Moreover, the capture efficiency of virus particles in SP-IRIS was improved by incorporating advanced surface functionalization techniques and assay development, yielding a limit of detection down to 43 PFU/mL.<sup>209,210</sup>

SP-IRIS has undergone multiple recent technological developments. First, a number of strategies capable of analyzing stacks of defocused SP-IRIS images were developed, which improves the visibility of nanoparticles in SP-IRIS images.<sup>211–213</sup> Moreover, SP-IRIS adopted a similar approach to differential phase contrast<sup>214</sup> and Fourier ptychographic microscopy<sup>87,215</sup> by combining asymmetric illumination with computational reconstruction to improve the spatial resolution of the acquired images.<sup>216</sup> The technique was applied to imaging an Ebola model virus immobilized on an SP-IRIS chip surface in air with a spatial resolution of  $\sim 150$  nm, demonstrating a factor of 2 improvement over standard SP-IRIS.

In addition to the label-free imaging applications described above, SP-IRIS measurements have also included scattering labels. In a demonstration of this concept,  $\beta$ -lactoglobulin proteins were detected by combining SP-IRIS with antibody-functionalized 40 nm GNPs.<sup>217</sup> Antibody-functionalized SP-IRIS chips were incubated with media spiked with  $\beta$ -



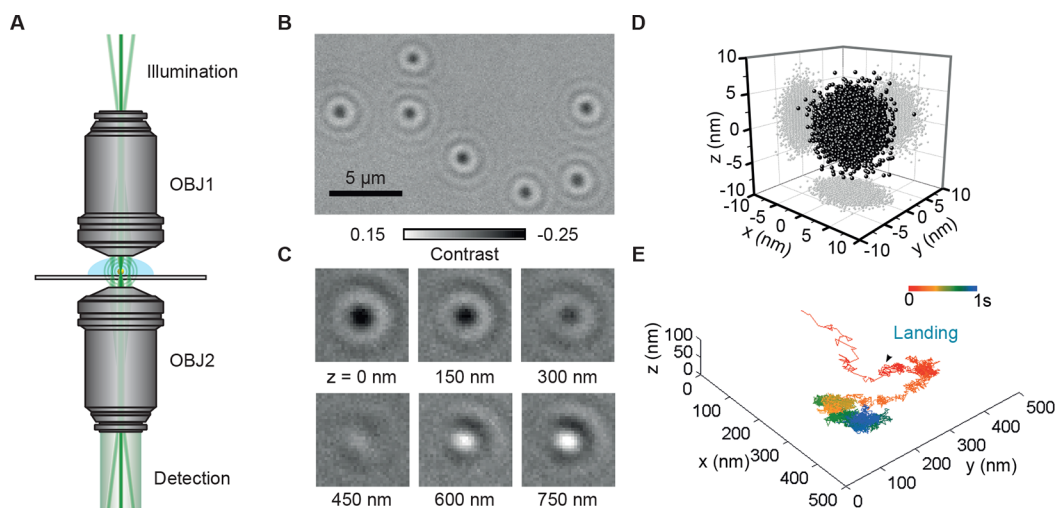


**Figure 13.** Coherent brightfield microscopy. (A) Schematic illustrating the experimental configuration. OBJ1, water-dipping objective; OBJ2, oil-immersion objective. (B) Image of vaccinia virus particles immobilized on a glass coverslip. (C) Image of a vaccinia virus particle as a function of axial sample position. (D) 3D localization of a tracked vaccinia virus particle immobilized on a glass coverslip at a frame rate of 5 kHz. (E) 3D trace of a virus particle landing and diffusing on a cell plasma membrane at an acquisition rate of 5 kHz. (B–E) Adapted with permission from ref 219. Copyright 2017 American Chemical Society.

lactoglobulin, enabling the protein to bind to the chip. Following this step, the chip was incubated with antibody-functionalized 40 nm GNPs, enabling the GNP labeled protein complex to be detected using SP-IRIS. The calculated limit of detection of the technique was  $\sim 60$  aM in undiluted serum and  $\sim 500$  aM in unprocessed blood. Furthermore, SP-IRIS used GNR labeling to detect and count viruses over a large FOV.<sup>203</sup> As GNRs scatter light which is linearly polarized along their longitudinal axis,<sup>37,76</sup> the authors used circularly polarized illumination in combination with polarization optics in the detection to selectively attenuate the reflected field relative to the scattered field. This enabled the detection of  $25 \text{ nm} \times 71 \text{ nm}$  GNRs while using a low-NA, low-magnification objective lens with a FOV of  $1.46 \text{ mm}^2$ , which enabled tens of GNR-containing microarray spots to be imaged simultaneously (Figure 12D). Because of the relationship between the orientation of the GNR and the retardation of the scattered field imposed by the polarization optics in the detection, a  $z$  stack of images was acquired and processed so that GNRs of all orientation angles were detected. This modality of SP-IRIS was used to detect hepatitis B surface antigen (HBsAg) in buffer, using  $15 \text{ nm} \times 40 \text{ nm}$  GNRs as scattering labels. Similar to the study outlined above, an antibody-microarray coated SP-IRIS chip was incubated with HBsAg, followed by incubation with antibody-functionalized GNRs. After these steps, the SP-IRIS chip was imaged in air to quantify the amount of GNR-labeled HBsAg bound to the antibody-microarray coated IRIS chip (Figure 12E). Combining single particle counting and inferring the number of nanorods within an unresolvable distance by analyzing the intensity of the signal, the sensor was capable of operating over a dynamic range of  $\sim 1 \times 10^6$ , with a limit of detection of  $3.2 \text{ pg/mL}$ . This work was extended to dynamic measurements by using a custom perfusion chamber and a higher-NA objective, sacrificing the size of the FOV in exchange for higher collection efficiency of scattered light.<sup>218</sup> In addition, an analysis scheme which tracked each binding event over time was developed so that the rate of binding and unbinding in a sample could be determined.

#### 4.6. Coherent Brightfield Imaging

In coherent brightfield imaging (COBRI), the interference takes place between forward scattered light from the object of interest and the transmitted illumination light. COBRI was introduced by Hsieh and co-workers, who showcased the method by label-free imaging and tracking of vaccinia virus particles ( $\sim 250 \text{ nm}$  in diameter) diffusing on a cell plasma membrane, at a frame rate of up to 100 kHz and a spatial precision of  $< 3 \text{ nm}$  (Figure 13B–E).<sup>219</sup> The authors demonstrated that the method is capable of three-dimensional tracking as the axial position of the object can be retrieved by analyzing the PSF due to the variation in the phase difference between scattered and transmitted light fields with the axial position of the scatterer. COBRI exhibits a single contrast inversion as the object of interest is translated through the focus, making axial tracking particularly intuitive and straightforward (Figure 13C). To track virus particles with high localization precision in the presence of scattering background from the cell membrane, the authors employed a digital background removal procedure. The experimental setup used a pair of AODs to scan a spatially filtered laser beam across the sample to generate an even illumination profile. The original experimental design of COBRI incorporated a 60 mm focal length lens to focus the illumination onto the sample, although this was later replaced by a water-dipping objective lens (Figure 13A).<sup>220</sup>

COBRI microscopy was further used to study intracellular cargo transport by imaging and tracking cellular vesicles in three dimensions inside live fibroblast cells at a frame rate of 30 kHz.<sup>221</sup> Because of the sensitivity limit of the particular setup used, vesicles below 150 nm in diameter could not be observed and hence the study focused on larger vesicles, with a mean diameter of  $\sim 320 \text{ nm}$ . Because of the high temporal resolution and long observation times enabled by the technique, transient bidirectional motion of the vesicles inside the cells were observed. In addition, correlated motion was observed by simultaneously tracking two adjacent vesicles. COBRI is particularly well-suited for tracking objects within cells, as the technique does not detect reflections from interfaces within the sample, such as a cell membrane.

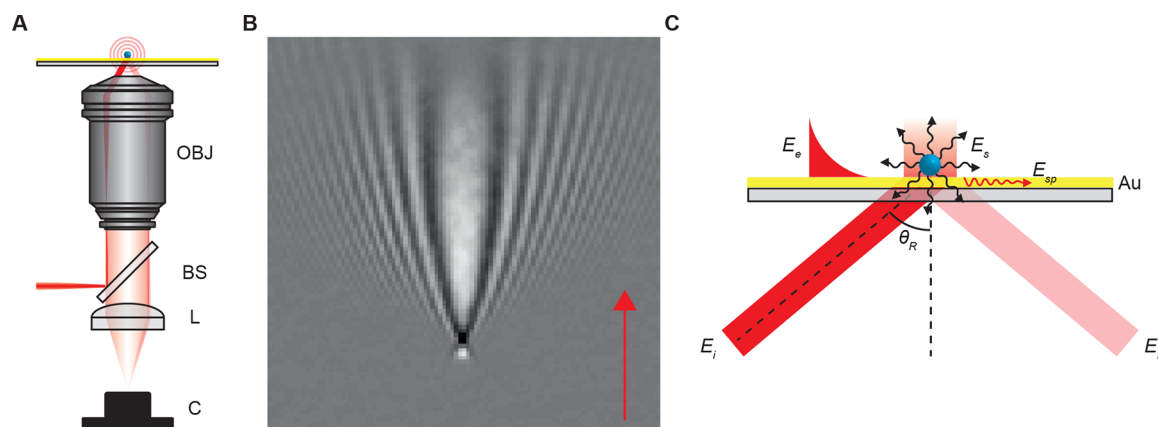


**Figure 14.** Surface plasmon resonance microscopy. (A) Schematic of a typical SPRM optical setup. OBJ, objective; BS, beamsplitter; L, tube lens; C, camera. (B) An example of a SPRM PSF with the arrow indicating the direction of surface plasmon propagation. (C) Near-field light–matter interaction of SPRM illumination.  $E_i$ , incident field,  $E_s$ , scattered field,  $E_r$ , reflected field,  $E_{sp}$ , evanescent field,  $\theta_R$ , resonant angle. (B) Adapted with permission from ref 259. Copyright 2018 American Chemical Society.

Recently, the sensitivity of COBRI was improved so that GNPs of diameters down to 10 nm could be imaged and tracked in water.<sup>220</sup> The gain in sensitivity was obtained by employing the reference field attenuation approach discussed in section 4.4.<sup>43–45</sup> As a proof of principle, a lipid labeled with a 10 nm GNP was tracked while diffusing on a supported lipid bilayer with an acquisition rate of 1 kHz and localization precision of 10 nm. In addition, the authors built a combined iSCAT-COBRI microscope to enable a quantitative comparison between the two techniques using the same detection line, image processing, and experimental parameters. To obtain a comparable level of camera counts with the same illumination intensity, the transmissivity of the partial reflector was tailored for each technique. It was determined that the sensitivity of the techniques are identical for equal illumination intensity, as expected from eq 7.

## 5. PLASMONIC IMAGING

### 5.1. Introduction

Many bioanalytical technologies leverage surface plasmon resonance (SPR) to amplify the evanescent electric field at the sample–substrate interface, thus enhancing the detected signal emanating from an analyte molecule in the far-field. SPR spectroscopy has been used in biosensing since 1983,<sup>222</sup> with the first biosensor based on the optical excitation of surface plasmons demonstrated in the early 1990s by Lundstrom et al. Modern SPR biosensors enable highly sensitive, often label-free investigation of the interaction between biomolecules, such as proteins<sup>223–230</sup> and nucleic acids,<sup>231–239</sup> with multiple reviews having documented the expansion of the field in great detail.<sup>240–246</sup> The majority of these approaches are ensemble-based, integrating the signal from multiple interactions in a macroscopic area so they fail to resolve the range of stochastic behavior present in a population of biomolecules. Recent developments have thus attempted to combine the information available from ensemble-based spectroscopic detection with high-resolution optical microscopy in an attempt to reach single-molecule sensitivity by SPR microscopy (SPRM).

Surface plasmon resonance refers to the collective oscillation of free conduction electrons near the interface of two media with dielectric constants of opposite signs, for example, a metal and a dielectric. The associated electromagnetic field is localized to

this interface and decays into both media. SPR spectroscopy measures changes in the optical reflectivity of the interface between these two media, which result from changes in the local refractive index caused by target species entering or leaving the evanescent field. The sensitivity of the measurement to small changes in the local refractive index is enhanced by the excitation of surface plasmon polaritons (SPP); charge density waves formed at, and propagating along, the interface between a metal and a dielectric medium. Excitation of SPPs on a continuous metallic film (typically silver or gold) with incident light requires matching the respective wave vectors. This can be achieved by tuning the angle of incidence of illumination. Consequently, as the illumination angle approaches the resonance angle, excitation of SPPs results in a sudden and sharp attenuation of the reflected light intensity. The resonance angle that leads to this intensity dip is therefore highly sensitive to the effective refractive index ( $n_{\text{eff}}$ ), the weighted average of the index of refraction of any materials within the evanescent field ( $\sim 300$  nm from the metal surface), such as liquids and absorbates.<sup>247</sup>

A typical SPR instrument excites surface plasmon modes on unstructured metal films by attenuated total reflection (ATR), passing a p-polarized monochromatic light beam through a prism, which is optically attached to a gold-coated glass slide. The reflected light intensity can then be quantified as a function of wavelength, at a fixed angle of illumination, or versus illumination angle for a range of wavelengths. The first demonstrations of spatially resolved plasmonic measurements were published in the 1980s by Yeatman and Ash<sup>248</sup> and Rothenhausler and Knoll.<sup>249</sup> Initial developments simply replaced the detector in an SPR spectroscopy setup, typically a photodiode, with a digital camera to obtain a two-dimensional image of the local refractive index change on the surface of a thin gold film. This technique is commonly known as SPR imaging (SPRI) or two-dimensional SPR (2D-SPR). Prism-based SPRI platforms provide sufficient spatial resolution to quantify the optical response of multiple cells independently<sup>250</sup> and, as a result, they provide a useful tool for several high-throughput and multiplexed analyses in biological research and drug discovery applications.<sup>251–255</sup> The spatial resolution achievable when a prism is used to collect the detected light, however, is limited. Replacing the prism with a high-NA objective lens greatly enhances the achievable spatial resolution to that of a wide-field microscope, thus facilitating SPRM.<sup>256</sup>

In this section, we will focus on recent developments in objective-based plasmonic imaging, particularly those which leverage SPR on continuous metallic films to enhance the signal and elevate plasmonic imaging toward single-molecule detection sensitivity.

## 5.2. Surface Plasmon Resonance Microscopy

A typical SPRM optical system focuses a beam of p-polarized monochromatic light into the BFP of a high-NA oil-immersion objective, producing plane-wave illumination of a gold-coated glass coverslip, again based on the ATR method, akin to the Kretschmann configuration.<sup>257</sup> Lateral offset of the focused beam away from the optical axis of the BFP,  $d$ , alters the incident illumination angle,  $\theta$ , while radial translation changes the azimuthal illumination angle and therefore the direction of SPP propagation. Given the focal length of the objective lens,  $f$ , the incident angle of illumination can be determined from eq 9:

$$d = f \sin \theta \quad (9)$$

Because of imperfect alignment and aberrations in the objective, however, a Fresnel-based optical model may not produce accurate results, thus a calibration measurement may be required. Modulation of the incident illumination angle determines the proportion of light reflected off of the gold–medium interface and collected by the objective before being imaged onto a CCD camera with a tube lens (Figure 14A). The reflected light intensity is strongly attenuated upon excitation of the surface plasmon. Wave vector matching of the incident light to that of the surface plasmon can be achieved by illuminating the metal/dielectric interface at the resonance angle or SPR angle,  $\theta_R$  given by<sup>258</sup>

$$\sin(\theta_R) = \sqrt{\frac{\epsilon_1 \epsilon_m}{(\epsilon_1 + \epsilon_m) \epsilon_2}} \quad (10)$$

where  $\epsilon_1$  and  $\epsilon_2$  are the dielectric constants of the dielectric medium (typically a buffer solution) and the objective lens, respectively, and  $\epsilon_m$  is the real part of the dielectric constant of the metal film. This equation is valid if the immersion medium and objective lens refractive index are matched. Small refractive index variations in the evanescent field at the interface alter the resonance angle. A practical implication of eqs 9 and 10 is the challenge associated with illuminating a sample at the resonance angle. For example,  $\theta_R = 71.6^\circ$  for a 50 nm thick gold film illuminated with  $\lambda = 638$  nm light at a water interface<sup>256</sup> and, as a result, objectives with  $NA > 1.4$  are required. In addition, as  $\theta_R$  for gold and silver films typically increases as  $\lambda$  decreases in the visible spectrum, illumination is generally restricted to red light in SPRM experiments, as higher index materials would be required to achieve  $\theta_i = \theta_R$  at shorter wavelengths.

For a uniform surface, measuring the change in reflected light intensity at a fixed incident angle of illumination enables the change in the effective refractive index of the interface to be determined. This is the basic principle of SPR spectroscopy. Resolving discrete local refractive index differences caused by the presence of a nano-object near the surface, however, requires a deviation from the classical model. This heterogeneity in the complex dielectric generates the contrast of an SPRM image. The incident p-polarized light at the substrate/metal interface is partially reflected and absorbed, exciting the surface plasmon wave and resulting in two fields: the reflected field,  $E_r$ , and the field associated with the surface plasmon,  $E_{sp}$ . The propagating surface plasmon wave is scattered by any dielectric discontinuity, such as an object near the metal surface, producing a scattered

field,  $E_s$  (Figure 14C). The light intensity detected at any given point in an SPR image,  $I_{SPR}$ , is given by a superposition of the reflected, scattered, and surface plasmon fields, radiated in the direction of reflection:<sup>260</sup>

$$\begin{aligned} I_{SPR} &= |E_r + E_{sp} + E_s|^2 \\ &= |E_{sp} + E_r|^2 + |E_s|^2 + 2\text{Re}\{E_s(E_{sp}^* + E_r^*)\} \end{aligned} \quad (11)$$

The first term in eq 11 describes a uniform SPR background in the absence of a particle. The second term in the expression is a pure scattering contribution, which is negligible for particles much smaller than the illumination wavelength. The complex third term describes the interferometric contribution between the scattering field and the surface plasmon, which can be expressed as an exponentially decaying cylindrical wave and gives rise to a parabolic “tail” pattern of fringes at the image plane (Figure 14B).<sup>261–263</sup>

Excitation of surface plasmon modes propagating across a continuous metallic surface produces an electric field exhibiting a characteristic propagation length ( $\sim 10^1 \mu\text{m}$ ) and penetration depth ( $\sim 10^2$  nm). While this is the most commonly excited surface plasmon mode in SPRM experiments, these properties can be manipulated using conductive-dielectric multilayers,<sup>264</sup> exciting localized surface plasmons (LSP) supported by a single nanoparticle,<sup>265–268</sup> or by manufacturing arrays of plasmonic nanoparticles<sup>269,270</sup> or nanoapertures<sup>271–273</sup> on a metallic film. There have been many optical platform developments in the field of spectral SPR imaging and biosensing, with nonresonant detection sensitivities reaching the single molecule level in two independent studies in 2012. Zijlstra et al. employed a sensitive photothermal assay to monitor the SPR of a gold nanorod upon binding of single proteins, producing results which exhibited a 700-fold increase in sensitivity over alternative, state-of-the-art plasmon biosensors at the time.<sup>267</sup> In a different approach, Ament et al. illuminated a gold nanorod with a white light laser in TIR and employed a darkfield spectroscopy detection modality; this allowed them to resolve the discrete steps in the SPR wavelength caused by single protein binding events on the millisecond time scale.<sup>268</sup> These pioneering developments, as well as many other studies which leverage plasmon sensor technologies, have been covered in other reviews.<sup>241,274–276</sup> For this review, we will focus on recent developments in objective-based SPRM setups based on the excitation of propagating SPPs on continuous metallic films.

The PSF of an SPRM microscope is distorted by the propagating SPP, and thus its orientation is ultimately dictated by the incident (polar) angle of illumination (Figure 14B). Spatial resolution is diffraction limited in the direction transverse to SPP propagation, while extending over the propagation length of the SPP in the longitudinal direction, typically several micrometers. Tao and co-workers were the first to observe this pattern,<sup>277</sup> and subsequently proposed a theoretical model to describe the interaction between a propagating SPP and an isolated nano-object.<sup>260</sup> Several theoretical models have also attempted to describe this interaction and its role in the formation of a plasmonic image.<sup>278</sup> Quantitative analysis of the wave-like PSF, however, has been challenging due to its geometric complexity despite these complex interferometric scattering patterns containing information regarding the properties of the associated nanoparticle. The summed signal intensity over a region of interest (ROI) selected from a PSF can be used to identify both the size of a nanoparticle and its distance from the metal film. The



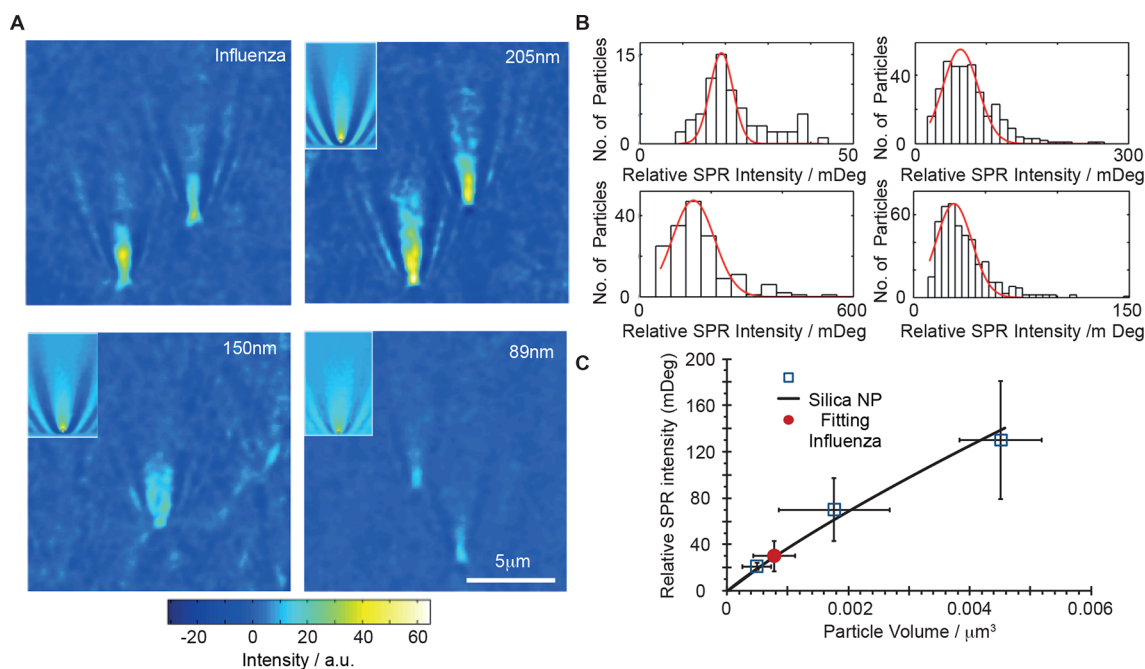


**Figure 15.** SPRM detection of single virus particles. (A) SPRM images of H1N1 influenza A virus and three different-sized silica nanoparticles in PBS buffer. (B) Histograms of SPR intensities of silica nanoparticles of different diameters and of influenza A viral particles. (C) Calibration curve of SPR intensity vs particle volume. (A–C) Adapted with permission from ref 277. Copyright 2010 National Academy of Sciences.

refractive index, and therefore the nanoparticle material, however, cannot be accurately determined by this method. Quantitative interpretations in the frequency domain have further developed the general understanding and analysis of the SPRM PSF.<sup>259</sup> The interferometric pattern partly consists of light scattered from the imaged nanoparticle, hence it must depend on parameters such as the refractive index as well as the size of the nanoparticle. Quantitative analysis of this pattern was achieved, both numerically and experimentally, by implementing a parameter,  $\psi$ , which describes the phase of the parabolic patterns leading to the elucidation of the relationship between the refractive index of the nanoparticle and its associated pattern.<sup>279</sup>

The detection of scattered light of a propagating evanescent wave limits the spatial resolution of SPRM. However, the confinement of the surface plasmon to the metal/dielectric interface provides SPRM with extremely high axial sensitivity. The rapidly decaying evanescent field results in an exponential relationship between SPR signal intensity and the axial distance between a particle and the interface. If the decay constant of the SPRM system is known, this relationship can be quantified with a precision of  $\sim 5$  nm in the  $z$ -direction.<sup>280</sup>

### 5.3. Biomolecular Imaging and Detection

Despite its anisotropic PSF, SPRM has been employed to directly image and study both synthetic nanoparticles and biomolecules. The excitation of a propagating SPP amplifies the local electric field and is scattered by any dielectric discontinuity in its path while also attenuating the amount of light reflected from the surface. Both of these effects contribute toward enhanced interferometric contrast in the far field. Furthermore, the confinement of the evanescent field to within approximately 200–300 nm of the gold–medium interface rejects background scattering from out-of-focus particles, much like in the approaches discussed in section 3. Tao and co-workers leveraged this effect to image single H1N1 influenza A virus particles and

monitor their interaction on different surfaces (Figure 15A).<sup>277</sup> The multiplexing capabilities of SPRM enabled high-throughput analysis of several individual virus particles. By fitting the SPRM signal from differently sized silica nanoparticles (Figure 15B), a proportional relationship was verified between the volume of the particles and the interferometric signal (Figure 15C). By way of this calibration process, and by approximating the refractive index of viral particles as  $\sim 1.48$  due to their protein–lipid composition, the volume and diameter of influenza A was found to be  $6.8 \pm 3.0 \times 10^{-4} \mu\text{m}^3$  and  $109 \pm 13$  nm, respectively, in good agreement with literature values.

The imaging capability enabled by a high-NA objective provides SPRM with single-molecule sensitivity, first demonstrated by Yu et al. in 2014.<sup>281</sup> By implementing differential imaging coupled with lateral translation of the image and a deconvolution algorithm, single DNA molecules were imaged. These images were used to measure the length of individual stretched  $\lambda$ -DNA molecules to determine an average length of  $\sim 14.6 \mu\text{m}$ , in good agreement with fluorescence images and theoretical models. Applications of SPRM to study larger biological structures, such as single-bacterium motion classification<sup>282</sup> and visualization of cellular activity and morphology,<sup>283–285</sup> further demonstrate the versatility of the technique, but such applications are mostly beyond the scope of this review.<sup>286</sup> It is worth noting that the extension of the electric field penetration depth toward cellular length-scales ( $\sim 1 \mu\text{m}$ ) can be achieved by depositing a buffer layer with a refractive index similar to that of the sample between the substrate and the metal film.<sup>264</sup> This technique, called long-range surface plasmon resonance (LRSRP), has recently been incorporated into an SPRM setup to study cellular micromotion.<sup>285</sup>

The sensitivity of a SPRM measurement is determined by its ability to detect small variations in the refractive index, which are proportional to the volume of the analyte molecule. Consequently, quantitative detection of small-molecule binding events is a challenge for a conventional SPRM system. In an

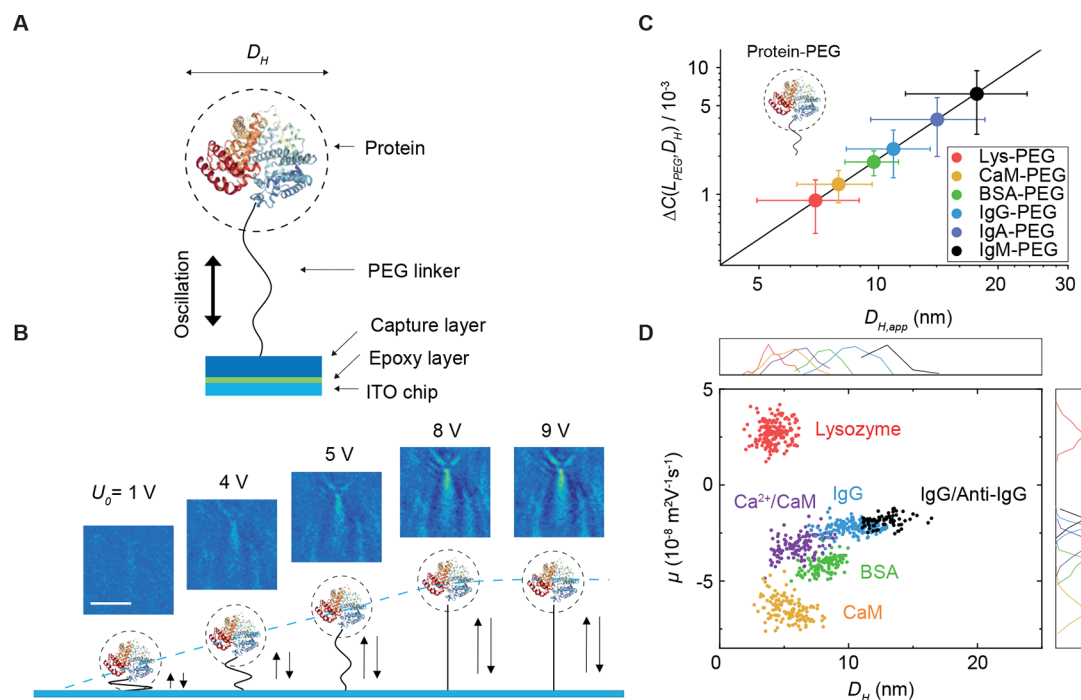


**Figure 16.** SPRM imaging of protein size, charge, and mobility. (A) Schematic showing a single protein tethered to an ITO surface by a 63 nm long polyethylene glycol (PEG) linker. (B) FFT image contrast as a function of potential amplitude and a schematic displaying this relation to PEG tether extension; scale bar = 3  $\mu\text{m}$ . The blue dashed line indicates linear and plateau regimes of tether extension. (C) Size determination of protein-PEG complexes ( $D_H$ ) as a function of FFT image contrast change ( $\Delta C$ ). (D) 2D plot of mobility ( $\mu$ ) vs size ( $D_H$ ) of single proteins and protein-ligand complexes. (A–D) Adapted with permission from ref 295. Copyright 2020 Springer Nature under Creative Commons Attribution 4.0 International License <https://creativecommons.org/licenses/by/4.0>.

alternative approach, plasmonic-based electrochemical impedance microscopy (P-EIM) employs an SPRM optical setup to image the electrochemical impedance distribution across the surface while simultaneously measuring the SPR response.<sup>287</sup> Instead of measuring changes in current directly, P-EIM uses the gold surface as an electrode and converts local surface charge variations, which result from the modulation of an applied external field, into an optical signal. In comparison to SPRM, P-EIM yields improved image contrast and greater sensitivity when detecting small molecules. P-EIM measures interfacial impedance rather than refractive index changes, therefore the measured signal does not scale with the mass of the analyte molecule. The superior sensitivity, coupled with submicrometer spatial resolution and submillisecond temporal resolution, makes P-EIM a powerful approach for small-molecule detection and quantitative investigation of protein binding kinetics, as well as a variety of other applications.<sup>288–290</sup>

The labeling of biomolecules with GNPs can also enhance the detected optical response, as has been shown in multiple SPR biosensor studies. Used in conjunction with SPRM, Halpern et al. demonstrated real-time detection of hybridization adsorption of single DNA-functionalized GNPs.<sup>291</sup> A novel method to improve the detection capabilities of SPRM toward small-molecule detection combines the axial sensitivity of SPRM with the signal amplification provided by GNPs and the detection sensitivity of P-EIM. Here, GNPs are bound to a gold electrode with a molecular tether and an oscillating electric field is applied normal to the electrode surface, causing the GNPs to oscillate in the  $z$  direction. The plasmonic signal from the nano-oscillators is extremely sensitive to the amplitude of their oscillation, such that the  $z$  position of each nano-oscillator can be determined with a precision of  $\sim 0.1$  nm.<sup>292</sup> From the measured amplitude

and phase of the oscillation, the charge of each nano-oscillator can be determined with a detection limit of  $\sim 0.18$  electron charges in aqueous solution. This sensitivity to nano-oscillator charge, which is altered by the binding of small molecules, was further employed to monitor phosphorylation kinetics.<sup>293</sup> An adaptation of this approach used light to drive the nano-oscillators rather than an external electrical current.<sup>294</sup> Mechanoresponsive polymers self-assemble on the gold surface and act as both a tether and a motor for the GNPs, as they extend and collapse under periodic photothermal generation. To monitor single-strand microRNA (miRNA), the complementary strand is immobilized in the gap between the GNP and the gold surface, and as the two hybridize to form a rigid double-stranded structure, the oscillation amplitude of the GNP is damped. Using the time trace of the damping signal, real-time monitoring of single-molecule miRNA hybridization can be achieved.

Unlike traditional localized SPR (LSPR) methods, the implementation of nano-oscillators as signal-enhancing devices is not limited to metallic nanoparticles. A recent study has applied the general principles of nano-oscillator SPRM but replaced the GNP antenna with single proteins and the plasmonic surface with a layer of indium tin oxide (ITO) (Figure 16A).<sup>295</sup> An alternating electric field is applied to the ITO surface, driving the oscillation of the tethered protein molecules. With an SPRM optical setup, the surface is illuminated at an oblique angle which produces an evanescent wave, the incident light is scattered by the protein and collected by a high-NA objective, and an image sequence is recorded on a CMOS camera. A fast Fourier transform (FFT) is performed on the image sequence to isolate the oscillation frequency of the applied field and extract the oscillation amplitude while rejecting

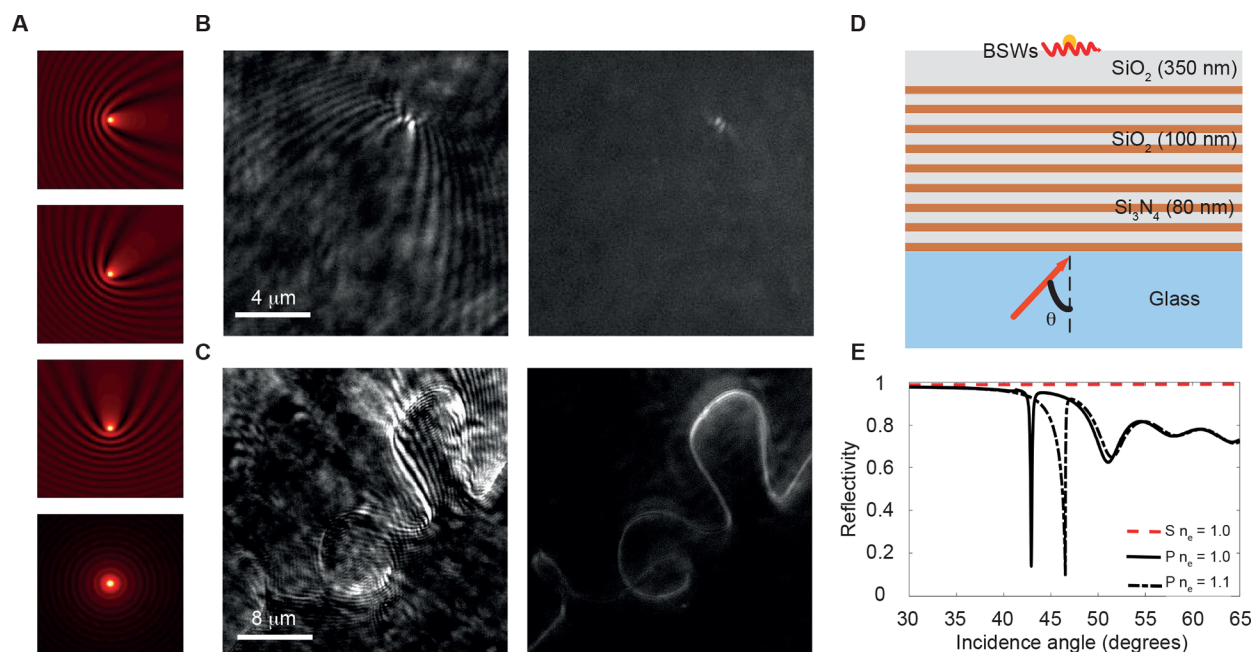


**Figure 17.** SPRM-ARI imaging and Bloch surface wave microscopy. (A) Schematic illustrating the superposition of the planar illumination wave, incident at differing azimuthal angles, and a circular scattered wave from a nanosphere. The bottom image shows the cumulative propagation direction of the planar wave for azimuthal illumination angles 0–360°, similar to SPRM-ARI. (B) SPRM image of a 50 nm nanosphere on a Ag film (left) and a corresponding image acquired with SPRM-ARI (right). (C) Images acquired analogously to those in B but of a winding polymer nanowire. (D) Schematic displaying the dielectric multilayer substrate used for BSWM. (E) Angle-dependent excitation spectrum where  $n_e$  is the refractive index of the environment. (A–E) Adapted with permission from ref 299. Copyright 2019 American Association for the Advancement of Science under Creative Commons Attribution-NonCommercial 4.0 International license <https://creativecommons.org/licenses/by-nc/4.0/>.

background noise (Figure 16B). The resulting signal has been used to estimate the size (Figure 16C), charge, mobility, and conformation of the tethered protein. This data was then used to produce a two-dimensional plot of mobility vs size for various single proteins and protein–ligand complexes (Figure 16D).

#### 5.4. Resolution-enhanced Surface Plasmon Resonance Microscopy

Although imaging of single molecules is possible with conventional SPRM, the complex, wave-like PSF significantly restricts spatial resolution and sensitivity. Attempts have been made to reconstruct a pseudospherical scattering wavefront and thus a symmetric PSF, both optically and computationally.

One approach to improve the spatial resolution is to use light with a shorter wavelength (e.g.,  $\lambda = 532$  nm for Au) to excite the surface plasmons, although this sacrifices sensitivity as the SPR is less well-defined.<sup>256</sup> Lateral raster scanning of a focused probe beam across the surface, in a technique known as scanning localized surface plasmon microscopy (SLSPM), has also been shown to achieve improvements to the spatial resolution but at the expense of temporal resolution.<sup>296–298</sup> The wave-like appearance of the SPRM PSF is not entirely unique to SPRM. As discussed in section 3.3, illumination of a nano-object by a plane wave incident at an oblique polar angle produces a similarly anisotropic PSF, with tail-like fringe patterns, as the spherical scattered wave and reflected plane wave have a spatially inhomogeneous phase offset.

Using conventional brightfield microscopy, as discussed in section 3.3, Rohrbach and co-workers overcame these fringe patterns by incoherently averaging images recorded with many different azimuthal angles of illumination.<sup>85,91</sup> A similar azimuthal rotation illumination (ARI) approach was implemented in an SPRM microscope (SPRM-ARI) (Figure 17A),<sup>299</sup>

building upon previous attempts to optically improve the lateral resolution in SPRM.<sup>300–302</sup> The characteristic tails produced from SP scattering of a nanoparticle on a silver film were effectively homogenized upon image averaging, resulting in a bright, doughnut-shaped PSF (Figure 17B). This shape can be explained by the polarization-matched coupled emission at all incident azimuthal angles of illumination, analogous to the PSF for surface plasmon-coupled emission microscopy (SPCEM).<sup>303–305</sup> A polarizer was inserted in front of the camera, such that this doughnut-shaped spot was separated into two bright spots, which can be regarded as the PSF of SPRM-ARI. The benefits of improved spatial resolution and smoothing of interferometric fringe patterns was further illustrated by imaging the complex shape of a winding nanowire (Figure 17C). SPRM-ARI is said to enhance the longitudinal spatial resolution of SPRM by an order of magnitude, and the effective temporal resolution is only limited by the illumination rotation speed (1 ms), as opposed to the lateral movement time limitation in differential SPR. Alternative nonmetallic films for signal enhancement have also been suggested and compared. Using bespoke dielectric multilayers to produce Bloch surface waves (BSW) instead of surface plasmons, illumination wavelength, resonant angle, and polarization state can be tailored (Figure 17D). While SPRM is restricted to illumination with P-polarized light, commonly in the spectral region of 635 nm for Au films due to resonant angle collection, BSW microscopy (BSWM) can operate with S-polarized light of shorter wavelengths (e.g., 532 nm) and with tunable penetration depths (Figure 17E).

A recent study by the Tao group has modified the traditional SPRM method to image the scattering of SPPs in a transmission modality, which they refer to as plasmonic scattering microscopy (PSM).<sup>306</sup> In contrast to reflection-based SPRM, the reflected light is not collected, and plasmonic images are produced by the



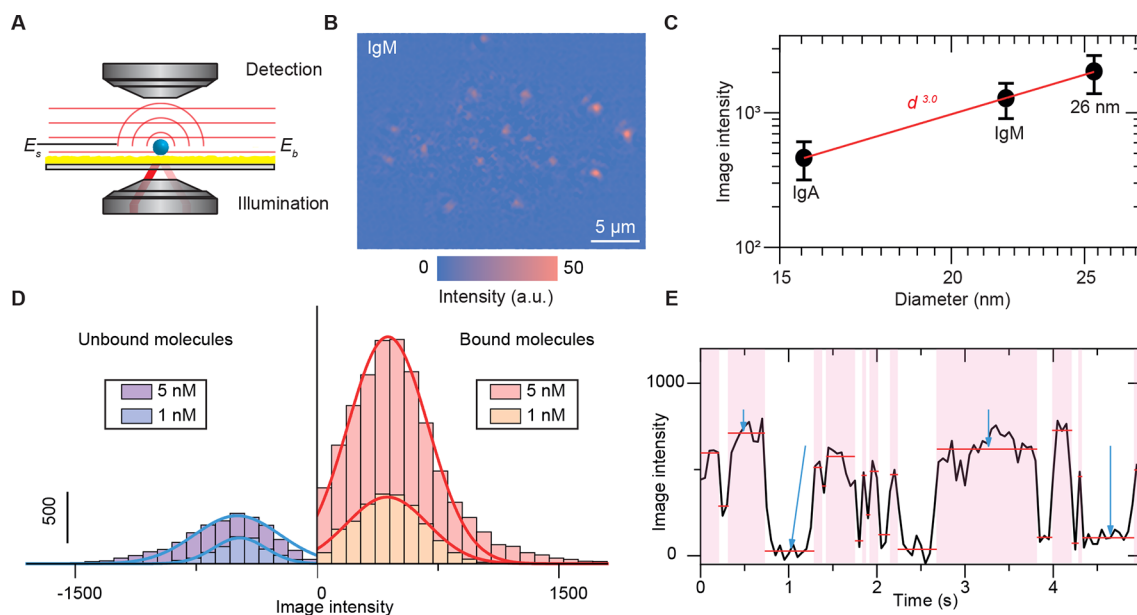


**Figure 18.** Quantitative detection of single molecules by plasmonic scattering microscopy. (A) Schematic illustrating the detection method employed in PSM, in which plasmonic waves scattered by a particle ( $E_s$ ) and any inhomogeneities on the gold surface ( $E_b$ ) are gathered from the top and interfere to produce an image at the detector. (B) Background and drift corrected PSM image of immunoglobulin M (IgM) molecules. Scale bar: 5  $\mu\text{m}$ . (C) PSM image intensity vs particle diameter. (D) Histograms displaying intensity changes associated with binding and unbinding of individual IgA molecules. (E) Example of the binding behavior of a single IgA molecule. (B–E) Adapted with permission from ref 306. Copyright 2020 Springer Nature.

interferometric interaction of light scattered from both the particle and from topographical inhomogeneities of the gold surface (Figure 18A). This allows for higher illumination intensities ( $\sim 30\,000\times$ ), provides a high-contrast image and circumvents the complexity and limited resolution of the SPRM PSF. Instead, the pixel intensities are integrated across the complex Airy disk (Figure 18B). The enhanced sensitivity of PSM was demonstrated by label-free imaging of single proteins. Human immunoglobulin M (IgM) and human immunoglobulin A (IgA) were detected upon binding to the surface (Figure 18B), and their respective sizes were determined (Figure 18C). This identification was further confirmed by distinguishing both proteins via the specific binding of IgA to an anti-IgA coated surface. The latter experiment enabled the quantification of single-protein binding kinetics by digital counting of individual binding events of IgA molecules to an anti-IgA coated surface (Figure 18D,E). Surface coverage results, obtained by multiplying the binding counts detected by PSM by the molecular mass of IgA (385 kDa), were consistent with ensemble SPR measurements, confirming that PSM can be used to measure protein mass. The PSM optical setup was recently modified to include a Kretschmann prism-coupled SPR illumination configuration, while retaining single protein sensitivity and high spatial resolution enabled by transmission detection.<sup>307</sup>

Computational approaches to reconstruct an isotropic SPRM PSF, without additional temporal limitations or further complication of the optical setup, have also been explored.<sup>308</sup> The image reconstruction algorithm proposed applies filters in Fourier space to obtain the scattered field from the measured image, before reconstructing the object image via deconvolution of the scattered field with the SPRM PSF, modeled by a decaying cylindrical wave. This process was demonstrated on 100 nm polystyrene nanoparticles and achieved near-diffraction-limited spatial resolution in both transverse and longitudinal directions of  $\sim 310$  nm. However, in the presence of multiple non-

negligible scattering events, a more sophisticated algorithm may need to be applied. In another study, this digital image-processing algorithm was employed in an optimized SPRM setup termed interferometric plasmonic microscopy (iPM).<sup>309</sup> Diffraction-limited spatial resolution ( $\sim 260$  nm) enabled the real-time imaging of single exosomes adsorbing to a modified Au surface, which was then used to determine their respective diameters (30–150 nm). This level of sensitivity resulted quantitative measurements of the membrane fusion activity between exosomes and liposomes, as well as the study of the dynamic interaction between exosomes and antibodies.

## 6. SUMMARY AND OUTLOOK

In this review, we have given an overview of recent developments in darkfield, interferometric scattering, and plasmonic microscopy in the context of nanoparticle and molecular imaging, detection, and characterization. These three approaches have achieved significant increases in sensitivity, with the latter two reaching the single (bio)molecule level under ambient conditions. Darkfield microscopy has demonstrated the most limited sensitivity of the discussed techniques, mainly due to the  $D^6$  scaling of signal with particle size, which necessitates extremely efficient background rejection and extensive dynamic range to detect very small signals. Even in the absence of demonstrating single-molecule sensitivity, darkfield microscopy has been used to detect single viruses<sup>71,112</sup> and 10 nm GNPs<sup>42</sup> in studies on custom-built microscopes.

Despite the limited sensitivity of darkfield microscopy relative to interferometric scattering and plasmonic enhancement, efficient background rejection enables much higher illumination intensities for a given detector, allowing a significant portion of the full well depth of the camera to be used for detecting scattered photons. The combination of strong background rejection with a theoretically unlimited photon budget enables darkfield microscopy to perform well as a single-particle tracking

technique when imaging suitably sized labels due to the high resulting signal-to-background ratios. Examples include shot-noise-limited localization precision of  $\sim 1$  nm with 10  $\mu$ s temporal resolution when tracking 20 nm GNPs in a micromirror TIRS setup<sup>58</sup> and 1.3 Å localization precision with 1 ms temporal resolution when tracking 40 nm GNPs using a perforated mirror TIRS setup with annular illumination.<sup>72</sup>

A potential downside of the single-particle tracking ability of darkfield microscopy is the difficulty of applying the technique to biological environments that exhibit high levels of background scattering. To overcome this limitation, strategies may include improved image processing techniques and the introduction of next-generation detectors with higher full-well capacities. We anticipate darkfield microscopy usage to continue to focus on single-particle tracking of biologically relevant systems using scattering labels, and expect that further technological developments will continue to push the boundaries of spatiotemporal resolution, enabling the analysis of even faster and more subtle molecular motion. Beyond this application, for darkfield microscopy to reach the sensitivity limits achieved by interferometric imaging, developments in image processing might be required to identify the target signal from any unwanted background. This may be a nontrivial task, however, as background scattering from sources near the target particle, such as coverslip surface roughness, may interfere with the scattered light from the particle, producing a complex signal. Thus, the ultimate challenge for darkfield microscopy, when attempting to observe very small scatterers such as single molecules, is to retain a purely scattering intensity measurement in the absence of any background, or to develop novel image analysis approaches, which allows the interferometric interaction of the signal and background to be used.

Interferometric scattering microscopy has exhibited sensitivity superior to that of darkfield microscopy, largely due to the weaker  $D^3$  scaling of the signal with particle size and resulting higher ease of background suppression. The boundaries have been significantly pushed, from the detection of metal nanoparticles to single proteins, through the introduction of innovative image processing, and data analysis techniques combined with various technological developments.<sup>32–34,43</sup> Significantly improving the sensitivity of interferometric microscopy in its current form may prove a difficult task, as there are limits to the incident laser power that biological samples and optical elements can be exposed to. Strategies to collect more light by integrating for longer in time, at the expense of temporal resolution, would require an improved approach to background noise subtraction, especially in the context of lateral drift and other cumulative noise sources. This could be achieved by developments in both the hardware, such as substrate modifications, or the image analysis methods. Additionally, exploring mechanisms which enable an increase in the light–matter interaction strength at the sample might be worthwhile.

The ability to detect and quantify the mass of single proteins in solution under ambient conditions is an exciting development, with broad use across the life sciences. We anticipate the detection limit of MP to be further improved through a range of hardware and software developments, enabling the study of currently inaccessible systems and more complex biomolecular processes. iSCAT, one of the most rapidly developing interferometric scattering approaches, has transitioned from single-particle tracking in low scattering environments to 3D tracking in complex environments, including cell mem-

branes.<sup>136–138,140</sup> This represents an important advance, as tracking biomolecules within their native environments at spatiotemporal resolutions inaccessible in fluorescence microscopy paves the way to discover hitherto hidden dynamics. We hypothesize that interferometric scattering microscopy development will continue to focus on unlocking the information contained within its complex PSF, while improvements in sensitivity and image processing will enable the use of smaller scattering labels and imaging at higher spatiotemporal resolutions. In addition to pushing the boundaries of sensitivity, we expect interferometric scattering microscopy techniques to achieve some degree of specificity, for example, through the development of improved biosensor assays and technology, yielding ever-lower limits of detection.<sup>201,203,210</sup>

Similar to darkfield microscopy, interferometric scattering microscopy is well-suited to being combined with other microscopy techniques due to the simplicity of the optical setup and the universality of light scattering. In this review, we have discussed the incorporation of iSCAT detection in optical traps,<sup>139,145–149</sup> however, this is just one of many techniques with which iSCAT is compatible. Therefore, we anticipate more correlative combinations to be explored, including combinations involving scanning probe and light microscopy techniques.

Further applications of iSCAT, some of which stretch beyond the scope of this review, focus on nanoscale imaging. Most recently, the concept of iSCAT's general sensitivity to changes to local polarizability has been extended beyond the strict life sciences context. One example is the introduction of time-resolved iSCAT, termed stroboSCAT, where iSCAT is performed in a pump–probe configuration to monitor ultrafast dynamics in 2D materials following photoexcitation.<sup>310,311</sup> iSCAT has also recently been used to monitor phase transitions during nanoparticle charging in batteries at the single-particle level, enabling detailed investigations of the process.<sup>312</sup> In addition, another recent development is the combination of iSCAT detection principles with mid-infrared photothermal (MIP) microscopy. This emerging technique is particularly exciting due to the chemical specificity obtained during the measurement. In visible probe MIP microscopy, the mid-IR absorption induced photothermal effect is probed using visible light.<sup>313–315</sup> The technique has recently been applied to chemically specific imaging of cells,<sup>316</sup> 100 nm polystyrene beads,<sup>317</sup> and single virus particles.<sup>318</sup>

Significant advances have been made in surface plasmon resonance microscopy, the part of the plasmonic imaging field covered in this review. Developments in both the experimental methods and image analysis have enabled its application to the study of many biological molecules and systems, including viruses, DNA molecules, and single proteins, as well as larger complexes such as bacteria and live mammalian cells. Despite the near-field enhancement provided by the surface plasmon coupling of the incident light, the major limitation of SPRM is its complex, elongated PSF, which renders image contrast comparisons to nonplasmonically enhanced interferometric approaches difficult to elucidate. The lateral resolution, in the direction of surface plasmon propagation, is limited by the characteristic parabolic PSF tail, which extends for several micrometers beyond the diffraction limit of the transverse direction. Recent attempts to tackle this issue have shown promising results. Altering the optical system to generate images from multiple illumination directions has proven to be an effective approach,<sup>299</sup> although it limits the temporal resolution (which is restricted to the beam-scanning rate) as well as the PSF


(which remains suboptimal due to polarization effects and anisotropic emission). Novel image processing methods have aided the analysis of the SPRM PSF and also enabled the reconstruction of a symmetrical, diffraction limited PSF.<sup>308,309</sup> The initial promise of these resolution-enhanced SPRM techniques bodes well for future iterations, which minimize any limitations associated with temporal resolution and image contrast.

Ever-expanding developments of the plasmonically active substrate, including the addition of bespoke nanostructures and nanoapertures, are enabling further near-field enhancement, as well as other experimental advantages, such as alternative optical options and specific surface functionalization. Bloch surface wave microscopy enables many of these advantages by replacing the metallic film with a dielectric multilayer, which may help to alleviate any negative effects associated with the heating of the metallic film. Specific parameters of this multilayer structure can be modified to suit a range of illumination wavelengths and the use of s-polarized light, while the SiO<sub>2</sub> top layer resembles that of a typical microscope coverslip.<sup>299</sup> Finally, the incorporation of surface-charge-sensitive measurements has shown great promise for improving SPRM sensitivity toward the detection of small molecules.<sup>289</sup> We anticipate many more promising technical developments and novel applications introduced to the expanding field of plasmonic imaging in the coming years.

It is worth emphasizing the degree to which nominally very different methods share very similar challenges. Traditionally, darkfield, interferometric, and plasmonic microscopy have been largely separate fields. Given the advances in these fields, the next step changes likely require the combination of concepts and approaches from all three, together with stronger efforts in terms of optics, detectors, and data analysis geared toward label-free optical images. Concerted efforts have enabled revolutions in fluorescence and electron microscopy; they are now required to fulfill the promise that scattering-based methods have demonstrated over the past few decades.


## AUTHOR INFORMATION

### Corresponding Author

**Philipp Kukura** – *Physical and Theoretical Chemistry Laboratory, Department of Chemistry, University of Oxford, Oxford OX1 3QZ, United Kingdom*;  [orcid.org/0000-0003-0136-7704](https://orcid.org/0000-0003-0136-7704); Phone: +44 1865 275401; Email: [philipp.kukura@chem.ox.ac.uk](mailto:philipp.kukura@chem.ox.ac.uk); Fax: +44 1865 275410

### Authors

**Lee Priest** – *Physical and Theoretical Chemistry Laboratory, Department of Chemistry, University of Oxford, Oxford OX1 3QZ, United Kingdom*;  [orcid.org/0000-0001-5906-3493](https://orcid.org/0000-0001-5906-3493)

**Jack S. Peters** – *Physical and Theoretical Chemistry Laboratory, Department of Chemistry, University of Oxford, Oxford OX1 3QZ, United Kingdom*;  [orcid.org/0000-0001-8829-7555](https://orcid.org/0000-0001-8829-7555)

Complete contact information is available at:  
<https://pubs.acs.org/10.1021/acs.chemrev.1c00271>

### Author Contributions

†L.P. and J.S.P. contributed equally.

### Notes

The authors declare no competing financial interest.

## Biographies

Lee Priest studied Natural Sciences at University College London and received his MSci degree in 2016. He is currently a Ph.D. student in the Kukura Group at the University of Oxford. His research has focused on advancing the sensitivity of interferometric imaging techniques, primarily in the context of mass photometry particle detection.

Jack S. Peters studied at the University of Warwick and received his MChem degree in 2018. He is currently a graduate student under the supervision of Professor Philipp Kukura at the University of Oxford. His current research focuses on technological development of mass photometry, with the aim of improving the sensitivity and mass resolution of the technique.

Philipp Kukura is Professor of Chemistry and Fellow of Exeter College at the University of Oxford. He received an MChem from the University of Oxford (2002) and a Ph.D. from the University of California, Berkeley (2006). After postdoctoral work at ETH Zurich, he joined the Chemistry Department at the University of Oxford as Research Fellow (2010), Lecturer (2011), and then full Professor (2016). Honours and awards include the Royal Society of Chemistry Harrison Meldola Award (2011), the Royal Society of Chemistry Marlow Award (2015), the EBSA Young Investigator Award (2017), the Royal Society Wolfson Research Merit Award (2018), the Klung-Wilhelmy Science award in Chemistry (2018), the Blavatnik Award for Young Scientists UK in Chemistry (2019), and the RMS Medal for Light Microscopy (2021). His current research interests include the application of ultrasensitive light microscopy to study bimolecular structure and interactions.

## ACKNOWLEDGMENTS

P. K. is supported by an ERC Consolidator grant (PHOTO-MASS 819593) and an EPSRC Leadership Fellowship (EP/T03419X/1). L.P. is supported by the Christ Church Moritz-Heyman Award and the EPSRC Doctoral Training Partnership. J.S.P. is supported by the EPSRC Doctoral Training Partnership. We thank Catherine Lichten and other members of the Kukura Group who provided highly valued feedback and input to this article. The field of optical microscopy, and its application to nanoscale phenomena has seen tremendous activity over the past decades, and while we have made our best effort in being comprehensive, it is likely unavoidable that we may have missed important and relevant contributions, for which we would like to apologize. We very much acknowledge all those who contribute to this incredibly exciting and rapidly progressing field.

## ABBREVIATIONS

AOD = acousto-optic deflector

Apols = amphipols

ABEL = anti-Brownian electrokinetic

ATR = attenuated total reflection

ARI = azimuthal rotation illumination

BFP = back focal plane

BSW = Bloch surface wave

BSWM = Bloch surface wave microscopy

BSA = bovine serum albumin

COBRI = coherent bright-field microscopy

CCMV = cowpea chlorotic mottle virus

cryo-EM = cryo-electron microscopy

DIC = differential interference contrast

DLS = dynamic light scattering

FBS = fetal bovine serum

FOV = field of view



FWHM = full width at half-maximum  
 GNP = gold nanoparticle  
 GNR = gold nanorod  
 HBsAg = hepatitis B surface antigen  
 IgA = human immunoglobulin A  
 IgM = human immunoglobulin M  
 ITO = indium tin oxide  
 IRM = interference reflection microscopy  
 iPM = interferometric plasmonic microscopy  
 IRIS = interferometric reflectance imaging sensor  
 iSCAT = interferometric scattering microscopy  
 LED = light emitting diode  
 LSPR = localized surface plasmon  
 LRSPR = long-range surface plasmon resonance  
 MP = mass photometry  
 MS = mass spectrometry  
 MIP = mid-infrared photothermal  
 nanoCET = nanocapillary electrophoretic tracking  
 NA = numerical aperture  
 OmpF = outer membrane protein  
 PCM = phase contrast microscopy  
 PT-SLM = photothermal spatial light modulator  
 PFU = plaque-forming units  
 PSM = plasmonic scattering microscopy  
 P-EIM = plasmonic-based electrochemical impedance microscopy  
 PSF = point-spread function  
 PBS = polarizing beamsplitter  
 PEG = polyethylene glycol  
 QPD = quadrant photodiode  
 QWP = quarter wave plate  
 RICM = reflection interference contrast microscopy  
 ROI = region of interest  
 RF-SCAT = remote focusing interferometric scattering microscopy  
 ROCS = rotating coherent scattering  
 SEM = scanning electron microscopy  
 SLSPM = scanning localized surface plasmon microscopy  
 SNR = signal-to-noise ratio  
 SP-IRIS = single-particle interferometric reflectance imaging sensor  
 SPT = single-particle tracking  
 miRNA = single-strand microRNA  
 SP = surface plasmon  
 SPP = surface plasmon polaritons  
 SPR = surface plasmon resonance  
 SPRI = surface plasmon resonance imaging  
 SPRM = surface plasmon resonance microscopy  
 SPCEM = surface plasmon-coupled emission microscopy  
 TIR = total internal reflection  
 TIRF = total internal reflection fluorescence  
 TIRS = total internal reflection scattering  
 2D-SPR = two-dimensional surface plasmon resonance  
 TFP = type IV pili  
 VSV = vesicular stomatitis virus  
 WSM = waveguide scattering microscopy

## REFERENCES

- (1) Binnig, G.; Rohrer, H.; Gerber, C.; Weibel, E. Surface Studies by Scanning Tunneling Microscopy. *Phys. Rev. Lett.* **1982**, *49*, 57–61.
- (2) Eigler, D. M.; Schweizer, E. K. Positioning Single Atoms with a Scanning Tunneling Microscope. *Nature* **1990**, *344*, 524–526.

- (3) Binnig, G.; Quate, C. F.; Gerber, C. Atomic Force Microscope. *Phys. Rev. Lett.* **1986**, *56*, 930–933.
- (4) Ando, T.; Kodera, N.; Takai, E.; Maruyama, D.; Saito, K.; Toda, A. A High-Speed Atomic Force Microscope for Studying Biological Macromolecules. *Proc. Natl. Acad. Sci. U. S. A.* **2001**, *98*, 12468–12472.
- (5) Moerner, W. E.; Kador, L. Optical Detection and Spectroscopy of Single Molecules in a Solid. *Phys. Rev. Lett.* **1989**, *62*, 2535–2538.
- (6) Orrit, M.; Bernard, J. Single Pentacene Molecules Detected by Fluorescence Excitation in a P-Terphenyl Crystal. *Phys. Rev. Lett.* **1990**, *65*, 2716–2719.
- (7) Neuhauser, W.; Hohenstatt, M.; Toschek, P. E.; Dehmelt, H. Localized Visible Ba<sup>+</sup> Mono-Ion Oscillator. *Phys. Rev. A: At., Mol., Opt. Phys.* **1980**, *22*, 1137–1140.
- (8) Moerner, W. E.; Orrit, M. Illuminating Single Molecules in Condensed Matter. *Science* **1999**, *283*, 1670–1676.
- (9) Dickson, R. M.; Cubitt, A. B.; Tsien, R. Y.; Moerner, W. E. On/off Blinking and Switching Behaviour of Single Molecules of Green Fluorescent Protein. *Nature* **1997**, *388*, 355–358.
- (10) Betzig, E.; Patterson, G. H.; Sougrat, R.; Lindwasser, O. W.; Olenych, S.; Bonifacio, J. S.; Davidson, M. W.; Lippincott-Schwartz, J.; Hess, H. F. Imaging Intracellular Fluorescent Proteins at Nanometer Resolution. *Science* **2006**, *313*, 1642–1645.
- (11) Rust, M. J.; Bates, M.; Zhuang, X. Sub-Diffraction-Limit Imaging by Stochastic Optical Reconstruction Microscopy (STORM). *Nat. Methods* **2006**, *3*, 793–795.
- (12) Hess, S. T.; Girirajan, T. P. K.; Mason, M. D. Ultra-High Resolution Imaging by Fluorescence Photoactivation Localization Microscopy. *Biophys. J.* **2006**, *91*, 4258–4272.
- (13) Dempsey, G. T.; Vaughan, J. C.; Chen, K. H.; Bates, M.; Zhuang, X. Evaluation of Fluorophores for Optimal Performance in Localization-Based Super-Resolution Imaging. *Nat. Methods* **2011**, *8*, 1027–1040.
- (14) Gwosch, K. C.; Pape, J. K.; Balzarotti, F.; Hoess, P.; Ellenberg, J.; Ries, J.; Hell, S. W. MINIFLUX Nanoscopy Delivers 3D Multicolor Nanometer Resolution in Cells. *Nat. Methods* **2020**, *17*, 217–224.
- (15) Siedentopf, H.; Zsigmondy, R. Über Sichtbarmachung Und Größenbestimmung Ultramikroskopischer Teilchen, Mit Besonderer Anwendung Auf Goldrubingläser. *Ann. Phys.* **1902**, *315*, 1–39.
- (16) Zernike, F. Das Phasenkontrastverfahren Bei Der Mikroskopischen Beobachtung. *Z. Technol. Phys.* **1935**, *16*, 454–457.
- (17) Zernike, F. Phase Contrast, a New Method for the Microscopic Observation of Transparent Objects. *Physica* **1942**, *9*, 686–698.
- (18) Zernike, F. Phase Contrast, a New Method for the Microscopic Observation of Transparent Objects Part II. *Physica* **1942**, *9*, 974–986.
- (19) Nomarski, G. Microinterferomètre Différentiel à Ondes Polarisées. *J. Phys. Radium* **1955**, *16*, 9S–11S.
- (20) Allen, R. D.; David, G. B.; Nomarski, G. The Zeiss-Nomarski Differential Interference Equipment for Transmitted-Light Microscopy. *Z. Wiss. Mikrosk.* **1969**, *69*, 193–221.
- (21) Curtis, A. S. The Mechanism of Adhesion of Cells to Glass. A Study by Interference Reflection Microscopy. *J. Cell Biol.* **1964**, *20*, 199–215.
- (22) Verschuieren, H. Interference Reflection Microscopy in Cell Biology: Methodology and Applications. *J. Cell Sci.* **1985**, *75*, 279–301.
- (23) Ploem, J. S. *Reflection-Contrast Microscopy as a Tool for Investigation of the Attachment of Living Cells to a Glass Surface*; Van Furth, R., Ed.; Blackwell Scientific: Oxford, 1975.
- (24) Limozin, L.; Sengupta, K. Quantitative Reflection Interference Contrast Microscopy (RICM) in Soft Matter and Cell Adhesion. *ChemPhysChem* **2009**, *10*, 2752–2768.
- (25) Gaiduk, A.; Yorulmaz, M.; Ruijgrok, P. V.; Orrit, M. Room-Temperature Detection of a Single Molecule's Absorption by Photothermal Contrast. *Science* **2010**, *330*, 353–356.
- (26) Celebrano, M.; Kukura, P.; Renn, A.; Sandoghdar, V. Single-Molecule Imaging by Optical Absorption. *Nat. Photonics* **2011**, *5*, 95–98.
- (27) Chong, S.; Min, W.; Xie, X. S. Ground-State Depletion Microscopy: Detection Sensitivity of Single-Molecule Optical

Absorption at Room Temperature. *J. Phys. Chem. Lett.* **2010**, *1*, 3316–3322.

(28) Vollmer, F.; Arnold, S. Whispering-Gallery-Mode Biosensing: Label-Free Detection down to Single Molecules. *Nat. Methods* **2008**, *5*, 591–596.

(29) Vollmer, F.; Swaim, J. D.; Foreman, M. R. Whispering Gallery Mode Sensors. *Adv. Opt. Photonics* **2015**, *7*, 168–240.

(30) Baaske, M. D.; Vollmer, F. Optical Observation of Single Atomic Ions Interacting with Plasmonic Nanorods in Aqueous Solution. *Nat. Photonics* **2016**, *10*, 733–739.

(31) Abbe, E. Beiträge Zur Theorie Des Mikroskops Und Der Mikroskopischen Wahrnehmung: I. Die Construction von Mikroskopen Auf Grund Der Theorie. *Arch. für mikroskopische Anat.* **1873**, *9*, 413–418.

(32) Ortega Arroyo, J.; Andrecka, J.; Spillane, K. M.; Billington, N.; Takagi, Y.; Sellers, J. R.; Kukura, P. Label-Free, All-Optical Detection, Imaging, and Tracking of a Single Protein. *Nano Lett.* **2014**, *14*, 2065–2070.

(33) Piliarik, M.; Sandoghdar, V. Direct Optical Sensing of Single Unlabelled Proteins and Super-Resolution Imaging of Their Binding Sites. *Nat. Commun.* **2014**, *5*, 4495.

(34) Young, G.; Hundt, N.; Cole, D.; Fineberg, A.; Andrecka, J.; Tyler, A.; Olerinyova, A.; Ansari, A.; Marklund, E. G.; Collier, M. P.; et al. Quantitative Mass Imaging of Single Biological Macromolecules. *Science* **2018**, *360*, 423–427.

(35) Stallinga, S.; Rieger, B. Accuracy of the Gaussian Point Spread Function Model in 2D Localization Microscopy. *Opt. Express* **2010**, *18*, 24461.

(36) Thompson, R. E.; Larson, D. R.; Webb, W. W. Precise Nanometer Localization Analysis for Individual Fluorescent Probes. *Biophys. J.* **2002**, *82*, 2775–2783.

(37) Bohren, C. F.; Huffman, D. R. *Absorption and Scattering of Light by Small Particles*; John Wiley & Sons: New York, 1983.

(38) Agio, M.; Mojarad, N. M.; Sandoghdar, V. Plasmon Spectra of Nanospheres under a Tightly Focused Beam. *J. Opt. Soc. Am. B* **2008**, *25*, 651–658.

(39) Lieb, M. A.; Zavislan, J. M.; Novotny, L. Single-Molecule Orientations Determined by Direct Emission Pattern Imaging. *J. Opt. Soc. Am. B* **2004**, *21*, 1210–1215.

(40) Brokmann, X.; Coolen, L.; Hermier, J. P.; Dahan, M. Emission Properties of Single CdSe/ZnS Quantum Dots Close to a Dielectric Interface. *Chem. Phys.* **2005**, *318*, 91–98.

(41) Lee, K. G.; Chen, X. W.; Eghlidi, H.; Kukura, P.; Lettow, R.; Renn, A.; Sandoghdar, V.; Götzinger, S. A Planar Dielectric Antenna for Directional Single-Photon Emission and near-Unity Collection Efficiency. *Nature Photonics* **2011**, *166*–169, DOI: 10.1038/nphoton.2010.312.

(42) Weigel, A.; Sebesta, A.; Kukura, P. Dark Field Microspectroscopy with Single Molecule Fluorescence Sensitivity. *ACS Photonics* **2014**, *1*, 848–856.

(43) Cole, D.; Young, G.; Weigel, A.; Sebesta, A.; Kukura, P. Label-Free Single-Molecule Imaging with Numerical-Aperture-Shaped Interferometric Scattering Microscopy. *ACS Photonics* **2017**, *4*, 211–216.

(44) Liebel, M.; Hugall, J. T.; Van Hulst, N. F. Ultrasensitive Label-Free Nanosensing and High-Speed Tracking of Single Proteins. *Nano Lett.* **2017**, *17*, 1277–1281.

(45) Avci, O.; Campana, M. I.; Yurdakul, C.; Selim Ünlü, M. Pupil Function Engineering for Enhanced Nanoparticle Visibility in Wide-Field Interferometric Microscopy. *Optica* **2017**, *4*, 247–254.

(46) Horio, T.; Hotani, H. Visualization of the Dynamic Instability of Individual Microtubules by Dark-Field Microscopy. *Nature* **1986**, *321*, 605–607.

(47) Kudo, S.; Magariyama, Y.; Aizawa, S. I. Abrupt Changes in Flagellar Rotation Observed by Laser Dark-Field Microscopy. *Nature* **1990**, *346*, 677–680.

(48) Nishiyama, M.; Muto, E.; Inoue, Y.; Yanagida, T.; Higuchi, H. Substeps within the 8-Nm Step of the ATPase Cycle of Single Kinesin Molecules. *Nat. Cell Biol.* **2001**, *3*, 425–428.

(49) Yasuda, R.; Noji, H.; Yoshida, M.; Kinoshita, K.; Itoh, H. Resolution of Distinct Rotational Substeps by Submillisecond Kinetic Analysis of F1-ATPase. *Nature* **2001**, *410*, 898–904.

(50) Dunn, A. R.; Spudich, J. A. Dynamics of the Unbound Head during Myosin V Processive Translocation. *Nat. Struct. Mol. Biol.* **2007**, *14*, 246–248.

(51) Axelrod, D. Total Internal Reflection Fluorescence Microscopy in Cell Biology. *Traffic* **2001**, *2*, 764–774.

(52) Schneckenburger, H. Total Internal Reflection Fluorescence Microscopy: Technical Innovations and Novel Applications. *Curr. Opin. Biotechnol.* **2005**, *16*, 13–18.

(53) Mattheyses, A. L.; Simon, S. M.; Rappoport, J. Z. Imaging with Total Internal Reflection Fluorescence Microscopy for the Cell Biologist. *J. Cell Sci.* **2010**, *123*, 3621–3628.

(54) Ambrose, E. J. A Surface Contact Microscope for the Study of Cell Movements. *Nature* **1956**, *178*, 1194.

(55) Ambrose, E. J. The Movements of Fibrocytes. *Exp. Cell Res.* **1961**, *8*, 54–73.

(56) Braslavsky, I.; Amit, R.; Jaffar Ali, B. M.; Gileadi, O.; Oppenheim, A.; Stavans, J. Objective-Type Dark-Field Illumination for Scattering from Microbeads. *Appl. Opt.* **2001**, *40*, 5650–5657.

(57) Stout, A. L.; Axelrod, D. Evanescent Field Excitation of Fluorescence by Epi-Illumination Microscopy. *Appl. Opt.* **1989**, *28*, 5237–5242.

(58) Meng, X.; Sonn-Segev, A.; Schumacher, A.; Cole, D.; Young, G.; Thorpe, S.; Style, R. W.; Dufresne, E. R.; Kukura, P. Micromirror Total Internal Reflection Microscopy for High-Performance Single Particle Tracking at Interfaces. *arXiv2021*, 2103.09738

(59) Ueno, H.; Nishikawa, S.; Iino, R.; Tabata, K. V.; Sakakihara, S.; Yanagida, T.; Noji, H. Simple Dark-Field Microscopy with Nanometer Spatial Precision and Microsecond Temporal Resolution. *Biophys. J.* **2010**, *98*, 2014–2023.

(60) Kobayashi, R.; Ueno, H.; Li, C. B.; Noji, H. Rotary Catalysis of Bovine Mitochondrial F1-ATPase Studied by Single-Molecule Experiments. *Proc. Natl. Acad. Sci. U. S. A.* **2020**, *117*, 1447–1456.

(61) Watanabe, R.; Minagawa, Y.; Noji, H. Thermodynamic Analysis of F<sub>1</sub>-ATPase Rotary Catalysis Using High-Speed Imaging. *Protein Sci.* **2014**, *23*, 1773–1779.

(62) Li, C. B.; Ueno, H.; Watanabe, R.; Noji, H.; Komatsuzaki, T. ATP Hydrolysis Assists Phosphate Release and Promotes Reaction Ordering in F1-ATPase. *Nat. Commun.* **2015**, *6*, 10223.

(63) Watanabe, R.; Hayashi, K.; Ueno, H.; Noji, H. Catalysis-Enhancement via Rotary Fluctuation of F1-ATPase. *Biophys. J.* **2013**, *105*, 2385–2391.

(64) Hayashi, S.; Ueno, H.; Shaikh, A. R.; Umemura, M.; Kamiya, M.; Ito, Y.; Ikeguchi, M.; Komoriya, Y.; Iino, R.; Noji, H. Molecular Mechanism of ATP Hydrolysis in F1-ATPase Revealed by Molecular Simulations and Single-Molecule Observations. *J. Am. Chem. Soc.* **2012**, *134*, 8447–8454.

(65) Minagawa, Y.; Ueno, H.; Hara, M.; Ishizuka-Katsura, Y.; Ohsawa, N.; Terada, T.; Shirouzu, M.; Yokoyama, S.; Yamato, I.; Muneyuki, E.; et al. Basic Properties of Rotary Dynamics of the Molecular Motor *Enterococcus Hiraе* V1-ATPase. *J. Biol. Chem.* **2013**, *288*, 32700–32707.

(66) Iida, T.; Minagawa, Y.; Ueno, H.; Kawai, F.; Murata, T.; Iino, R. Single-Molecule Analysis Reveals Rotational Substeps and Chemo-Mechanical Coupling Scheme of *Enterococcus Hiraе* V1-ATPase. *J. Biol. Chem.* **2019**, *294*, 17017–17030.

(67) Ueno, H.; Minagawa, Y.; Hara, M.; Rahman, S.; Yamato, I.; Muneyuki, E.; Noji, H.; Murata, T.; Iino, R. Torque Generation of *Enterococcus Hiraе* V-ATPase. *J. Biol. Chem.* **2014**, *289*, 31212–31223.

(68) Nishikawa, S.; Arimoto, I.; Ikezaki, K.; Sugawa, M.; Ueno, H.; Komori, T.; Iwane, A. H.; Yanagida, T. Switch between Large Hand-Over-Hand and Small Inchworm-like Steps in Myosin VI. *Cell* **2010**, *142*, 879–888.

(69) Isojima, H.; Iino, R.; Niitani, Y.; Noji, H.; Tomishige, M. Direct Observation of Intermediate States during the Stepping Motion of Kinesin-1. *Nat. Chem. Biol.* **2016**, *12*, 290–297.

- (70) Nakamura, A.; Okazaki, K.-i.; Furuta, T.; Sakurai, M.; Iino, R. Processive Chitinase Is Brownian Monorail Operated by Fast Catalysis after Peeling Rail from Crystalline Chitin. *Nat. Commun.* **2018**, *9*, 3814.
- (71) Enoki, S.; Iino, R.; Morone, N.; Kaihatsu, K.; Sakakihara, S.; Kato, N.; Noji, H. Label-Free Single-Particle Imaging of the Influenza Virus by Objective-Type Total Internal Reflection Dark-Field Microscopy. *PLoS One* **2012**, *7*, No. e49208.
- (72) Ando, J.; Nakamura, A.; Visoosat, A.; Yamamoto, M.; Song, C.; Murata, K.; Iino, R. Single-Nanoparticle Tracking with Angstrom Localization Precision and Microsecond Time Resolution. *Biophys. J.* **2018**, *115*, 2413–2427.
- (73) Ando, J.; Shima, T.; Kanazawa, R.; Shimo-Kon, R.; Nakamura, A.; Yamamoto, M.; Kon, T.; Iino, R. Small Stepping Motion of Processive Dynein Revealed by Load-Free High-Speed Single-Particle Tracking. *Sci. Rep.* **2020**, *10*, 1080.
- (74) Ando, J.; Nakamura, A.; Yamamoto, M.; Song, C.; Murata, K.; Iino, R. Multicolor High-Speed Tracking of Single Biomolecules with Silver, Gold, and Silver-Gold Alloy Nanoparticles. *ACS Photonics* **2019**, *6*, 2870–2883.
- (75) Sönnichsen, C.; Alivisatos, A. P. Gold Nanorods as Novel Nonbleaching Plasmon-Based Orientation Sensors for Polarized Single-Particle Microscopy. *Nano Lett.* **2005**, *5*, 301–304.
- (76) Huang, X.; Neretina, S.; El-Sayed, M. A. Gold Nanorods: From Synthesis and Properties to Biological and Biomedical Applications. *Adv. Mater.* **2009**, *21*, 4880–4910.
- (77) Mazaheri, M.; Ehrig, J.; Shkarin, A.; Zaburdaev, V.; Sandoghdar, V. Ultrahigh-Speed Imaging of Rotational Diffusion on a Lipid Bilayer. *Nano Lett.* **2020**, *20*, 7213–7219.
- (78) Wicker, K.; Heintzmann, R. Resolving a Misconception about Structured Illumination. *Nat. Photonics* **2014**, *8*, 342–344.
- (79) Cronin, D. J.; Smith, A. E. Dynamic Coherent Optical System. *Opt. Eng.* **1973**, *12*, 120250.
- (80) Cotte, Y.; Toy, F.; Jourdain, P.; Pavillon, N.; Boss, D.; Magistretti, P.; Marquet, P.; Depeursinge, C. Marker-Free Phase Nanoscopy. *Nat. Photonics* **2013**, *7*, 113–117.
- (81) Zheng, G.; Horstmeyer, R.; Yang, C. Wide-Field, High-Resolution Fourier Ptychographic Microscopy. *Nat. Photonics* **2013**, *7*, 739–745.
- (82) Maire, G.; Giovannini, H.; Talneau, A.; Chaumet, P. C.; Belkebir, K.; Sentenac, A. Phase Imaging and Synthetic Aperture Super-Resolution via Total Internal Reflection Microscopy. *Opt. Lett.* **2018**, *43*, 2173–2176.
- (83) Chowdhury, S.; Dhalla, A.-H.; Izatt, J. Structured Oblique Illumination Microscopy for Enhanced Resolution Imaging of Non-Fluorescent, Coherently Scattering Samples. *Biomed. Opt. Express* **2012**, *3*, 1841–1854.
- (84) von Olshausen, P.; Rohrbach, A. Coherent Total Internal Reflection Dark-Field Microscopy: Label-Free Imaging beyond the Diffraction Limit. *Opt. Lett.* **2013**, *38*, 4066–4069.
- (85) Jünger, F.; Olshausen, P. V.; Rohrbach, A. Fast, Label-Free Super-Resolution Live-Cell Imaging Using Rotating Coherent Scattering (ROCS) Microscopy. *Sci. Rep.* **2016**, *6*, 30393 DOI: 10.1038/srep30393.
- (86) Heintzmann, R.; Cremer, C. G. Laterally Modulated Excitation Microscopy: Improvement of Resolution by Using a Diffraction Grating. In *Optical Biopsies and Microscopic Techniques III*; SPIE, 1999; Vol. 3568, pp 185–196 DOI: 10.1117/12.336833.
- (87) Gustafsson, M. G. L. Surpassing the Lateral Resolution Limit by a Factor of Two Using Structured Illumination Microscopy. *J. Microsc.* **2000**, *198*, 82–87.
- (88) Heintzmann, R.; Huser, T. Super-Resolution Structured Illumination Microscopy. *Chem. Rev.* **2017**, *117*, 13890–13908.
- (89) Koch, M. D.; Rohrbach, A. Label-Free Imaging and Bending Analysis of Microtubules by ROCS Microscopy and Optical Trapping. *Biophys. J.* **2018**, *114*, 168–177.
- (90) Jünger, F.; Rohrbach, A. Strong Cytoskeleton Activity on Millisecond Timescales upon Particle Binding Revealed by ROCS Microscopy. *Cytoskeleton* **2018**, *75*, 410–424.
- (91) Ruh, D.; Mutschler, J.; Michelbach, M.; Rohrbach, A. Superior Contrast and Resolution by Image Formation in Rotating Coherent Scattering (ROCS) Microscopy. *Optica* **2018**, *5*, 1371–1381.
- (92) Nan, X.; Sims, P. A.; Xie, X. S. Organelle Tracking in a Living Cell with Microsecond Time Resolution and Nanometer Spatial Precision. *ChemPhysChem* **2008**, *9*, 707–712.
- (93) Sudhakar, S.; Abdosamadi, M. K.; Jachowski, T. J.; Bugiel, M.; Jannasch, A.; Schäffer, E. Germanium Nanospheres for Ultraresolution Picotensometry of Kinesin Motors. *Science* **2021**, *371*, No. eabd9944.
- (94) Mickolajczyk, K. J.; Deffenbaugh, N. C.; Ortega Arroyo, J.; Andrecka, J.; Kukura, P.; Hancock, W. O. Kinetics of Nucleotide-Dependent Structural Transitions in the Kinesin-1 Hydrolysis Cycle. *Proc. Natl. Acad. Sci. U. S. A.* **2015**, *112*, E7186–E7193.
- (95) Sowa, Y.; Steel, B. C.; Berry, R. M. A Simple Backscattering Microscope for Fast Tracking of Biological Molecules. *Rev. Sci. Instrum.* **2010**, *81*, 113704.
- (96) Nord, A. L.; Sowa, Y.; Steel, B. C.; Lo, C. J.; Berry, R. M. Speed of the Bacterial Flagellar Motor near Zero Load Depends on the Number of Stator Units. *Proc. Natl. Acad. Sci. U. S. A.* **2017**, *114*, 11603–11608.
- (97) Lo, C. J.; Sowa, Y.; Pilizota, T.; Berry, R. M. Mechanism and Kinetics of a Sodium-Driven Bacterial Flagellar Motor. *Proc. Natl. Acad. Sci. U. S. A.* **2013**, *110*, E2544–E2551.
- (98) Xiao, L.; Qiao, Y.; He, Y.; Yeung, E. S. Three Dimensional Orientational Imaging of Nanoparticles with Darkfield Microscopy. *Anal. Chem.* **2010**, *82*, 5268–5274.
- (99) Enoki, S.; Iino, R.; Niitani, Y.; Minagawa, Y.; Tomishige, M.; Noji, H. High-Speed Angle-Resolved Imaging of a Single Gold Nanorod with Microsecond Temporal Resolution and One-Degree Angle Precision. *Anal. Chem.* **2015**, *87*, 2079–2086.
- (100) Grandin, H. M.; Städler, B.; Textor, M.; Vörös, J. Waveguide Excitation Fluorescence Microscopy: A New Tool for Sensing and Imaging the Biointerface. *Biosens. Bioelectron.* **2006**, *21*, 1476–1482.
- (101) Agnarsson, B.; Ingthorsson, S.; Gudjonsson, T.; Leosson, K. Evanescent-Wave Fluorescence Microscopy Using Symmetric Planar Waveguides. *Opt. Express* **2009**, *17*, 5075–5082.
- (102) Archetti, A.; Glushkov, E.; Sieben, C.; Stroganov, A.; Radenovic, A.; Manley, S. Waveguide-PAINT Offers an Open Platform for Large Field-of-View Super-Resolution Imaging. *Nat. Commun.* **2019**, *10*, 1267.
- (103) Thoma, F.; Langbein, U.; Mittler-Neher, S. Waveguide Scattering Microscopy. *Opt. Commun.* **1997**, *134*, 16–20.
- (104) Ni, W.; Chen, H.; Kou, X.; Yeung, M. H.; Wang, J. Optical Fiber-Excited Surface Plasmon Resonance Spectroscopy of Single and Ensemble Gold Nanorods. *J. Phys. Chem. C* **2008**, *112*, 8105–8109.
- (105) Hill, D. J.; Pinion, C. W.; Christesen, J. D.; Cahoon, J. F. Waveguide Scattering Microscopy for Dark-Field Imaging and Spectroscopy of Photonic Nanostructures. *ACS Photonics* **2014**, *1*, 725–731.
- (106) Agnarsson, B.; Lundgren, A.; Gunnarsson, A.; Rabe, M.; Kunze, A.; Mapar, M.; Simonsson, L.; Bally, M.; Zhdanov, V. P.; Höök, F. Evanescent Light-Scattering Microscopy for Label-Free Interfacial Imaging: From Single Sub-100 Nm Vesicles to Live Cells. *ACS Nano* **2015**, *9*, 11849–11862.
- (107) Agnarsson, B.; Mapar, M.; Sjöberg, M.; Alizadeheidari, M.; Höök, F. Low-Temperature Fabrication and Characterization of a Symmetric Hybrid Organic-Inorganic Slab Waveguide for Evanescent Light Microscopy. *Nano Futures* **2018**, *2*, 025007.
- (108) Lundgren, A.; Agnarsson, B.; Zirbs, R.; Zhdanov, V. P.; Reimhult, E.; Hook, F. Nonspecific Colloidal-Type Interaction Explains Size-Dependent Specific Binding of Membrane-Targeted Nanoparticles Article. *ACS Nano* **2016**, *10*, 9974–9982.
- (109) Agnarsson, B.; Wayment-Steele, H. K.; Höök, F.; Kunze, A. Monitoring of Single and Double Lipid Membrane Formation with High Spatiotemporal Resolution Using Evanescent Light Scattering Microscopy †. *Nanoscale* **2016**, *8*, 19219.
- (110) Rupert, D. L. M.; Mapar, M.; Shelke, G. V.; Norling, K.; Elmeskog, M.; Lotvall, J. O.; Block, S.; Bally, M.; Agnarsson, B.; Hook, F. Effective Refractive Index and Lipid Content of Extracellular Vesicles



Revealed Using Optical Waveguide Scattering and Fluorescence Microscopy. *Langmuir* **2018**, *34*, 8522–8531.

(111) Hannestad, J. K.; Rocha, S.; Agnarsson, B.; Zhdanov, V. P.; Wittung-Stafshede, P.; Höök, F. Single-Vesicle Imaging Reveals Lipid-Selective and Stepwise Membrane Disruption by Monomeric  $\alpha$ -Synuclein. *Proc. Natl. Acad. Sci. U. S. A.* **2020**, *117*, 14178–14186.

(112) Faez, S.; Lahini, Y.; Weidlich, S.; Garmann, R. F.; Wondraczek, K.; Zeisberger, M.; Schmidt, M. A.; Orrit, M.; Manoharan, V. N. Fast, Label-Free Tracking of Single Viruses and Weakly Scattering Nanoparticles in a Nanofluidic Optical Fiber. *ACS Nano* **2015**, *9*, 12349–12357.

(113) Faez, S.; Samin, S.; Baasanjav, D.; Weidlich, S.; Schmidt, M.; Mosk, A. P. Nanocapillary Electrokinetic Tracking for Monitoring Charge Fluctuations on a Single Nanoparticle. *Faraday Discuss.* **2016**, *193*, 447–458.

(114) Jiang, S.; Zhao, J.; Förster, R.; Weidlich, S.; Plidschun, M.; Kobelke, J.; Fatobene Ando, R.; Schmidt, M. A. Three Dimensional Spatiotemporal Nano-Scale Position Retrieval of the Confined Diffusion of Nano-Objects inside Optofluidic Microstructured Fibers. *Nanoscale* **2020**, *12*, 3146–3156.

(115) Jiang, S.; Förster, R.; Plidschun, M.; Kobelke, J.; Fatobene Ando, R.; Schmidt, M. A. Three-Dimensional Spatiotemporal Tracking of Nano-Objects Diffusing in Water-Filled Optofluidic Microstructured Fiber. *Nanophotonics* **2020**, *9*, 4545–4554.

(116) Förster, R.; Weidlich, S.; Nissen, M.; Wieduwilt, T.; Kobelke, J.; Goldfain, A. M.; Chiang, T. K.; Garmann, R. F.; Manoharan, V. N.; Lahini, Y.; et al. Tracking and Analyzing the Brownian Motion of Nano-Objects Inside Hollow Core Fibers. *ACS Sensors* **2020**, *5*, 879–886.

(117) Hartung, A.; Kobelke, J.; Schwuchow, A.; Bierlich, J.; Popp, J.; Schmidt, M. A.; Frosch, T. Low-Loss Single-Mode Guidance in Large-Core Antiresonant Hollow-Core Fibers. *Opt. Lett.* **2015**, *40*, 3432–3435.

(118) Kukura, P.; Ewers, H.; Müller, C.; Renn, A.; Helenius, A.; Sandoghdar, V. High-Speed Nanoscopic Tracking of the Position and Orientation of a Single Virus. *Nat. Methods* **2009**, *6*, 923–927.

(119) Amos, L. A.; Amos, W. B. The Bending of Sliding Microtubules Imaged by Confocal Light Microscopy and Negative Stain Electron Microscopy. *J. Cell Sci.* **1991**, *1991*, 95–101.

(120) Lindfors, K.; Kalkbrenner, T.; Stoller, P.; Sandoghdar, V. Detection and Spectroscopy of Gold Nanoparticles Using Supercontinuum White Light Confocal Microscopy. *Phys. Rev. Lett.* **2004**, *93*, 037401.

(121) Jacobsen, V.; Stoller, P.; Brunner, C.; Vogel, V.; Sandoghdar, V. Interferometric Optical Detection and Tracking of Very Small Gold Nanoparticles at a Water-Glass Interface. *Opt. Express* **2006**, *14*, 405–414.

(122) Ewers, H.; Jacobsen, V.; Klotzsch, E.; Smith, A. E.; Helenius, A.; Sandoghdar, V. Label-Free Optical Detection and Tracking of Single Virions Bound to Their Receptors in Supported Membrane Bilayers. *Nano Lett.* **2007**, *7*, 2263–2266.

(123) Kukura, P.; Celebrano, M.; Renn, A.; Sandoghdar, V. Imaging a Single Quantum Dot When It Is Dark. *Nano Lett.* **2009**, *9*, 926–929.

(124) Holanová, K.; Vala, M.; Piliarik, M. Optical Imaging and Localization of Prospective Scattering Labels Smaller than a Single Protein. *Opt. Laser Technol.* **2019**, *109*, 323–327.

(125) Ortega-Arroyo, J.; Kukura, P. Interferometric Scattering Microscopy (ISCAT): New Frontiers in Ultrafast and Ultrasensitive Optical Microscopy. *Phys. Chem. Chem. Phys.* **2012**, *14*, 15625–15636.

(126) Taylor, R. W.; Sandoghdar, V. Interferometric Scattering Microscopy: Seeing Single Nanoparticles and Molecules via Rayleigh Scattering. *Nano Lett.* **2019**, *19*, 4827–4835.

(127) Taylor, R. W.; Sandoghdar, V. Interferometric Scattering (ISCAT) Microscopy and Related Techniques. In *Label-Free Super-Resolution Microscopy. Biological and Medical Physics, Biomedical Engineering*; Astratov, V., Ed.; Springer: Cham, 2019.

(128) Young, G.; Kukura, P. Interferometric Scattering Microscopy. *Annu. Rev. Phys. Chem.* **2019**, *70*, 301–322.

(129) Lin, Y.-H.; Chang, W.-L.; Hsieh, C.-L. Shot-Noise Limited Localization of Single 20 Nm Gold Particles with Nanometer Spatial Precision within Microseconds. *Opt. Express* **2014**, *22*, 9159–9170.

(130) Spindler, S.; Ehrig, J.; König, K.; Nowak, T.; Piliarik, M.; Stein, H. E.; Taylor, R. W.; Garanger, E.; Lecommandoux, S.; Alves, I. D.; et al. Visualization of Lipids and Proteins at High Spatial and Temporal Resolution via Interferometric Scattering (ISCAT) Microscopy. *J. Phys. D: Appl. Phys.* **2016**, *49*, 274002.

(131) Liao, Y. H.; Lin, C. H.; Cheng, C. Y.; Wong, W. C.; Juo, J. Y.; Hsieh, C. L. Monovalent and Oriented Labeling of Gold Nanoprobes for the High-Resolution Tracking of a Single-Membrane Molecule. *ACS Nano* **2019**, *13*, 10918–10928.

(132) Spindler, S.; Sibold, J.; Gholami Mahmoodabadi, R.; Steinem, C.; Sandoghdar, V. High-Speed Microscopy of Diffusion in Pore-Spanning Lipid Membranes. *Nano Lett.* **2018**, *18*, S262–S271.

(133) Andrecka, J.; Takagi, Y.; Mickolajczyk, K. J. J.; Lippert, L. G. G.; Sellers, J. R. R.; Hancock, W. O. O.; Goldman, Y. E. E.; Kukura, P. Interferometric Scattering Microscopy for the Study of Molecular Motors. *Methods Enzymol.* **2016**, *581*, 517–539.

(134) Andrecka, J.; Ortega Arroyo, J.; Takagi, Y.; de Wit, G.; Fineberg, A.; MacKinnon, L.; Young, G.; Sellers, J. R.; Kukura, P. Structural Dynamics of Myosin 5 during Processive Motion Revealed by Interferometric Scattering Microscopy. *eLife* **2015**, *4*, e05413.

(135) Mickolajczyk, K. J.; Geyer, E. A.; Kim, T.; Rice, L. M.; Hancock, W. O. Direct Observation of Individual Tubulin Dimers Binding to Growing Microtubules. *Proc. Natl. Acad. Sci. U. S. A.* **2019**, *116*, 7314–7322.

(136) Taylor, R. W.; Mahmoodabadi, R. G.; Rauschenberger, V.; Giessel, A.; Schambony, A.; Sandoghdar, V. Interferometric Scattering Microscopy Reveals Microsecond Nanoscopic Protein Motion on a Live Cell Membrane. *Nat. Photonics* **2019**, *13*, 480–487.

(137) de Wit, G.; Albrecht, D.; Ewers, H.; Kukura, P. Revealing Compartmentalized Diffusion in Living Cells with Interferometric Scattering Microscopy. *Biophys. J.* **2018**, *114*, 2945–2950.

(138) Taylor, R. W.; Holler, C.; Mahmoodabadi, R. G.; Küppers, M.; Dastjerdi, H. M.; Zaburdaev, V.; Schambony, A.; Sandoghdar, V. High-Precision Protein-Tracking With Interferometric Scattering Microscopy. *Front. Cell Dev. Biol.* **2020**, *8*, 590158.

(139) Krishnan, M.; Mojarad, N.; Kukura, P.; Sandoghdar, V. Geometry-Induced Electrostatic Trapping of Nanometric Objects in a Fluid. *Nature* **2010**, *467*, 692–695.

(140) Mahmoodabadi, R. G.; Taylor, R. W.; Kaller, M.; Spindler, S.; Sandoghdar, V. The Point Spread Function in Interferometric Scattering Microscopy (ISCAT). I. Aberrations in Defocusing and Axial Localization. *Opt. Express* **2020**, *28*, 25969–25988.

(141) Lee, I.-B.; Moon, H.-M.; Park, J.-S.; Zambochova, K.; Hong, S.-C.; Cho, M. Three-Dimensional Interferometric Scattering Microscopy via Remote Focusing Technique. *Opt. Lett.* **2020**, *45*, 2628–2631.

(142) Cohen, A. E.; Moerner, W. E. Method for Trapping and Manipulating Nanoscale Objects in Solution. *Appl. Phys. Lett.* **2005**, *86*, 093109.

(143) Wang, Q.; Goldsmith, R. H.; Jiang, Y.; Bockenbauer, S. D.; Moerner, W. E. Probing Single Biomolecules in Solution Using the Anti-Brownian Electrokinetic (ABEL) Trap. *Acc. Chem. Res.* **2012**, *45*, 1955–1964.

(144) Squires, A. H.; Lavania, A. A.; Dahlberg, P. D.; Moerner, W. E. Interferometric Scattering Enables Fluorescence-Free Electrokinetic Trapping of Single Nanoparticles in Free Solution. *Nano Lett.* **2019**, *19*, 4112–4117.

(145) Mojarad, N.; Sandoghdar, V.; Krishnan, M. Measuring Three-Dimensional Interaction Potentials Using Optical Interference. *Opt. Express* **2013**, *21*, 9377–9389.

(146) Tae Kim, J.; Spindler, S.; Sandoghdar, V. Scanning-Aperture Trapping and Manipulation of Single Charged Nanoparticles. *Nat. Commun.* **2014**, *5*, 3380.

(147) Tuna, Y.; Kim, J. T.; Liu, H. W.; Sandoghdar, V. Levitated Plasmonic Nanoantennas in an Aqueous Environment. *ACS Nano* **2017**, *11*, 7674–7678.

- (148) Eberle, P.; Höller, C.; Müller, P.; Suomalainen, M.; Greber, U. F.; Eghlidi, H.; Poulidakos, D. Single Entity Resolution Valving of Nanoscopic Species in Liquids. *Nat. Nanotechnol.* **2018**, *13*, 578–582.
- (149) Skaug, M. J.; Schwemmer, C.; Fringes, S.; Rawlings, C. D.; Knoll, A. W. Nanofluidic Rocking Brownian Motors. *Science* **2018**, *359*, 1505–1508.
- (150) Goldfain, A. M.; Garmann, R. F.; Jin, Y.; Lahini, Y.; Manoharan, V. N. Dynamic Measurements of the Position, Orientation, and DNA Content of Individual Unlabeled Bacteriophages. *J. Phys. Chem. B* **2016**, *120*, 6130–6138.
- (151) Garmann, R. F.; Goldfain, A. M.; Manoharan, V. N. Measurements of the Self-Assembly Kinetics of Individual Viral Capsids around Their RNA Genome. *Proc. Natl. Acad. Sci. U. S. A.* **2019**, *116*, 22485–22490.
- (152) Andrecka, J.; Ortega Arroyo, J.; Lewis, K.; Cross, R. A.; Kukura, P. Label-Free Imaging of Microtubules with Sub-Nm Precision Using Interferometric Scattering Microscopy. *Biophys. J.* **2016**, *110*, 214–217.
- (153) Lee, I.-B. B.; Moon, H.-M. M.; Joo, J.-H. H.; Kim, K.-H. H.; Hong, S.-C. C.; Cho, M. Interferometric Scattering Microscopy with Polarization-Selective Dual Detection Scheme: Capturing the Orientational Information of Anisotropic Nanometric Objects. *ACS Photonics* **2018**, *5*, 797–804.
- (154) Vala, M.; Bujak, Ł.; García Marín, A.; Holanová, K.; Henrichs, V.; Braun, M.; Lánský, Z.; Piliarik, M. Nanoscopic Structural Fluctuations of Disassembling Microtubules Revealed by Label Free Super Resolution Microscopy. *Small Methods* **2021**, *5*, 2000985.
- (155) Talà, L.; Fineberg, A.; Kukura, P.; Persat, A. *Pseudomonas Aeruginosa* Orchestrates Twitching Motility by Sequential Control of Type IV Pili Movements. *Nat. Microbiol.* **2019**, *4*, 774–780.
- (156) De Wit, G.; Danial, J. S. H.; Kukura, P.; Wallace, M. I. Dynamic Label-Free Imaging of Lipid Nanodomains. *Proc. Natl. Acad. Sci. U. S. A.* **2015**, *112*, 12299–12303.
- (157) Andrecka, J.; Spillane, K. M.; Ortega-Arroyo, J.; Kukura, P. Direct Observation and Control of Supported Lipid Bilayer Formation with Interferometric Scattering Microscopy. *ACS Nano* **2013**, *7*, 10662–10670.
- (158) Ortega-Arroyo, J.; Bissette, A. J.; Kukura, P.; Fletcher, S. P. Visualization of the Spontaneous Emergence of a Complex, Dynamic, and Autocatalytic System. *Proc. Natl. Acad. Sci. U. S. A.* **2016**, *113*, 11122–11126.
- (159) Lebedeva, M. A.; Palmieri, E.; Kukura, P.; Fletcher, S. P. Emergence and Rearrangement of Dynamic Supramolecular Aggregates Visualized by Interferometric Scattering Microscopy. *ACS Nano* **2020**, *14*, 11160–11168.
- (160) Engwerda, A. H. J.; Southworth, J.; Lebedeva, M. A.; Scanes, R. J. H.; Kukura, P.; Fletcher, S. P. Coupled Metabolic Cycles Allow Out-of-Equilibrium Autopoietic Vesicle Replication. *Angew. Chem.* **2020**, *132*, 20541–29546.
- (161) Stetefeld, J.; McKenna, S. A.; Patel, T. R. Dynamic Light Scattering: A Practical Guide and Applications in Biomedical Sciences. *Biophys. Rev.* **2016**, *8*, 409–427.
- (162) Falke, S.; Betzel, C. Dynamic Light Scattering (DLS). In *Radiation in Bioanalysis*; Nature Publishing Group, 2019; Vol. 8, pp 173–193.
- (163) McDonald, M. P.; Gemeinhardt, A.; König, K.; Piliarik, M.; Schaffer, S.; Völkl, S.; Aigner, M.; Mackensen, A.; Sandoghdar, V. Visualizing Single-Cell Secretion Dynamics with Single-Protein Sensitivity. *Nano Lett.* **2018**, *18*, 513–519.
- (164) Gemeinhardt, A.; McDonald, M. P.; König, K.; Aigner, M.; Mackensen, A.; Sandoghdar, V. Label-Free Imaging of Single Proteins Secreted from Living Cells via Iscat Microscopy. *J. Visualized Exp.* **2018**, *2018*, 58486.
- (165) McMeekin, T. L.; Wilensky, M.; Groves, M. L. Refractive Indices of Proteins in Relation to Amino Acid Composition and Specific Volume. *Biochem. Biophys. Res. Commun.* **1962**, *7*, 151–156.
- (166) Harpaz, Y.; Gerstein, M.; Chothia, C. Volume Changes on Protein Folding. *Structure* **1994**, *2*, 641–649.
- (167) Marklund, E. G.; Benesch, J. L. Weighing-up Protein Dynamics: The Combination of Native Mass Spectrometry and Molecular Dynamics Simulations. *Curr. Opin. Struct. Biol.* **2019**, *2019*, 50–58.
- (168) Boeri Erba, E.; Signor, L.; Petosa, C. Exploring the Structure and Dynamics of Macromolecular Complexes by Native Mass Spectrometry. *J. Proteomics* **2020**, *222*, 103799.
- (169) Robert, H. M. L.; Holanová, K.; Bujak, Ł.; Vala, M.; Henrichs, V.; Lánský, Z.; Piliarik, M. Fast Photothermal Spatial Light Modulation for Quantitative Phase Imaging at the Nanoscale. *Nat. Commun.* **2021**, *12*, 2921.
- (170) Hajdusits, B.; Suskiewicz, M. J.; Hundt, N.; Meinhart, A.; Kurzbauer, R.; Leodolter, J.; Kukura, P.; Clausen, T. McsB Forms a Gated Kinase Chamber to Mark Aberrant Bacterial Proteins for Degradation. *eLife* **2021**, *10*, e63505.
- (171) Bhatt, V.; Shi, K.; Salamango, D. J.; Moeller, N. H.; Pandey, K. K.; Bera, S.; Bohl, T. E.; Kurniawan, F.; Orellana, K.; Zhang, W.; et al. Structural Basis of Host Protein Hijacking in Human T-Cell Leukemia Virus Integration. *Nat. Commun.* **2020**, *11*, 3121.
- (172) England, R. M.; Moss, J. I.; Gunnarsson, A.; Parker, J. S.; Ashford, M. B. Synthesis and Characterization of Dendrimer-Based Polysarcosine Star Polymers: Well-Defined, Versatile Platforms Designed for Drug-Delivery Applications. *Biomacromolecules* **2020**, *21*, 3332–3341.
- (173) Fineberg, A.; Surrey, T.; Kukura, P. Quantifying the Monomer–Dimer Equilibrium of Tubulin with Mass Photometry. *J. Mol. Biol.* **2020**, *432*, 6168–6172.
- (174) Ye, X.; Vogt, M. S.; van der Does, C.; Bildl, W.; Schulte, U.; Essen, L.-O.; Albers, S.-V. The Phosphatase PP2A Interacts With ArnA and ArnB to Regulate the Oligomeric State and the Stability of the ArnA/B Complex. *Front. Microbiol.* **2020**, *11*, 1849.
- (175) Lonhienne, T.; Low, Y. S.; Garcia, M. D.; Croll, T.; Gao, Y.; Wang, Q.; Brillault, L.; Williams, C. M.; Fraser, J. A.; McGeary, R. P.; et al. Structures of Fungal and Plant Acetohydroxyacid Synthases. *Nature* **2020**, *586*, 317–321.
- (176) Li, Y.; Struwe, W. B.; Kukura, P. Single Molecule Mass Photometry of Nucleic Acids. *Nucleic Acids Res.* **2020**, *48*, e97.
- (177) Satapathy, S.; Dabbs, R. A.; Wilson, M. R. Rapid High-Yield Expression and Purification of Fully Post-Translationally Modified Recombinant Clusterin and Mutants. *Sci. Rep.* **2020**, *10*, 14243.
- (178) Reikine, S.; Mclaughlin, S. H.; Modis, Y. Equilibrium Binding Model for CpG DNA-Dependent Dimerization of Toll-like Receptor 9 Ectodomain. *Biochemistry* **2020**, *59*, 4155–4162.
- (179) Fouët, G.; Bally, I.; Signor, L.; Häußermann, K.; Thielens, N. M.; Rossi, V.; Gaboriaud, C. Headless C1q: A New Molecular Tool to Decipher Its Collagen-like Functions. *FEBS J.* **2021**, *288*, 2030–2041.
- (180) Dersch, S.; Reimold, C.; Stoll, J.; Breddermann, H.; Heimerl, T.; Defeu Soufo, H. J.; Graumann, P. L. Polymerization of *Bacillus Subtilis* MreB on a Lipid Membrane Reveals Lateral Co-Polymerization of MreB Paralogs and Strong Effects of Cations on Filament Formation. *BMC Mol. Cell Biol.* **2020**, *21*, 76.
- (181) Malay, A. D.; Miyazaki, N.; Biela, A.; Chakraborti, S.; Majsterkiewicz, K.; Stupka, I.; Kaplan, C. S.; Kowalczyk, A.; Piette, B. M. A. G.; Hochberg, G. K. A.; et al. An Ultra-Stable Gold-Coordinated Protein Cage Displaying Reversible Assembly. *Nature* **2019**, *569*, 438–442.
- (182) Tjondro, H. C.; Ugonotti, J.; Kawahara, R.; Chatterjee, S.; Chen, S.; Soltermann, F.; Hinneburg, H.; Parker, B. L.; Venkatakrishnan, V.; Loke, I.; et al. Hyper-Truncated Asn355- And Asn391-Glycans Modulate the Activity of Neutrophil Granule Myeloperoxidase. *J. Biol. Chem.* **2021**, *296*, 100144.
- (183) Marcaida, M. J.; Kauzlaric, A.; Duperrex, A.; Sülzle, J.; Moncrieffe, M. C.; Adebajo, D.; Manley, S.; Trono, D.; Dal Peraro, M. The Human RNA Helicase DDX21 Presents a Dimerization Interface Necessary for Helicase Activity. *iScience* **2020**, *23*, 101811.
- (184) Takada, H.; Roghanian, M.; Caballero-Montes, J.; Van Nerom, K.; Jimmy, S.; Kudrin, P.; Trebini, F.; Murayama, R.; Akanuma, G.; Garcia-Pino, A.; et al. Ribosome Association Primes the Stringent Factor Rel for TRNA-Dependent Locking in the A-Site and Activation of (p)PpGpp Synthesis. *Nucleic Acids Res.* **2021**, *49*, 444–457.



- (185) Olerinyova, A.; Sonn-Segev, A.; Gault, J.; Eichmann, C.; Schimpf, J.; Kopf, A. H.; Rudden, L. S. P.; Ashkinadze, D.; Bomba, R.; Frey, L.; et al. Mass Photometry of Membrane Proteins. *Chem.* **2021**, *7*, 224–236.
- (186) Wilk, P.; Kuška, K.; Wątor, E.; Malecki, P. H.; Woś, K.; Tokarz, P.; Dubin, G.; Grudnik, P. Structural Characterization of Glycerol Kinase from the Thermophilic Fungus *Chaetomium Thermophilum*. *Int. J. Mol. Sci.* **2020**, *21*, 9570.
- (187) Gunnarsson, A.; Stubbs, C. J.; Rawlins, P. B.; Taylor-Newman, E.; Lee, W. C.; Geschwindner, S.; Hytönen, V.; Holdgate, G.; Jha, R.; Dahl, G. Regenerable Biosensors for Small-Molecule Kinetic Characterization Using SPR. *SLAS Discovery* **2021**, *26*, 730–739.
- (188) Wu, D.; Piszczek, G. Rapid Determination of Antibody-Antigen Affinity by Mass Photometry. *J. Visualized Exp.* **2021**, *168*, No. e61784.
- (189) Thabault, L.; Liberelle, M.; Koruza, K.; Yildiz, E.; Joudiou, N.; Messens, J.; Brisson, L.; Wouters, J.; Sonveaux, P.; Frédérick, R. Discovery of a Novel Lactate Dehydrogenase Tetramerization Domain Using Epitope Mapping and Peptides. *J. Biol. Chem.* **2021**, *296*, 100422.
- (190) Foley, E. D. B.; Kushwah, M. S.; Young, G.; Kukura, P. Label-Free Tracking and Mass Measurement of Single Proteins on Lipid Bilayers. *bioRxiv* **2021**, 2021.04.08.438951. DOI: 10.1101/2021.04.08.438951.
- (191) Heermann, T.; Steiert, F.; Ramm, B.; Hundt, N.; Schulle, P. Mass-Sensitive Particle Tracking (MSPT) to Elucidate the Membrane-Associated MinDE Reaction Cycle. *bioRxiv* **2021**, 2021.04.08.438961. DOI: 10.1101/2021.04.08.438961.
- (192) Häußermann, K.; Young, G.; Kukura, P.; Dietz, H. Dissecting FOXP2 Oligomerization and DNA Binding. *Angew. Chem., Int. Ed.* **2019**, *58*, 7662–7667.
- (193) Hickman, A. B.; Kailasan, S.; Genzor, P.; Haase, A. D.; Dyda, F. Casposase Structure and the Mechanistic Link between DNA Transposition and Spacer Acquisition by CRISPR-Cas. *eLife* **2020**, *9*, e50004.
- (194) Sonn-Segev, A.; Belacic, K.; Bodrug, T.; Young, G.; VanderLinden, R. T.; Schulman, B. A.; Schimpf, J.; Friedrich, T.; Dip, P. V.; Schwartz, T. U.; et al. Quantifying the Heterogeneity of Macromolecular Machines by Mass Photometry. *Nat. Commun.* **2020**, *11*, 1772.
- (195) Wu, D.; Piszczek, G. Measuring the Affinity of Protein-Protein Interactions on a Single-Molecule Level by Mass Photometry. *Anal. Biochem.* **2020**, *592*, 113575.
- (196) Soltermann, F.; Foley, E. D. B.; Pagnoni, V.; Galpin, M.; Benesch, J. L. P.; Kukura, P.; Struwe, W. B. Quantifying Protein-Protein Interactions by Molecular Counting with Mass Photometry. *Angew. Chem., Int. Ed.* **2020**, *59*, 10774–10779.
- (197) Torres-Ocampo, A. P.; Özden, C.; Hommer, A.; Gardella, A.; Lapinskas, E.; Samkutty, A.; Esposito, E.; Garman, S. C.; Stratton, M. M. Characterization of CaMKII $\alpha$  Holoenzyme Stability. *Protein Sci.* **2020**, *29*, 1524–1534.
- (198) Tamara, S.; Franc, V.; Heck, A. J. R. A Wealth of Genotype-Specific Proteoforms Fine-Tunes Hemoglobin Scavenging by Haptoglobin. *Proc. Natl. Acad. Sci. U. S. A.* **2020**, *117*, 15554–15564.
- (199) Avci, O.; Ünlü, N.; Özkumur, A.; Ünlü, M. Interferometric Reflectance Imaging Sensor (IRIS)—A Platform Technology for Multiplexed Diagnostics and Digital Detection. *Sensors* **2015**, *15*, 17649–17665.
- (200) Özkumur, E.; Needham, J. W.; Bergstein, D. A.; Gonzalez, R.; Cabodi, M.; Gershoni, J. M.; Goldberg, B. B.; Ünlü, M. S. Label-Free and Dynamic Detection of Biomolecular Interactions for High-Throughput Microarray Applications. *Proc. Natl. Acad. Sci. U. S. A.* **2008**, *105*, 7988–7992.
- (201) Daaboul, G. G.; Yurt, A.; Zhang, X.; Hwang, G. M.; Goldberg, B. B.; Ünlü, M. S. High-Throughput Detection and Sizing of Individual Low-Index Nanoparticles and Viruses for Pathogen Identification. *Nano Lett.* **2010**, *10*, 4727–4731.
- (202) Sevenler, D.; Avci, O.; Ünlü, M. S. Quantitative Interferometric Reflectance Imaging for the Detection and Measurement of Biological Nanoparticles. *Biomed. Opt. Express* **2017**, *8*, 2976–2989.
- (203) Sevenler, D.; Daaboul, G. G.; Ekiz Kanik, F.; Ünlü, N. L.; Ünlü, M. S. Digital Microarrays: Single-Molecule Readout with Interferometric Detection of Plasmonic Nanorod Labels. *ACS Nano* **2018**, *12*, 5880–5887.
- (204) Daaboul, G. G.; Lopez, C. A.; Chinnala, J.; Goldberg, B. B.; Connor, J. H.; Ünlü, M. S. Digital Sensing and Sizing of Vesicular Stomatitis Virus Pseudotypes in Complex Media: A Model for Ebola and Marburg Detection. *ACS Nano* **2014**, *8*, 6047–6055.
- (205) Daaboul, G. G.; Freedman, D. S.; Scherr, S. M.; Carter, E.; Rosca, A.; Bernstein, D.; Mire, C. E.; Agans, K. N.; Hoenen, T.; Geisbert, T. W.; et al. Enhanced Light Microscopy Visualization of Virus Particles from Zika Virus to Filamentous Ebolaviruses. *PLoS One* **2017**, *12*, No. e0179728.
- (206) Daaboul, G. G.; Gagni, P.; Benussi, L.; Bettotti, P.; Ciani, M.; Cretich, M.; Freedman, D. S.; Ghidoni, R.; Ozkumur, A. Y.; Piotta, C.; et al. Digital Detection of Exosomes by Interferometric Imaging. *Sci. Rep.* **2016**, *6*, 37246.
- (207) Scherr, S. M.; Daaboul, G. G.; Trueb, J.; Sevenler, D.; Fawcett, H.; Goldberg, B.; Connor, J. H.; Ünlü, M. S. Real-Time Capture and Visualization of Individual Viruses in Complex Media. *ACS Nano* **2016**, *10*, 2827–2833.
- (208) Scherr, S. M.; Freedman, D. S.; Agans, K. N.; Rosca, A.; Carter, E.; Kuroda, M.; Fawcett, H. E.; Mire, C. E.; Geisbert, T. W.; Ünlü, M. S.; et al. Disposable Cartridge Platform for Rapid Detection of Viral Hemorrhagic Fever Viruses. *Lab Chip* **2017**, *17*, 917–925.
- (209) Seymour, E.; Daaboul, G. G.; Zhang, X.; Scherr, S. M.; Ünlü, N. L.; Connor, J. H.; Ünlü, M. S. DNA-Directed Antibody Immobilization for Enhanced Detection of Single Viral Pathogens. *Anal. Chem.* **2015**, *87*, 10505–10512.
- (210) Seymour, E.; Ünlü, N. L.; Carter, E. P.; Connor, J. H.; Ünlü, M. S. Configurable Digital Virus Counter on Robust Universal DNA Chips. *ACS Sensors* **2021**, *6*, 229–237.
- (211) Trueb, J. T.; Avci, O.; Sevenler, D.; Connor, J. H.; Ünlü, M. S. Robust Visualization and Discrimination of Nanoparticles by Interferometric Imaging. *IEEE J. Sel. Top. Quantum Electron.* **2017**, *23*, 394–403.
- (212) Aygun, U.; Urey, H.; Yalcin Ozkumur, A. Label-Free Detection of Nanoparticles Using Depth Scanning Correlation Interferometric Microscopy. *Sci. Rep.* **2019**, *9*, 9012.
- (213) Yurdakul, C.; Ünlü, M. S. Computational Nanosensing from Defocus in Single Particle Interferometric Reflectance Microscopy. *Opt. Lett.* **2020**, *45*, 6546–6549.
- (214) Tian, L.; Waller, L. Quantitative Differential Phase Contrast Imaging in an LED Array Microscope. *Opt. Express* **2015**, *23*, 11394–11403.
- (215) Tian, L.; Li, X.; Ramchandran, K.; Waller, L. Multiplexed Coded Illumination for Fourier Ptychography with an LED Array Microscope. *Biomed. Opt. Express* **2014**, *5*, 2376–2389.
- (216) Yurdakul, C.; Avci, O.; Matlock, A.; Devaux, A. J.; Quintero, M. V.; Ozbay, E.; Davey, R. A.; Connor, J. H.; Karl, W. C.; Tian, L. High-Throughput, High-Resolution Interferometric Light Microscopy of Biological Nanoparticles. *ACS Nano* **2020**, *14*, 2002–2013.
- (217) Monroe, M. R.; Daaboul, G. G.; Tuysuzoglu, A.; Lopez, C. A.; Little, F. F.; Ünlü, M. S. Single Nanoparticle Detection for Multiplexed Protein Diagnostics with Attomolar Sensitivity in Serum and Unprocessed Whole Blood. *Anal. Chem.* **2013**, *85*, 3698–3706.
- (218) Sevenler, D.; Trueb, J.; Ünlü, M. S. Beating the Reaction Limits of Biosensor Sensitivity with Dynamic Tracking of Single Binding Events. *Proc. Natl. Acad. Sci. U. S. A.* **2019**, *116*, 4129–4134.
- (219) Huang, Y.-F.; Zhuo, G.-Y.; Chou, C.-Y.; Lin, C.-H.; Chang, W.; Hsieh, C.-L. Coherent Brightfield Microscopy Provides the Spatio-temporal Resolution To Study Early Stage Viral Infection in Live Cells. *ACS Nano* **2017**, *11*, 2575–2585.
- (220) Cheng, C.-Y.; Liao, Y.-H.; Hsieh, C.-L. High-Speed Imaging and Tracking of Very Small Single Nanoparticles by Contrast Enhanced Microscopy. *Nanoscale* **2019**, *11*, 568–577.
- (221) Huang, Y. F.; Zhuo, G. Y.; Chou, C. Y.; Lin, C. H.; Hsieh, C. L. Label-Free, Ultrahigh-Speed, 3D Observation of Bidirectional and



Correlated Intracellular Cargo Transport by Coherent Brightfield Microscopy. *Nanoscale* **2017**, *9*, 6567–6574.

(222) Liedberg, B.; Nylander, C.; Lunström, I. Surface Plasmon Resonance for Gas Detection and Biosensing. *Sens. Actuators* **1983**, *4*, 299–304.

(223) Fischer, B.; Heyn, S. P.; Egger, M.; Gaub, H. E. Antigen Binding to a Pattern of Lipid-Anchored Antibody Binding Sites Measured by Surface Plasmon Microscopy. *Langmuir* **1993**, *9*, 136–140.

(224) Berger, C. E. H.; Beumer, T. A. M.; Kooyman, R. P. H.; Greve, J. Surface Plasmon Resonance Multisensing. *Anal. Chem.* **1998**, *70*, 703–706.

(225) Ladd, J.; Taylor, A. D.; Piliarik, M.; Homola, J.; Jiang, S. Label-Free Detection of Cancer Biomarker Candidates Using Surface Plasmon Resonance Imaging. *Anal. Bioanal. Chem.* **2009**, *393*, 1157–1163.

(226) Liu, W.; Chen, Y.; Yan, M. Surface Plasmon Resonance Imaging of Limited Glycoprotein Samples. *Analyst* **2008**, *133*, 1268–1273.

(227) Rebe Raz, S.; Bremer, M. G. E. G.; Giesbers, M.; Norde, W. Development of a Biosensor Microarray towards Food Screening, Using Imaging Surface Plasmon Resonance. *Biosens. Bioelectron.* **2008**, *24*, 552–557.

(228) Wong, C. L.; Ho, H. P.; Suen, Y. K.; Kong, S. K.; Chen, Q. L.; Yuan, W.; Wu, S. Y. Real-Time Protein Biosensor Arrays Based on Surface Plasmon Resonance Differential Phase Imaging. *Biosens. Bioelectron.* **2008**, *24*, 606–612.

(229) Yuk, J. S.; Kim, H. S.; Jung, J. W.; Jung, S. H.; Lee, S. J.; Kim, W. J.; Han, J. A.; Kim, Y. M.; Ha, K. S. Analysis of Protein Interactions on Protein Arrays by a Novel Spectral Surface Plasmon Resonance Imaging. *Biosens. Bioelectron.* **2006**, *21*, 1521–1528.

(230) Wegner, G. J.; Lee, H. J.; Marriott, G.; Corn, R. M. Fabrication of Histidine-Tagged Fusion Protein Arrays for Surface Plasmon Resonance Imaging Studies of Protein-Protein and Protein-DNA Interactions. *Anal. Chem.* **2003**, *75*, 4740–4746.

(231) Jordan, C. E.; Frutos, A. G.; Thiel, A. J.; Corn, R. M. Surface Plasmon Resonance Imaging Measurements of DNA Hybridization Adsorption and Streptavidin/DNA Multilayer Formation at Chemically Modified Gold Surfaces. *Anal. Chem.* **1997**, *69*, 4939–4947.

(232) Nelson, B. P.; Grimsrud, T. E.; Liles, M. R.; Goodman, R. M.; Corn, R. M. Surface Plasmon Resonance Imaging Measurements of DNA and RNA Hybridization Adsorption onto DNA Microarrays. *Anal. Chem.* **2001**, *73*, 1–7.

(233) Mannelli, I.; Courtois, V.; Lecaruyer, P.; Roger, G.; Millot, M. C.; Goossens, M.; Canva, M. Surface Plasmon Resonance Imaging (SPRI) System and Real-Time Monitoring of DNA Biochip for Human Genetic Mutation Diagnosis of DNA Amplified Samples. *Sens. Actuators, B* **2006**, *119*, 583–591.

(234) Hayashi, G.; Hagihara, M.; Nakatani, K. Genotyping by Allele-Specific l-DNA-Tagged PCR. *J. Biotechnol.* **2008**, *135*, 157–160.

(235) Li, Y.; Lee, H. J.; Corn, R. M. Fabrication and Characterization of RNA Aptamer Microarrays for the Study of Protein-Aptamer Interactions with SPR Imaging. *Nucleic Acids Res.* **2006**, *34*, 6416–6424.

(236) Nelson, B. P.; Liles, M. R.; Frederick, K. B.; Corn, R. M.; Goodman, R. M. Label-Free Detection of 16S Ribosomal RNA Hybridization on Reusable DNA Arrays Using Surface Plasmon Resonance Imaging. *Environ. Microbiol.* **2002**, *4*, 735–743.

(237) Nelson, B. P.; Frutos, A. G.; Brockman, J. M.; Corn, R. M. Near-Infrared Surface Plasmon Resonance Measurements of Ultrathin Films. I. Angle Shift and SPR Imaging Experiments. *Anal. Chem.* **1999**, *71*, 3928–3934.

(238) Brockman, J. M.; Frutos, A. G.; Corn, R. M. A Multistep Chemical Modification Procedure to Create DNA Arrays on Gold Surfaces for the Study of Protein-DNA Interactions with Surface Plasmon Resonance Imaging. *J. Am. Chem. Soc.* **1999**, *121*, 8044–8051.

(239) Jeong, E. J.; Jeong, Y. S.; Park, K.; Yi, S. Y.; Ahn, J.; Chung, S. J.; Kim, M.; Chung, B. H. Directed Immobilization of DNA-Binding Proteins on a Cognate DNA-Modified Chip Surface. *J. Biotechnol.* **2008**, *135*, 16–21.

(240) Homola, J.; Yee, S. S.; Gauglitz, G. Surface Plasmon Resonance Sensors: Review. *Sens. Actuators, B* **1999**, *54*, 3–15.

(241) Homola, J. Surface Plasmon Resonance Sensors for Detection of Chemical and Biological Species. *Chem. Rev.* **2008**, *108*, 462–493.

(242) Hinman, S. S.; McKeating, K. S.; Cheng, Q. Surface Plasmon Resonance: Material and Interface Design for Universal Accessibility. *Anal. Chem.* **2018**, *90*, 19–39.

(243) Guo, X. Surface Plasmon Resonance Based Biosensor Technique: A Review. *Journal of Biophotonics.* **2012**, *5*, 483–501.

(244) Masson, J. F. Surface Plasmon Resonance Clinical Biosensors for Medical Diagnostics. *ACS Sensors.* **2017**, *2*, 16–30.

(245) Zeidan, E.; Kepley, C. L.; Sayes, C.; Sandros, M. G. Surface Plasmon Resonance: A Label-Free Tool for Cellular Analysis. *Nanomedicine* **2015**, *10*, 1833–1846.

(246) Stahelin, R. V. Surface Plasmon Resonance: A Useful Technique for Cell Biologists to Characterize Biomolecular Interactions. *Mol. Biol. Cell* **2013**, *24*, 883–886.

(247) Jung, L. S.; Campbell, C. T.; Chinowsky, T. M.; Mar, M. N.; Yee, S. S. Quantitative Interpretation of the Response of Surface Plasmon Resonance Sensors to Adsorbed Films. *Langmuir* **1998**, *14*, 5636–5648.

(248) Yeatman, E.; Ash, E. A. Surface Plasmon Microscopy. *Electron. Lett.* **1987**, *23*, 1091–1092.

(249) Rothenhäusler, B.; Knoll, W. Surface-Plasmon Microscopy. *Nature* **1988**, *332*, 615–617.

(250) Zhang, F.; Wang, S.; Yin, L.; Yang, Y.; Guan, Y.; Wang, W.; Xu, H.; Tao, N. Quantification of Epidermal Growth Factor Receptor Expression Level and Binding Kinetics on Cell Surfaces by Surface Plasmon Resonance Imaging. *Anal. Chem.* **2015**, *87*, 9960–9965.

(251) Scarano, S.; Mascini, M.; Turner, A. P. F.; Minunni, M. Surface Plasmon Resonance Imaging for Affinity-Based Biosensors. *Biosens. Bioelectron.* **2010**, *25*, 957–966.

(252) Campbell, C. T.; Kim, G. SPR Microscopy and Its Applications to High-Throughput Analyses of Biomolecular Binding Events and Their Kinetics. *Biomaterials* **2007**, *28*, 2380–2392.

(253) Fasoli, J. B.; Corn, R. M. Surface Enzyme Chemistries for Ultrasensitive Microarray Biosensing with SPR Imaging. *Langmuir* **2015**, *31*, 9527–9536.

(254) Hinman, S. S.; Ruiz, C. J.; Drakakaki, G.; Wilkop, T. E.; Cheng, Q. On-Demand Formation of Supported Lipid Membrane Arrays by Trehalose-Assisted Vesicle Delivery for SPR Imaging. *ACS Appl. Mater. Interfaces* **2015**, *7*, 17122–17130.

(255) Manuel, G.; Lupták, A.; Corn, R. M. A Microwell-Printing Fabrication Strategy for the On-Chip Templated Biosynthesis of Protein Microarrays for Surface Plasmon Resonance Imaging. *J. Phys. Chem. C* **2016**, *120*, 20984–20990.

(256) Huang, B.; Yu, F.; Zare, R. N. Surface Plasmon Resonance Imaging Using a High Numerical Aperture Microscope Objective. *Anal. Chem.* **2007**, *79*, 2979–2983.

(257) Kretschmann, E.; Raether, H. Radiative Decay of Non Radiative Surface Plasmons Excited by Light. *Z. Naturforsch., A: Phys. Sci.* **1968**, *23*, 2135–2136.

(258) Orlovski, R.; Raether, H. The Total Reflection of Light at Smooth and Rough Silver Films and Surface Plasmons. *Surf. Sci.* **1976**, *54*, 303–308.

(259) Jiang, Y.; Wang, W. Point Spread Function of Objective-Based Surface Plasmon Resonance Microscopy. *Anal. Chem.* **2018**, *90*, 9650–9656.

(260) Yu, H.; Shan, X.; Wang, S.; Chen, H.; Tao, N. Molecular Scale Origin of Surface Plasmon Resonance Biosensors. *Anal. Chem.* **2014**, *86*, 8992–8997.

(261) Bozhevolnyi, S. I. Localization Phenomena in Elastic Surface-Polariton Scattering Caused by Surface Roughness. *Phys. Rev. B: Condens. Matter Mater. Phys.* **1996**, *54*, 8177–8185.

(262) Bozhevolnyi, S. I.; Coello, V. Elastic Scattering of Surface Plasmon Polaritons: Modeling and Experiment. *Phys. Rev. B: Condens. Matter Mater. Phys.* **1998**, *58*, 10899–10910.

- (263) Hecht, B.; Bielefeldt, H.; Novotny, L.; Inoué, Y.; Pohl, D. W. Local Excitation, Scattering, and Interference of Surface Plasmons. *Phys. Rev. Lett.* **1996**, *77*, 1889–1892.
- (264) Berini, P. Long-Range Surface Plasmon Polaritons. *Adv. Opt. Photonics* **2009**, *1*, 484–588.
- (265) Kelly, K. L.; Coronado, E.; Zhao, L. L.; Schatz, G. C. The Optical Properties of Metal Nanoparticles: The Influence of Size, Shape, and Dielectric Environment. *J. Phys. Chem. B* **2003**, *107*, 668–677.
- (266) Becker, J.; Trügler, A.; Jakab, A.; Hohenester, U.; Sönnichsen, C. The Optimal Aspect Ratio of Gold Nanorods for Plasmonic Bio-Sensing. *Plasmonics* **2010**, *5*, 161–167.
- (267) Zijlstra, P.; Paulo, P. M. R.; Orrit, M. Optical Detection of Single Non-Absorbing Molecules Using the Surface Plasmon Resonance of a Gold Nanorod. *Nat. Nanotechnol.* **2012**, *7*, 379–382.
- (268) Ament, I.; Prasad, J.; Henkel, A.; Schmachtel, S.; Sönnichsen, C. Single Unlabeled Protein Detection on Individual Plasmonic Nanoparticles. *Nano Lett.* **2012**, *12*, 1092–1095.
- (269) Vecchi, G.; Giannini, V.; Gómez Rivas, J. Surface Modes in Plasmonic Crystals Induced by Diffractive Coupling of Nanoantennas. *Phys. Rev. B: Condens. Matter Mater. Phys.* **2009**, *80*, 201401.
- (270) Chen, P.; Chung, M. T.; McHugh, W.; Nidetz, R.; Li, Y.; Fu, J.; Cornell, T. T.; Shanley, T. P.; Kurabayashi, K. Multiplex Serum Cytokine Immunoassay Using Nanoplasmonic Biosensor Microarrays. *ACS Nano* **2015**, *9*, 4173–4181.
- (271) Li, X.; Soler, M.; Özdemir, C. I.; Belushkin, A.; Yesilköy, F.; Altug, H. Plasmonic Nanohole Array Biosensor for Label-Free and Real-Time Analysis of Live Cell Secretion. *Lab Chip* **2017**, *17*, 2208–2217.
- (272) Guo, H.; Guo, J. Hybrid Plasmon Photonic Crystal Resonance Grating for Integrated Spectrometer Biosensor. *Opt. Lett.* **2015**, *40*, 249–252.
- (273) Seiler, S. T.; Rich, I. S.; Lindquist, N. C. Direct Spectral Imaging of Plasmonic Nanohole Arrays for Real-Time Sensing. *Nanotechnology* **2016**, *27*, 184001.
- (274) Bockova, M.; Slaby, J.; Springer, T.; Homola, J. Advances in Surface Plasmon Resonance Imaging and Microscopy and Their Biological Applications. *Annu. Rev. Anal. Chem.* **2019**, *12*, 151–176.
- (275) Zeng, Y.; Hu, R.; Wang, L.; Gu, D.; He, J.; Wu, S. Y.; Ho, H. P.; Li, X.; Qu, J.; Gao, B. Z.; et al. Recent Advances in Surface Plasmon Resonance Imaging: Detection Speed, Sensitivity, and Portability. *Nanophotonics* **2017**, *6*, 1017–1030.
- (276) Wong, C. L.; Olivo, M. Surface Plasmon Resonance Imaging Sensors: A Review. *Plasmonics* **2014**, *9*, 809–824.
- (277) Wang, S.; Shan, X.; Patel, U.; Huang, X.; Lu, J.; Li, J.; Tao, N. Label-Free Imaging, Detection, and Mass Measurement of Single Viruses by Surface Plasmon Resonance. *Proc. Natl. Acad. Sci. U. S. A.* **2010**, *107*, 16028–16032.
- (278) Demetriadou, A.; Kornyshev, A. A. Principles of Nanoparticle Imaging Using Surface Plasmons. *New J. Phys.* **2015**, *17*, 013041.
- (279) Qian, C.; Wu, G.; Jiang, D.; Zhao, X.; Chen, H. B.; Yang, Y.; Liu, X. W. Identification of Nanoparticles via Plasmonic Scattering Interferometry. *Angew. Chem., Int. Ed.* **2019**, *58*, 4217–4220.
- (280) Yang, Y.; Yu, H.; Shan, X.; Wang, W.; Liu, X.; Wang, S.; Tao, N. Label-Free Tracking of Single Organelle Transportation in Cells with Nanometer Precision Using a Plasmonic Imaging Technique. *Small* **2015**, *11*, 2878–2884.
- (281) Yu, H.; Shan, X.; Wang, S.; Chen, H.; Tao, N. Plasmonic Imaging and Detection of Single DNA Molecules. *ACS Nano* **2014**, *8*, 3427–3433.
- (282) Syal, K.; Iriya, R.; Yang, Y.; Yu, H.; Wang, S.; Haydel, S. E.; Chen, H. Y.; Tao, N. Antimicrobial Susceptibility Test with Plasmonic Imaging and Tracking of Single Bacterial Motions on Nanometer Scale. *ACS Nano* **2016**, *10*, 845–852.
- (283) Wang, W.; Wang, S.; Liu, Q.; Wu, J.; Tao, N. Mapping Single-Cell-Substrate Interactions by Surface Plasmon Resonance Microscopy. *Langmuir* **2012**, *28*, 13373–13379.
- (284) Toma, K.; Kano, H.; Offenhäusser, A. Label-Free Measurement of Cell-Electrode Cleft Gap Distance with High Spatial Resolution Surface Plasmon Microscopy. *ACS Nano* **2014**, *8*, 12612–12619.
- (285) Yang, C. T.; Méjard, R.; Griesser, H. J.; Bagnaninchi, P. O.; Thierry, B. Cellular Micromotion Monitored by Long-Range Surface Plasmon Resonance with Optical Fluctuation Analysis. *Anal. Chem.* **2015**, *87*, 1456–1461.
- (286) Zhou, X.; Yang, Y.; Wang, S.; Liu, X. Surface Plasmon Resonance Microscopy: From Single Molecule Sensing to Single Cell Imaging. *Angew. Chem., Int. Ed.* **2020**, *59*, 1776–1785.
- (287) Foley, K. J.; Shan, X.; Tao, N. J. Surface Impedance Imaging Technique. *Anal. Chem.* **2008**, *80*, 5146–5151.
- (288) Yuan, L.; Tao, N.; Wang, W. Plasmonic Imaging of Electrochemical Impedance. *Annu. Rev. Anal. Chem.* **2017**, *10*, 183–200.
- (289) Liang, W.; Wang, S.; Festa, F.; Wiktor, P.; Wang, W.; Magee, M.; Labaer, J.; Tao, N. Measurement of Small Molecule Binding Kinetics on a Protein Microarray by Plasmonic-Based Electrochemical Impedance Imaging. *Anal. Chem.* **2014**, *86*, 9860–9865.
- (290) Macgriff, C.; Wang, S.; Wiktor, P.; Wang, W.; Shan, X.; Tao, N. Charge-Based Detection of Small Molecules by Plasmonic-Based Electrochemical Impedance Microscopy. *Anal. Chem.* **2013**, *85*, 6682–6687.
- (291) Halpern, A. R.; Wood, J. B.; Wang, Y.; Corn, R. M. Single-Nanoparticle Near-Infrared Surface Plasmon Resonance Microscopy for Real-Time Measurements of DNA Hybridization Adsorption. *ACS Nano* **2014**, *8*, 1022–1030.
- (292) Shan, X.; Fang, Y.; Wang, S.; Guan, Y.; Chen, H. Y.; Tao, N. Detection of Charges and Molecules with Self-Assembled Nano-Oscillators. *Nano Lett.* **2014**, *14*, 4151–4157.
- (293) Fang, Y.; Chen, S.; Wang, W.; Shan, X.; Tao, N. Real-Time Monitoring of Phosphorylation Kinetics with Self-Assembled Nano-Oscillators. *Angew. Chem., Int. Ed.* **2015**, *54*, 2538–2542.
- (294) Chen, Z.; Peng, Y.; Cao, Y.; Wang, H.; Zhang, J. R.; Chen, H. Y.; Zhu, J. J. Light-Driven Nano-Oscillators for Label-Free Single-Molecule Monitoring of MicroRNA. *Nano Lett.* **2018**, *18*, 3759–3765.
- (295) Ma, G.; Wan, Z.; Yang, Y.; Zhang, P.; Wang, S.; Tao, N. Optical Imaging of Single-Protein Size, Charge, Mobility, and Binding. *Nat. Commun.* **2020**, *11*, 4758.
- (296) Kano, H.; Knoll, W. A Scanning Microscope Employing Localized Surface-Plasmon-Polaritons as a Sensing Probe. *Opt. Commun.* **2000**, *182*, 11–15.
- (297) Watanabe, K.; Horiguchi, N.; Kano, H. Optimized Measurement Probe of the Localized Surface Plasmon Microscope by Using Radially Polarized Illumination. *Appl. Opt.* **2007**, *46*, 4985–4990.
- (298) Watanabe, K.; Ryosuke, M.; Terakado, G.; Okazaki, T.; Morigaki, K.; Kano, H. High Resolution Imaging of Patterned Model Biological Membranes by Localized Surface Plasmon Microscopy. *Appl. Opt.* **2010**, *49*, 887–891.
- (299) Kuai, Y.; Chen, J.; Tang, X.; Xiang, Y.; Lu, F.; Kuang, C.; Xu, L.; Shen, W.; Cheng, J.; Gui, H. Label-Free Surface-Sensitive Photonic Microscopy with High Spatial Resolution Using Azimuthal Rotation Illumination. *Sci. Adv.* **2019**, *5*, eaav5335.
- (300) Banville, F. A.; Söllradl, T.; Zermatten, P.-J.; Grandbois, M.; Charette, P. G. Improved Resolution in SPR and MCWG Microscopy by Combining Images Acquired with Distinct Mode Propagation Directions. *Opt. Lett.* **2015**, *40*, 1165–1168.
- (301) Son, T.; Lee, C.; Seo, J.; Choi, I.-H.; Kim, D. Surface Plasmon Microscopy by Spatial Light Switching for Label-Free Imaging with Enhanced Resolution. *Opt. Lett.* **2018**, *43*, 959–962.
- (302) Tan, H. M.; Pechprasarn, S.; Zhang, J.; Pitter, M. C.; Somekh, M. G. High Resolution Quantitative Angle-Scanning Widefield Surface Plasmon Microscopy. *Sci. Rep.* **2016**, *6*, 20195.
- (303) Tang, W. T.; Chung, E.; Kim, Y.-H.; So, P. T. C.; Sheppard, C. J. R. Investigation of the Point Spread Function of Surface Plasmon-Coupled Emission Microscopy. *Opt. Express* **2007**, *15*, 4634–4646.
- (304) Tang, W. T.; Chung, E.; Kim, Y.-H.; So, P. T.; Sheppard, C. J. Surface-Plasmon-Coupled Emission Microscopy with a Spiral Phase Plate. *Opt. Lett.* **2010**, *35*, 517–519.

(305) Chen, Y.; Zhang, D.; Han, L.; Rui, G.; Wang, X.; Wang, P.; Ming, H. Surface-Plasmon-Coupled Emission Microscopy with a Polarization Converter. *Opt. Lett.* **2013**, *38*, 736–738.

(306) Zhang, P.; Ma, G.; Dong, W.; Wan, Z.; Wang, S.; Tao, N. Plasmonic Scattering Imaging of Single Proteins and Binding Kinetics. *Nat. Methods* **2020**, *17*, 1010–1017.

(307) Zhang, P.; Ma, G.; Wan, Z.; Wang, S. Quantification of Single-Molecule Protein Binding Kinetics in Complex Media with Prism-Coupled Plasmonic Scattering Imaging. *ACS Sens.* **2021**, *6*, 1357–1366.

(308) Yu, H.; Shan, X.; Wang, S.; Tao, N. Achieving High Spatial Resolution Surface Plasmon Resonance Microscopy with Image Reconstruction. *Anal. Chem.* **2017**, *89*, 2704–2707.

(309) Yang, Y.; Shen, G.; Wang, H.; Li, H.; Zhang, T.; Tao, N.; Ding, X.; Yu, H. Interferometric Plasmonic Imaging and Detection of Single Exosomes. *Proc. Natl. Acad. Sci. U. S. A.* **2018**, *115*, 10275–10280.

(310) Sung, J.; Schnedermann, C.; Ni, L.; Sadhanala, A.; Chen, R. Y. S.; Cho, C.; Priest, L.; Lim, J. M.; Kim, H. K.; Monserrat, B.; et al. Long-Range Ballistic Propagation of Carriers in Methylammonium Lead Iodide Perovskite Thin Films. *Nat. Phys.* **2020**, *16*, 171–176.

(311) Delor, M.; Weaver, H. L.; Yu, Q. Q.; Ginsberg, N. S. Imaging Material Functionality through Three-Dimensional Nanoscale Tracking of Energy Flow. *Nat. Mater.* **2020**, *19*, 56–62.

(312) Merryweather, A. J.; Schnedermann, C.; Jacquet, Q.; Grey, C. P.; Rao, A. Operando Optical Tracking of Single-Particle Ion Dynamics and Phase Transitions in Batteries. *Nature* **2021**, *594*, 522–528.

(313) Bai, Y.; Yin, J.; Cheng, J.-X. Bond-Selective Imaging by Optically Sensing the Mid-Infrared Photothermal Effect. *Sci. Adv.* **2021**, *7*, No. eabg1559.

(314) Zhang, D.; Li, C.; Zhang, C.; Slipchenko, M. N.; Eakins, G.; Cheng, J.-X. Depth-Resolved Mid-Infrared Photothermal Imaging of Living Cells and Organisms with Submicrometer Spatial Resolution. *Sci. Adv.* **2016**, *2*, No. e1600521.

(315) Li, Z.; Aleshire, K.; Kuno, M.; Hartland, G. V. Super-Resolution Far-Field Infrared Imaging by Photothermal Heterodyne Imaging. *J. Phys. Chem. B* **2017**, *121*, 8838–8846.

(316) Bai, Y.; Zhang, D.; Lan, L.; Huang, Y.; Maize, K.; Shakouri, A.; Cheng, J.-X. Ultrafast Chemical Imaging by Widefield Photothermal Sensing of Infrared Absorption. *Sci. Adv.* **2019**, *5*, No. eaav7127.

(317) Pavlovets, I. M.; Podshivaylov, E. A.; Chatterjee, R.; Hartland, G. V.; Frantsuzov, P. A.; Kuno, M. Infrared Photothermal Heterodyne Imaging: Contrast Mechanism and Detection Limits. *J. Appl. Phys.* **2020**, *127*, 165101.

(318) Zhang, Y.; Yurdakul, C.; Devaux, A. J.; Wang, L.; Xu, X. G.; Connor, J. H.; Ünlü, M. S.; Cheng, J.-X. Vibrational Spectroscopic Detection of a Single Virus by Mid-Infrared Photothermal Microscopy. *Anal. Chem.* **2021**, *93*, 4100–4107.